Study of Z-Boson Pair Production and Search for Physics beyond Standard Model at LEP-II

Ph.D. Degree in Physics

Submitted by
Gagan Bihari Mohanty

Under the Guidance of
Prof. Tariq Aziz

Tata Institute of Fundamental Research
Mumbai 400 005

2002

Study of $\mathbf{Z}$-Boson Pair Production and Search for Physics beyond Standard Model at LEP-II

Gagan Bihari Mohanty

Tata Institute of Fundamental Research
Mumbai 400 005

A Thesis submitted to the

University of Mumbai

for the degree of
Doctor of Philosophy in Physics

July, 2002

To my parents ...

Acknowledgement

It is long back since I joined TIFR, I have fully enjoyed the congenial and productive atmosphere offered by the institute. Starting from the graduate school up to the completion of my Ph.D., the institute has left some undeniable marks in my life, at par it's excellence.

Prof. Tariq Aziz, my thesis supervisor, has given me enough independence to try out all my ideas but without failing to point out the mistakes. His clarity and well understanding of the subject has helped a lot on my analysis at various stages. I would like to thank him for his patience, forbearance and kind encouragement.

I have been fortunate enough to have all the supports and suggestions from all the faculty members of the Experimental High Energy Physics group. Prof. Sunanda Banerjee, in particular, has helped me a lot on teaching me the intricacies of L3 software and various analysis techniques. I owe a great deal to Profs. S.N. Ganguli, A. Gurtu and S.C. Tonwar, Drs. K. Sudhakar, Kajari Mazumdar and Gobinda Majumder for all their help at different stages. A big thank you to Mr. P.V. Deshpande for his consistent effort to maintain the group computers in good shape. On theoretical side, Prof. K. Sridhar has freshened up many of the old or new ideas alike, while giving a course on particle physics. Profs. D.P. Roy, R.V. Gavai and Dr. M. Guchait have nicely supported to that end only.

I thank the European Organisation for Nuclear Research (CERN) for its kind hospitality during my extended period of stay there. All the members of the Large Electron Positron (LEP) accelerator group deserve a special mention for successful LEP operation over the last decade. The members of the L3 collaboration and the L3 ZZ Group in particular have provided a stimulating working environment. In particular, I thank Salvatore Mele, Eusebio Sánchez, Andreas Kopp, Chris Tully, Manish Wadhwa, Marta Felcini, Swagato Banerjee, Nandakumar Raja, Martin Weber, Miroslav Kopal, Mohd. Azizur Rahaman and Sanjeev Baldew for their help. Mehnaz Hafeez and Alexendre Elline in the later stage have helped on many of the computer related problems. A special thank to both of them.

I thank all my friends who helped me on many occasions with various issues, and made my graduate days worthwhile and interesting. Gulab, Sachi, Dilip, Palitbhai, Ashok, Manoj, Neel, Pravat, Prasantabhai, Vinod, Nemani and Nirvikar are a few to the long-list. Finally, it is all to my parents and family for their support and understanding, without which this thesis would have never seen the light.

Contents

List of Figures

List of Tables

SYNOPSIS

Title of the Thesis	:	STUDY OF Z-BOSON PAIR PRODUCTION
	:	AND SEARCH FOR PHYSICS BEYOND
	:	STANDARD MODEL AT LEP-II
Name of the Candidate	:	GAGAN BIHARI MOHANTY
Registration Number	:	TIFR–184 (29/7/1998)
Degree	:	DOCTOR OF PHILOSOPHY
Subject	:	PHYSICS
Thesis Supervisor	:	PROF. TARIQ AZIZ
Institution	:	TATA INSTITUTE OF
	:	FUNDAMENTAL RESEARCH,
	:	MUMBAI 400 005, INDIA.

Study of Z-Boson Pair Production

Since 1997, Large Electron Positron (LEP) collider at CERN has accumulated an integrated luminosity of 680 pb^{-1} at the centre-of-mass energies ($\sqrt{s}$) around and above the Z-pair production threshold. This has opened up an additional avenue of measurement in the neutral gauge boson sector of the Standard Model [1]. In the Standard Model (SM), a pair of Z-bosons is produced via t and u-channel electron exchange diagrams [2], with no additional contribution from triple gauge boson vertices unlike $\mathrm{W^+W^-}$ case. The Z-pair production cross section is also significantly lower than that of W-pair and other SM processes, making the experimental investigation of the process quite difficult.

This thesis describes the study of the final state where one Z decays to $\mathrm{q\bar{q}}$ leading to two hadronic jets and other Z to a pair of leptons [6]. The work is based on the data collected with the L3 detector [5] at $\sqrt{s}$ ranging from 183 GeV up to 208 GeV, the highest energy achieved at LEP towards the end of it's operation. L3 detector consists of a high precision Silicon vertex detector, a central tracking chamber operating on time expansion mode (TEC), a high resolution electromagnetic calorimeter (BGO) encapsulating the central detector, a hermetic hadron calorimeter (HCAL) and a high precision muon chamber (MUCH). All the sub-detectors are immersed in a uniform 0.5 Tesla solenoidal magnetic field.

Despite clean event topology due to presence of two well isolated leptons in the aforesaid final state, relative low event rate ($\mathcal{B.R.} \simeq 14\%$) requires delicate balance between lepton identification and kinematic selection. The leptons ($\mathrm{e}/\mu/\tau$) are identified in the L3 detector using their characteristic signatures. An electron is identified by demanding a well isolated electromagnetic cluster in the BGO calorimeter with an associated track in the tracking chamber. The muon, being a minimum ionising particle, can easily penetrate through a large depth of matter without being disturbed too much. At L3, it is identified by a matching track in the TEC and muon chamber along with an associated MIP signal in the calorimeters. The tau lepton is a short lived particle with a life time of about 2.9×10^{-13} second which corresponds to decay flight of ≈ 2 mm. Hence, only the visible decay products are observed in the detector in a very narrow cone around it's flight direction. Keeping it in mind, we have used the cone algorithm to reconstruct the tau from it's decay product. After identifying two leptons, the remaining clusters in the event are forced into two jets and a kinematic fit is performed by varying the four momenta of the reconstructed particles (jets and leptons here) within their experimental resolution imposing the energy-momentum conservation. An additional constraint of equal di-jet and di-lepton masses is utilised in the fit to further improve the mass resolution.

Selection procedure evolves around the fact that, both the Z's are produced on the mass-shell leading to constraints on reconstructed masses of di-quark and di-lepton systems, finite boost for Z allowing to restrict on the energy sharing between the daughter particles. An optimal set of selection variables is chosen, meeting these requirements, to discriminate the signal and background processes. Precise cut positions are determined by minimising the relative error on the expected cross section. The cut values are retuned as we go to higher energies to take care of modified signal topology. Over the full data sample analysed, we select 71 candidates to be compared with 63 events expected from the simulation (signal=50 and background=13) with an overall signal efficiency of 54% and purity of 84%.

Due to low statistics, instead of using the counting method we fit the most discriminative variable, the equal mass spectrum, to a maximum binned likelihood function to determine the cross section for the process: $e^+e^- \to ZZ \to q\bar{q}\ell^+\ell^-$. Various contributions to the systematics error on the measurement are estimated and the final error is calculated by adding the statistical and systematic errors in quadrature.

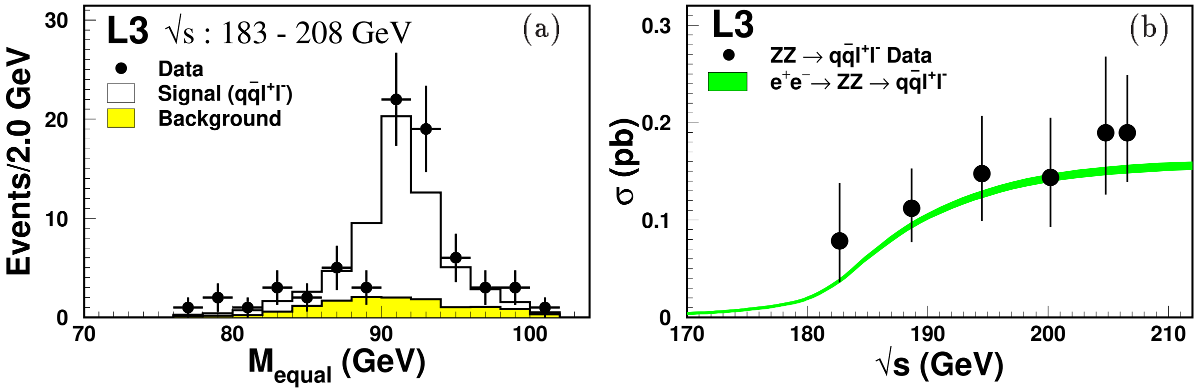

Figure 1: (a) *Distribution of the equal mass spectrum, the final variable used to determine the cross section,* and (b) *Standard Model prediction for the* $e^+e^- \to ZZ \to q\bar{q}\ell^+\ell^-$ *cross section with the corresponding measurement. A 2% theoretical uncertainty is assigned to the prediction.*

Figure 1 shows the distribution of the equal mass spectrum integrated over the total data sample and the variation of the measured cross section as a function of centre-of-mass energy along with the expectation from the Standard Model. In both the cases, we find good agreement between our measurement and the Standard Model prediction.

Study of inclusive $b\bar{b}$ final state

To better understand one of the major backgrounds for the Standard Model Higgs production and to test the capability of our detector to detect an intermediate-mass Higgs boson ($m_H \lesssim 140$ GeV), the process $e^+e^- \to ZZ \to b\bar{b}\ell^+\ell^-$ is closely studied. Since in this particular mass range, Higgs produced in association with Z leads to identical final state, $b\bar{b}X$ ($X = q\bar{q}$, $\ell^+\ell^-$ or $\nu\bar{\nu}$), similar to the process where one of the Z decays to $b\bar{b}$. Also, the cross sections for these two processes are quite similar.

A single discriminant is constructed out of the equal mass spectrum, as explained earlier, and the b-tag value of the two jets. The distribution of the discriminant is fitted to extract $\mathrm{ZZ} \to \mathrm{b\bar{b}}\ell^+\ell^-$ cross section. Because of low statistics, all data are combined to calculate a single luminosity-averaged cross section.

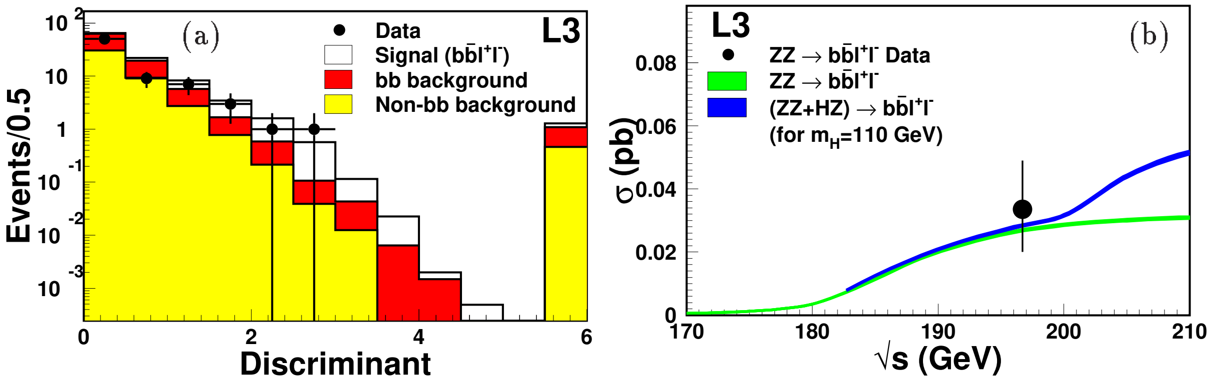

Figure 2: (a) *Distribution of the discriminant variables for the* $\mathrm{b\bar{b}}\ell^+\ell^-$ *selection (the last bin shows the overflow),* and (b) *variation of* $\mathrm{e^+e^-} \to \mathrm{ZZ} \to \mathrm{b\bar{b}}\ell^+\ell^-$ *cross section as a function of* $\sqrt{s}$*, with the corresponding measurement. The measured value of the cross section is also compared with the combined prediction of* HZ *and* ZZ *productions.*

Figure 2 shows the distribution of the final discriminant and measured $\mathrm{b\bar{b}}\ell^+\ell^-$ cross section along with it's expected evolution with $\sqrt{s}$. We find reasonable agreement with the Standard Model prediction.

Anomalous Tri-linear Neutral Gauge coupling

Tri-linear neutral gauge couplings are not allowed within the Standard Model because of $SU(2)_L \otimes U(1)_Y$ symmetry. Thus in order to ascertain the gauge structure of the Standard Model, it is essential to experimentally verify the non-existence of these couplings. In case of resonant Z-pair production, using $U_{em}(1)$ invariance and Bose-Einstein symmetry the most general expression for the anomalous vertex function can be expressed in terms of four couplings f_4^{V} and f_5^{V} ($\mathrm{V} = \mathrm{Z}$ or γ) [3]. A non-zero value for f_4^{V} leads to a C-violating, P-conserving process, while terms associated f_5^{V} are both C and P-violating.

Effect of anomalous couplings in ZZ events can be realised in various ways: (a) change in the observed cross section for the process, (b) modification of the angular distribution of the Z and (c) change in the average polarisation of the Z. However, given the low statistics associated with ZZ production, last two informations do not help much. Instead, we compare the integrated number of expected events with non-zero values for different anomalous couplings with the data. This is done by reweighting each signal event with a factor:

$$W(\{p^\nu\}, f_i^{\mathrm{V}}) \equiv \frac{\frac{1}{4}\sum\limits_{\lambda} \left| (\mathcal{M}_{\mathrm{SM}}(\{p^\nu\},\lambda) + \mathcal{M}_{\mathrm{AC}}(\{p^\nu\},\lambda, f_i^{\mathrm{V}})) \right|^2}{\frac{1}{4}\sum\limits_{\lambda} \left| \mathcal{M}_{\mathrm{SM}}(\{p^\nu\},\lambda) \right|^2},$$

where $\mathcal{M}_{\rm SM}(\{p^\nu\},\lambda)$ is the Standard Model amplitude for the signal process and $\mathcal{M}_{\rm AC}(\{p^\nu\},\lambda,f_i^{\rm V})$ is the contribution from the anomalous coupling, $f_i^{\rm V}$. No evidence for the anomalous couplings has been found and the null result is translated into 95% confidence level limits on those couplings:

$$
\begin{array}{rcllcl}
-0.37 \leq & f_4^{\rm Z} & \leq 0.43 & & (\text{SM: } f_4^{\rm Z}{=}0) \\
-0.82 \leq & f_5^{\rm Z} & \leq 0.94 & & (\text{SM: } f_5^{\rm Z}{=}0) \\
-0.25 \leq & f_4^{\gamma} & \leq 0.22 & & (\text{SM: } f_4^{\gamma}{=}0) \\
-0.49 \leq & f_5^{\gamma} & \leq 0.55 & & (\text{SM: } f_5^{\gamma}{=}0)
\end{array}
$$

Effect of Low Scale Gravity

Recently, it has been suggested [4] that the hierarchy problem *i.e.* the smallness of the ratio of electroweak scale to the Planck scale ($\simeq 10^{-17}$) can be resolved by introducing extra dimensions in the theory. In this case, the Planck scale (also called as string scale M_S) representing the scale for the gravitational interaction can be lowered to the electroweak scale with the condition that the strong effect of gravity remains restricted only to the extra dimensions. This has interesting theoretical implication on the Z-pair production, since the cross section for the process can be increased or decreased due to contribution from the graviton exchange diagram and it's interference with the SM diagram.

However, from our measured ZZ cross section [7], no evidence for such particles is found, and a lower limit at 95% confidence level is set on M_S of the theory for two different scenario:

$$
\begin{array}{lcl}
M_S > 0.67 \text{ TeV} & : & \lambda = +1 \\
M_S > 0.73 \text{ TeV} & : & \lambda = -1
\end{array}
$$

The factor λ is introduced to absorb any model dependence on the coupling whose absolute value is restricted to unity for the result listed above. The (+/−) sign indicates constructive or destructive interference with the SM amplitude.

Study of di-leptons recoiling against hadronic system

LEP has provided a unique opportunity to study the four-fermion final states originating from neutral current processes in $\rm e^+e^-$ interaction at several energy domain. In addition to offering experimental test to the Standard Model, it has important discovery potential for particle produced in association with Z. L3 with it's excellent energy and momentum resolution to reconstruct the leptons, electron and muon in particular, is better placed to study the latter in the process, $\rm e^+e^- \rightarrow ZX$, where Z decays to $\ell^+\ell^-$ and X to $\rm f\bar{f}$. Keeping it in mind, $\rm q\bar{q}\ell^+\ell^-$ final states [8] are studied using the same set of data sample used for the ZZ analysis.

After some loose preselection cuts to get rid of obvious backgrounds, two separate sets of selection cuts are used for selecting the $q\bar{q}\ell^+\ell^-$ events in the low as well as high mass region. Because, the underlying physics and the background processes involved are quite different for these two regions. The low mass region is dominated by the $\gamma^\star$-mediated process, while in the region close to m_Z, the Z-mediated process takes over. For each region, a number of physics variables is chosen to discriminate the signal and background processes and the two selections are combined by a logical $\mathcal{OR}$. The selections are also optimised at higher centre-of-mass energies.

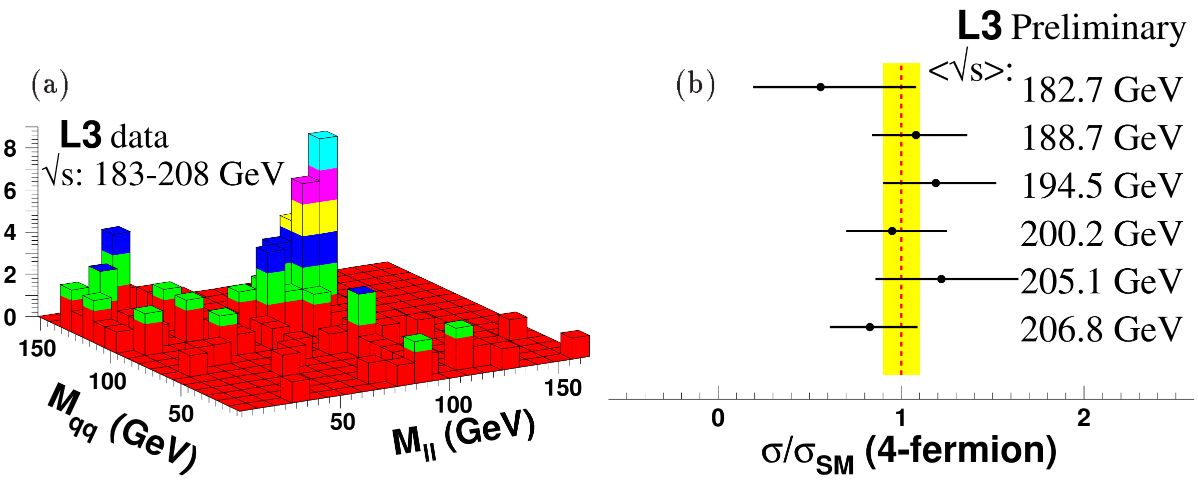

Figure 3: (a) *Two-dimensional distribution of the invariant and recoil mass spectra for the selected sample of* $q\bar{q}\ell^+\ell^-$ *events (different colour shade indicates the number of event in the box),* and (b) *ratio of measured four-fermion cross section for* $q\bar{q}\ell^+\ell^-$ *final state to the Standard Model prediction. The yellow band represents relative error of 10% on the prediction.*

Figure 3 shows the two-dimensional distribution of the invariant and the recoil mass of lepton pair (di-jet mass in our case) as well as the ratio of four-fermion cross section to the Standard Model value. Our result on the cross section is found to be well compatible with the Standard Model prediction. Also, no significant structure is observed in the di-lepton invariant or recoil mass spectra.

Reference

[1] S.L. Glashow, Nucl. Phys. **22** (1961) 579;
S. Weinberg, Phys. Rev. Lett. **19** (1967) 1264;
A. Salam, "Elementary Particle Theory", ed. N. Svartholm, (1968) 367.

[2] K. Hagiwara *et al.*, Nucl. Phys. **B282** (1987) 253;
A. Denner *et al.*, Nucl. Phys. **B306** (1988) 221;
G. Altareli *et al.*, Physics at LEP2, CERN 96-01.

[3] G.J. Gounaris *et al.*, Phys. Rev. **D61** (2000) 073013;
J. Alcaraz *et al.*, Phys. Rev. **D61** (2000) 075006.

[4] N. Arkani-Hamed *et al.*, Phys. Lett. **B429** (1998) 263;
K. Agashe and N.G. Deshpande, Phys. Lett. **B456** (1999) 60.

[5] L3 Collab., B. Adeva *et al.*, Nucl. Inst. Meth. **A289** (1990) 35;
L3 Collab., M. Chemarin *et al.*, Nucl. Inst. Meth. **A349** (1994) 345;
L3 Collab., M. Acciarri *et al.*, Nucl. Inst. Meth. **A351** (1994) 300;
L3 Collab., G. Basti *et al.*, Nucl. Inst. Meth. **A374** (1996) 293;
L3 Collab., A. Adam *et al.*, Nucl. Inst. Meth. **A383** (1996) 342.

[6] L3 Collab., M. Acciarri *et al.*, Phys. Lett. **B450** (1999) 281;
L3 Collab., M. Acciarri *et al.*, Phys. Lett. **B465** (1999) 363;
L3 Collab., M. Acciarri *et al.*, Phys. Lett. **B497** (2001) 23;
G.B. Mohanty, L3 Note # 2542l (2000);
Contrib. to the summer conferences 2001, L3 Note # 2696 (2001);
T. Aziz and G.B. Mohanty, L3 Note # 2726 (2002).

[7] L3 Collab., M. Acciarri *et al.*, Phys. Lett. **B464** (1999) 135;
S. Mele and E. Sánchez, Phys. Rev. **D61** (2000) 117901;
E. Sánchez, in *private communication.*

[8] L3 Collab., A. Adam *et al.*, Phys. Lett. **B321** (1994) 283;
L3 Collab., M. Acciarri *et al.*, Phys. Lett. **B413** (1997) 191;
"Status Report on Four-fermion final states", presented by G.B. Mohanty at L3 Extended Analysis Meeting, CERN, Sep 10-11 2001;
T. Aziz and G.B. Mohanty, L3 Note # 2739 (2002)

STATEMENT BY THE CANDIDATE

As required by the University Regulation No. R. 2190, I wish to state that the work embodied in this thesis titled **Study of Z-Boson Pair Production and Search for Physics Beyond Standard Model at LEP-II** forms my own contribution to the research work carried out under the guidance of **Prof. Tariq Aziz** at the Tata Institute of Fundamental Research. This work has not been submitted for any other degree of this or any other University. Whenever references have been made to previous works of others, it has been clearly indicated as such and included in the Bibliography.

Signature of Candidate
Name: Gagan Bihari Mohanty

Certified by,

Signature of Supervisor
Name: Prof. Tariq Aziz

Chapter 1

Introduction

It is the goal of modern physics to achieve reduction of nature's complexity to as few as possible fundamental principles. The method is increasing abstraction, the tool mathematics, the input experimental observations and the result unification of distinct phenomena up to that date. An important success pointing in that direction is the unified formulation of Maxwell's theory of electromagnetism [1] and the weak interaction, known as *Standard Model* of Electroweak Interactions.

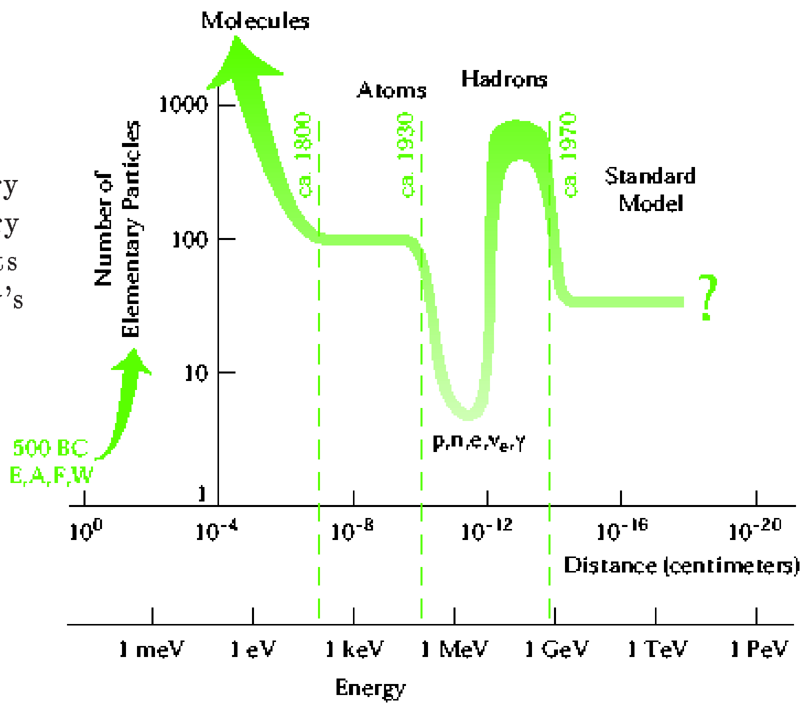

Figure 1.1: A schematic history of the concept of an elementary constituent: from four elements of the ancient Greeks to today's Standard Model.

Started with the discovery of radioactivity by Becquerel in 1896 [2], the weak interaction was put on a sound footing by Fermi, with an elegant model of contact interaction [3]. The structure of weak interactions was further clarified with the theoretical consideration of parity violations by Lee and Yang [4]. Soon thereafter, parity violation was experimentally confirmed in the famous Wu experiment [5]. This was when Fermi's original pure vector currents, constructed along the lines of QED[1], were replaced by a (V–A) structure [6]. Although very successful in low energy limit, Fermi's theory of weak interaction ran into a unitarity problem at high energy. Answer to this puzzle was found by introducing massive vector bosons into the theory. Apart from two charged bosons, W^+ and W^-, the presence of a neutral partner Z became imminent to prevent further anomalies. A first hint for the existence of the massive gauge boson came with the observation of neutral current reaction, $\bar{\nu}_\mu e^- \rightarrow \bar{\nu}_\mu e^-$, at CERN in 1973 [7]. The direct observation of the gauge bosons, $W^\pm$ and Z, was again reported at CERN by the UA1 and UA2 collaborations [8]. In addition to bringing massive gauge bosons and parity violation into picture, weak interaction also threw open challenge to the validation of one of the key symmetry operations. That is, the combined operation of parity (P) and charge conjugation (C), or CP operation which is thought to be a good quantum number for all interactions. There was no contradictory evidence against this postulate, until the discovery of CP violation in the neutral kaon system in 1964 [9]. It took another 10 years for Kobayashi and Maskawa to suggest that the CP violation could be explained via three generations of fermion families, interwoven with a phase factor [10]. With this much of historical perspective, let's now discuss some of the intriguing features of the Standard Model (SM) to be addressed in this thesis.

The Standard Model of electroweak interactions represents a renormalisable and non-abelian gauge theory that is invariant under a local gauge transformations of the symmetry group, $SU(2)_L \otimes U(1)_Y$. Along with the $SU(3)_C$ gauge group of quantum chromodynamics (QCD) [11] that guides all the sub-nuclear phenomena, the electroweak theory as proposed by Glashow, Salam and Weinberg [12] forms the basis of our current understanding of the theory of elementary particles. The Large Electron Positron (LEP) collider at CERN, with its large data samples collected at energies that were never realised earlier in an e^+e^- collision, is an ideal laboratory to test the predictions of the Standard Model. One of the major areas to be explored at LEP is the self-interactions among the gauge bosons which is envisaged due to non-abelian nature of the associated gauge group. The reaction, $e^+e^- \rightarrow ZZ$, provides an opportunity to test the predictions of Standard Model by validating the absence of anomalous couplings, V_{ZZZ} and $V_{ZZ\gamma}$ (absent at tree level). Possible deviations from the SM expectations in the form of change in the measured cross section or modified angular distribution of the produced Z-boson, will open the gate for new physics. Another strong motivation for studying this process is in connection to the production of Higgs boson at LEP. The higgs boson, the end product of the spontaneous breaking of $SU(2)_L \otimes U(1)_Y$ symmetry, is responsible for generating mass for the gauge bosons and chiral fermions. The process, $e^+e^- \rightarrow ZZ$, is the most dominant and irreducible background to Higgs search at LEP. It also tests the detector capability (which is in our case the L3 detector) for discovering Higgs particle. One of the conceptual drawbacks with Standard Model is that it does not incorporate gravity. Moreover, it is

[1]QED is the quantum field theoretic formulation of Maxwell's theory of electromagnetism

associated with a hierarchy between the electroweak and gravitational interactions. A possible remedy to this problem could be found out by introducing extra dimensions into the theory, which will lead to test the predictions of standard gravity at very low scale (Low Scale Gravity). Again the Z-boson pair production can be used to test the validity of this LSG-inspired model.

The thesis is organised as follows. The first three chapters are introductory in nature. *Theoretical Framework* (Chapter 2) deals with present theoretical understanding in the form of Standard Model taking Z-boson pair production as a case study. *Experimental Apparatus* (Chapter 3) gives an overview of the LEP collider and L3 detector. In Chapter 4, the issue of *Reconstruction and Simulation* has been briefly touched upon. The following four chapters deal with the analysis and measurement which form the major part of the thesis. *Selection of* $\mathrm{e^+e^-} \rightarrow \mathrm{ZZ} \rightarrow \mathrm{q\bar{q}}\ell^+\ell^-$ *Events* (Chapter 5), describes in detail the optimal selection methodology developed for selecting the $\mathrm{e^+e^-} \rightarrow \mathrm{ZZ}$ event, where one Z decays to $\mathrm{q\bar{q}}$ and other to $\ell^+\ell^-$. *Measurements of the Cross Section* for the process and inclusive $\mathrm{b\bar{b}X}$ final state are elucidated in Chapter 6. The selected sample of Z-pair events is used to *Search for Physics beyond Standard Model* in the sector of anomalous trilinear gauge couplings and low scale gravity in Chapter 7. Neutral current four-fermion final state is studied over the full accessible mass range for $\mathrm{q\bar{q}}\ell^+\ell^-$ final state. Result of which, forms part of *Neutral Current Four-Fermion Production* (Chapter 8). Finally, *Summary and Outlook* (Chapter 9) summarises the thesis.

References

[1] J.C. Maxwell, “Treatise on Electricity and Magnetism”, 3rd edition (1891).

[2] H. Becquerel, C.R. Acad. Sci. (Paris) **122** (1896) 501.

[3] E. Fermi, Z. Phys. **88** (1934) 161.

[4] T.D. Lee and C.N. Yang, Phys. Rev. **104** (1956) 254.

[5] C.S. Wu *et al.*, Phys. Rev. **105** (1957) 1413.

[6] R.P. Feynman and M. Gell-Mann, Phys. Rev. **109** (1958) 193;
E.C.G. Sudarshan and R.E. Marshak, Phys. Rev. **109** (1958) 1860.

[7] Gargamelle Collab., F.J. Hasert *et al.*, Phys. Lett. **B46** (1973) 138;
Gargamelle Collab., F.J. Hasert *et al.*, Nucl. Phys. **B73** (1974) 1.

[8] UA1 Collab., G. Arnison *et al.*, Phys. Lett. **B122** (1983) 103;
UA1 Collab., G. Arnison *et al.*, Phys. Lett. **B126** (1983) 398;
UA2 Collab., M. Banner *et al.*, Phys. Lett. **B122** (1983) 476;
UA2 Collab., P. Bagnaia *et al.*, Phys. Lett. **B129** (1983) 130.

[9] J.H. Christenson *et al.*, Phys. Rev. Lett. **13** (1964) 138.

[10] N. Cabibbo, Phys. Rev. Lett. **10** (1963) 531;
M. Kobayashi and T. Maskawa, Prog. Theor. Phys. **49** (1973) 652.

[11] J.D. Bjorken, Phys. Rev. Lett. **16** (1966) 408;
R.P. Feynman, Phys. Rev. Lett. **23** (1969) 1515;
H. Fritzsch, M. Gell-Mann and H. Leutwyler, Phys. Lett. **B47** (1973) 365;
D.J. Gross and F. Wilczek, Phys. Rev. Lett. **30** (1973) 1343;
S. Weinberg, Phys. Rev. Lett. **31** (1973) 494;
H.D. Politzer, Phys. Rev. Lett. **30** (1973) 1346;
G. ’t Hooft, Nucl. Phys. **B33** (1971) 173.

[12] S.L. Glashow, Nucl. Phys. **22** (1961) 579;
S. Weinberg, Phys. Rev. Lett. **19** (1967) 1264;
A. Salam, “Elementary Particle Theory”, ed. N. Svartholm, (1968) 367.

Chapter 2

Theoretical Framework

In this chapter, a formal theoretical background needed to describe and interpret the measurements described later is given.

2.1 Standard Model

The Standard Model of electroweak interactions [1] is based on the composite gauge group $SU(2)_L \otimes U(1)_Y$, where the generators of $SU(2)_L$ correspond to the three components of weak isospin T_i and $U(1)_Y$ to the weak hypercharge Y. These are related to the electric charge by $Q = T_3 + Y/2$. The Lagrangian describing the electroweak interactions is

$$\begin{aligned}\mathcal{L}_{EW} &= -\frac{1}{4}W^a_{\mu\nu}W_a^{\mu\nu} - \frac{1}{4}B_{\mu\nu}B^{\mu\nu} + i\bar{\psi}_j\gamma^\mu D_\mu\psi_j \\ &+(D_\mu\Phi)(D^\mu\Phi)^\dagger - \mu^2\Phi^\dagger\Phi - \lambda(\Phi^\dagger\Phi)^2 \\ &+\lambda_{\ell_k}\bar{L}_{L_k}\Phi\,\ell_{R_k} + \lambda_{\mathrm{u}_{jk}}\bar{Q}_{L_j}\tilde{\Phi}\,\mathrm{u}_{R_k} + \lambda_{\mathrm{d}_{jk}}\bar{Q}_{L_j}\Phi\,\mathrm{d}_{R_k} + h.c., \end{aligned} \tag{2.1}$$

with the field strength tensors

$$\begin{aligned} W^a_{\mu\nu} &= \partial_\mu W^a_\nu - \partial_\nu W^a_\mu + g\epsilon^{abc}W_{b\mu}W_{c\nu}, \\ B_{\mu\nu} &= \partial_\mu B_\nu - \partial_\nu B_\mu, \end{aligned} \tag{2.2}$$

for the three non-abelian fields of $SU(2)_L$ and the single abelian gauge field associated with $U(1)_Y$, respectively. The covariant derivative is

$$D_\mu = \partial_\mu - igT_aW^a_\mu - ig'\frac{Y}{2}B_\mu, \tag{2.3}$$

with g, g' being the $SU(2)_L, U(1)_Y$ coupling strength, respectively. The $SU(2)$ generators obey the usual commutation relation $[T_a, T_b] = i\epsilon_{abc}T_c$ and are related to Pauli spin matrices by $T_a = \tau_a/2$. The corresponding massless gauge fields form a weak isospin triplet with the charged fields being defined by $W^\pm_\mu = (W_1 \mp iW_2)_\mu/\sqrt{2}$, while the neutral component mixes with the abelian gauge field to form the physical states

$$\begin{aligned} Z_\mu &= W^3_\mu\cos\theta_w + B_\mu\sin\theta_w, \\ A_\mu &= B_\mu\cos\theta_w - W^3_\mu\sin\theta_w, \end{aligned} \tag{2.4}$$

	Families 1	2	3	Q ($\|e\|$)	T_3	Y
Leptons	$\begin{pmatrix}\nu_e \\ e\end{pmatrix}_L$	$\begin{pmatrix}\nu_\mu \\ \mu\end{pmatrix}_L$	$\begin{pmatrix}\nu_\tau \\ \tau\end{pmatrix}_L$	0 -1	$+\frac{1}{2}$ $-\frac{1}{2}$	-1 -1
	e_R	μ_R	τ_R	-1	0	-2
Quarks	$\begin{pmatrix}u \\ d'\end{pmatrix}_L$	$\begin{pmatrix}c \\ s'\end{pmatrix}_L$	$\begin{pmatrix}t \\ b'\end{pmatrix}_L$	$+\frac{2}{3}$ $+\frac{1}{2}$	$-\frac{1}{3}$ $-\frac{1}{2}$	$+\frac{1}{3}$ $+\frac{1}{3}$
	u_R	c_R	t_R	$+\frac{2}{3}$	0	$+\frac{4}{3}$
	d'_R	s'_R	b'_R	$-\frac{1}{3}$	0	$-\frac{2}{3}$

Table 2.1: The classification of fermions into three families of weak isospin multiplets. The weak eigen-states (d', s', b') are obtained from the mass eigen-states (d, s, b) by CKM rotation. For each particle state, an antiparticle state which is obtained by charge conjugation exists.

where $\tan\theta_w = g'/g$ is the weak mixing angle.

To generate the left-handed structure of the charged current interaction, the $SU(2)$ symmetry is applied to left-handed fermion fields only. The fermion fields are thus given by

$$\psi_L: \quad L_{L_k} = \frac{1}{2}(1-\gamma_5)\begin{pmatrix}\nu_k \\ \ell_k\end{pmatrix}, \quad Q_{L_k} = \frac{1}{2}(1-\gamma_5)\begin{pmatrix}u_k \\ d'_k\end{pmatrix}, \tag{2.5}$$

for the $SU(2)_L$ left-handed doublets and

$$\psi_R: \quad \ell_{R_k} = \frac{1}{2}(1+\gamma_5)\ell_k, \quad u_{R_k} = \frac{1}{2}(1+\gamma_5)u_k, \quad d'_{R_k} = \frac{1}{2}(1+\gamma_5)d'_k, \tag{2.6}$$

for the right-handed singlets with k representing the family index. Each of the quarks appear in three colors *e.g.* u_R, u_B and u_G and the right-handed neutrinos do not exist in the model. The λ_i in Equation 2.1 are the Yukawa couplings of the quarks and leptons.

Masses for the non-abelian gauge fields and fermions are generated by the Higgs mechanism [2] via spontaneous symmetry breaking which preserves the renormalizability of the gauge theory [3]. The Higgs fields are complex scalar isodoublets (ϕ^+, ϕ^0) with electroweak interactions described by the second line in Equation 2.1. For the choice of $\mu^2 < 0$, the ground state of the theory is obtained when the neutral member of the Higgs doublet acquires a vacuum expectation value (*v.e.v.*),

$$<\Phi> \quad = \quad \frac{1}{\sqrt{2}}\begin{pmatrix}0 \\ v\end{pmatrix} \tag{2.7}$$

where v is given by $v^2 = -\mu^2/\lambda$. This non-vanishing *v.e.v.* selects a preferred direction in $SU(2)_L \otimes U(1)_Y$ space and simultaneously breaks the symmetry, however leaving $U(1)_{em}$ subgroup intact. ϕ^0 is then redefined by $\phi^0 = (H+v)/\sqrt{2}$, such that the physical field

H has a vanishing *v.e.v.* and positive mass squared. The remaining degrees of freedom, *i.e.*, the Goldstone bosons, are "gauged away" from the scalar sector, but essentially reappear in the gauge sector, providing the longitudinal modes for the W and Z bosons. An examination of the v^2 terms in the kinetic piece of the scalar Lagrangian reveals the mass terms for the physical gauge bosons,

$$m_{\mathrm{W}} = \frac{1}{2}gv, \quad m_{\mathrm{Z}} = \frac{v}{2}\sqrt{g^2 + g'^2}, \quad m_A = 0. \tag{2.8}$$

In order to obtain Quantum Electrodynamics (QED) the massless A_μ is identical with the

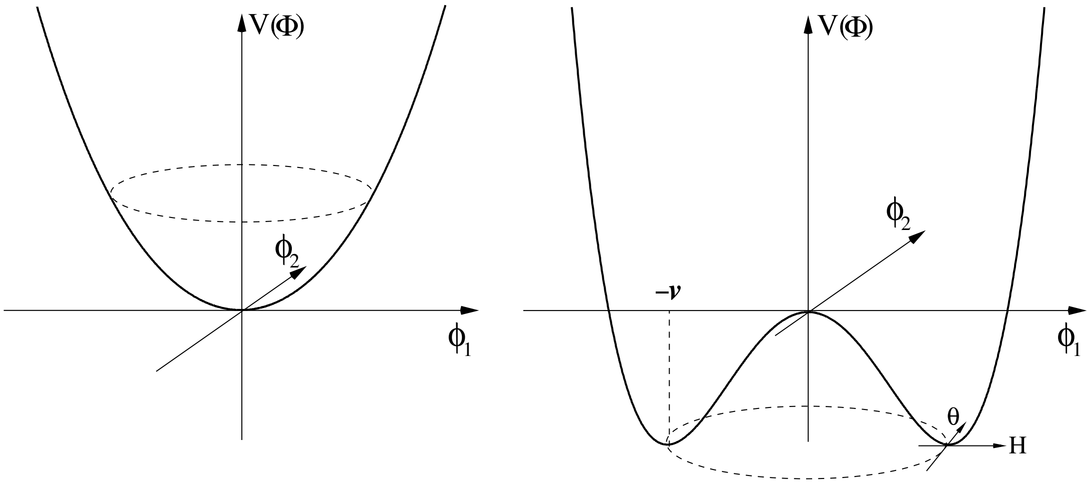

Figure 2.1: The shape of the Higgs potential V(Φ) as a function of ϕ_1 and ϕ_2 for the case of $\mu^2 > 0$ (left plot) and $\mu^2 < 0$ (right plot) with positive value of λ.

photon and $e = g \sin\theta_w = g' \cos\theta_w$. The electromagnetic and weak charged and neutral currents thus become

$$\begin{aligned} J_\mu^{em} &= \bar{\psi}\gamma_\mu Q\psi, \\ J_\mu^{CC} &= \bar{\psi}\gamma_\mu T_L^{\pm}\psi, \\ J_\mu^{NC} &= \bar{\psi}(T_{3L} - \sin^2\theta_w Q)\psi, \end{aligned} \tag{2.9}$$

Here, $T_L^{\pm} = (T_1 \pm iT_2)_L/\sqrt{2} = \tau^{\pm}/2$ operations act on the left handed isodoublets ψ_L, and vanish on ψ_R. Comparison with the Fermi theory of weak interaction yields the relation

$$\frac{G_F}{\sqrt{2}} = \frac{g^2}{8m_W^2}, \tag{2.10}$$

where G_F is the Fermi coupling constant. Equation 2.8 relates the gauge boson masses by $m_{\mathrm{Z}} = m_{\mathrm{W}}/\cos\theta_w$. Mass terms for the fermions, $m_{\mathrm{f}} = \lambda_{\mathrm{f}} v/\sqrt{2}$, are due to the physical Higgs–fermion interactions as enunciated in the last line of Equation 2.1. Diagonalization of the masses in the quark sector introduces Cabibbo-Kobayashi-Maskawa, or CKM matrix [4], which then appears in the hadronic weak charged current. The same analogy does not hold good in lepton sector, due to absence of right handed neutrino in the model.

Having briefly introduced the essential ingredients of the Standard Model, we now turn to examine its prediction for Z-boson pair production, the main subject of this thesis.

2.2 Z-boson Pair Production

In the Standard Model, a pair of Z-bosons is produced via t and u-channel electron exchange diagrams [5] as shown in Figure 2.2. These two diagrams are collectively known as NC02 diagrams, as they are part of the Neutral Current processes. Unlike W^+W^- case, there is no additional contribution from triple gauge boson vertices at tree level due to antisymmetric nature of the structure constant of the $SU(2)$ group.

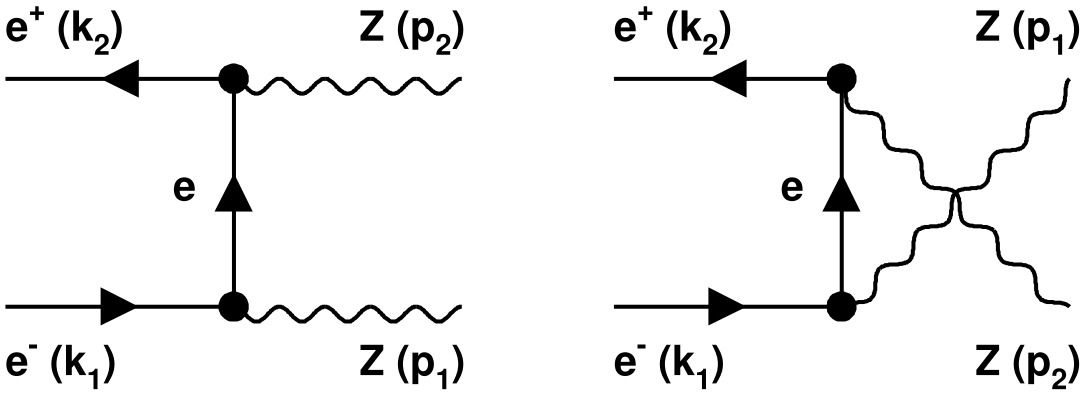

Figure 2.2: Feynman diagrams for the process $e^+e^- \to ZZ$ in the Standard Model.

The scattering matrix for the above diagrams is given by

$$\mathcal{M} \quad = \quad \bar{v}(k_2)T_{\mu\nu}u(k_1)\epsilon^{\mu\dagger}(p_2)\epsilon^{\nu}(p_1) \tag{2.11}$$

where $T_{\mu\nu}$ is the scattering amplitude. Assuming the mass of the electron is negligible[1],

$$T_{\mu\nu} \quad = \quad -i(\sqrt{2}m_Z^2 G_F)(g_V^2 + g_A^2 + 2g_V g_A \gamma_5)\left(\gamma_\mu \frac{1}{\not{l}_1}\gamma_\nu + \gamma_\nu \frac{1}{\not{l}_2}\gamma_\mu\right) \tag{2.12}$$

where $l_1^2 = t = (k_1 - p_1)^2 = (p_2 - k_2)^2$ and $l_2^2 = u = (k_1 - p_2)^2 = (p_1 - k_2)^2$. g_V and g_A are the vector and axial vector coupling constants of the electron and are given by $g_V = -\frac{1}{2} + 2\sin^2\theta_w$ and $g_A = -\frac{1}{2}$. The unpolarised differential cross section for the process can be calculated as

$$\frac{d\sigma}{dt} \quad = \quad \frac{4\pi\alpha^2 m_Z^2 G_F^2}{s^2}\frac{g_V^4 + g_A^4 + 6g_V^2 g_A^2}{e^4}\left[\frac{t}{u} + \frac{u}{t} + \frac{4m_Z^2 s}{ut} - m_Z^4\left(\frac{1}{t^2} + \frac{1}{u^2}\right)\right] \tag{2.13}$$

[1] The s-channel Higgs exchange diagram can be neglected.

where $s = (k_1 + k_2)^2 = (p_1 + p_2)^2$. The total cross section is therefore,

$$\sigma(\mathrm{e^+e^-} \rightarrow \mathrm{ZZ}) = \frac{1}{2!}\int_{t_{min}}^{t_{max}} \frac{d\sigma}{dt} dt,$$
$$t_{max,min} = m_\mathrm{Z}^2 - \frac{1}{2}s(1 \pm \beta_\mathrm{Z}) \tag{2.14}$$

with the factor 2! coming due to identical bosonic final state. β_Z is the velocity of the Z-boson in the centre-of-mass frame. After carrying out the integration, the expression for total cross section becomes

$$\sigma(\mathrm{e^+e^-} \rightarrow \mathrm{ZZ}) = \frac{8\pi\alpha^2 m_\mathrm{Z}^2 G_F^2}{s} \frac{g_V^4 + g_A^4 + 6g_V^2 g_A^2}{e^4}\left[\frac{1+4m_\mathrm{Z}^4/s^2}{1-2m_\mathrm{Z}^2/s}\log\left(\frac{1+\beta_\mathrm{Z}}{1-\beta_\mathrm{Z}}\right) - \beta_\mathrm{Z}\right] \tag{2.15}$$

Figure 2.3 shows the evolution of the expected cross section for the process, $\mathrm{e^+e^-} \rightarrow \mathrm{ZZ}$, with centre-of-mass energy ($\sqrt{s}$). The drop in the cross section after crossing the ZZ production threshold, is due to the factor of $(1/s)$ in Equation 2.15.

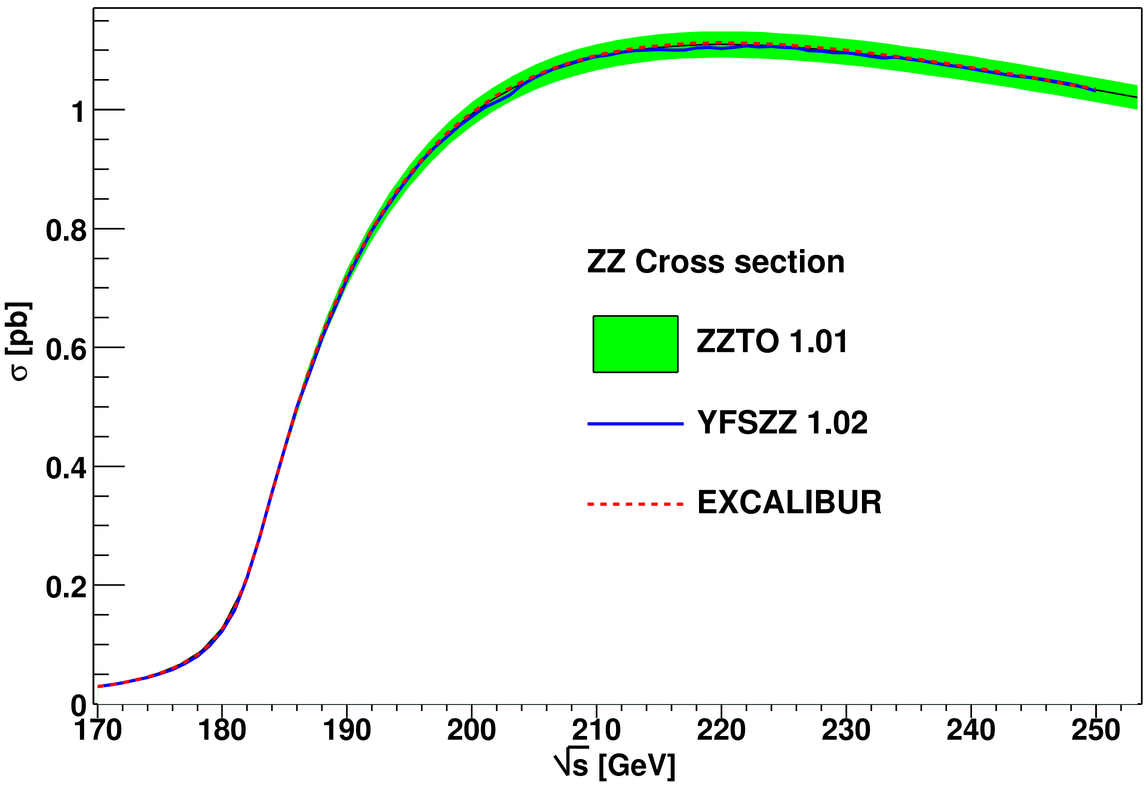

Figure 2.3: Cross section for the process $\mathrm{e^+e^-} \rightarrow \mathrm{ZZ}$ as a function of centre-of-mass energy with the green band indicating the theoretical uncertainties.

The differential angular distribution, $d\sigma/d\cos\theta_\mathrm{Z}$, can be easily calculated by substituting $dt = s\beta_\mathrm{Z} d\cos\theta_\mathrm{Z}/2$ in Equation 2.13. It is expected to peak in the forward and backward directions ($\cos\theta_\mathrm{Z} = \pm 1$).

2.3 Anomalous Trilinear Gauge Couplings

The coupling of a virtual photon or Z boson to ZZ final state through ZZγ and ZZZ vertices, as shown in Figure 2.4 is not forbidden by any fundamental principle. It is, due to $SU(2)_L$ part of the composite gauge symmetry which is rather known to be an approximate symmetry. In general, one may expect non-vanishing interactions of three

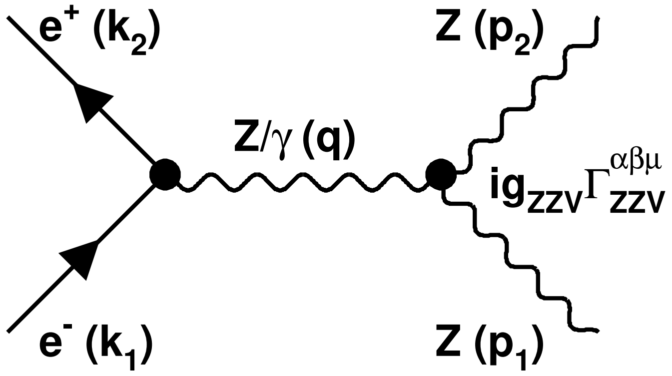

Figure 2.4: Diagrams with anomalous ZZγ and ZZZ couplings contributing to the $e^+e^- \to$ ZZ process. Here $\Gamma^{\alpha\beta\mu}_{ZZV}$ represents the anomalous vertex function.

neutral gauge bosons, which will pave way for Z-pair production via s-channel photon or Z exchange. However, in case of resonant Z-pair production due to Bose symmetry and electromagnetic gauge invariance, the form of such interactions is expressed in terms of only four terms [6],

$$\Gamma^{\alpha\beta\mu}_{ZZV}(p_1, p_2, q) = \frac{s - m_V^2}{m_Z^2}\left[i f_4^{ZZV}(q^\alpha g^{\mu\beta} + q^\beta g^{\mu\alpha}) + i f_5^{ZZV}\epsilon^{\mu\alpha\beta\rho}(p_1 - p_2)_\rho\right] \tag{2.16}$$

with $q = (k_1 + k_2) = (p_1 + p_2)$. In principle, five additional terms should be considered if at least one of the final Z's is off-shell. They are, however, suppressed by orders of $m_Z\Sigma_Z/\Lambda^2$ with Λ denoting the scale related to new physics. A non-zero value for f_4^V leads to a C-violating, P-conserving process, while terms associated f_5^V are both C and P-violating. Using again the formalism adopted in Reference [6], the explicit expressions for the anomalous contributions can be obtained;

$$M^{f_4^V}_{AC}(\sigma, \bar{\sigma}, \lambda_{Z_1}, \lambda_{Z_2}) = -ief_4^V g_\sigma^{Vee}\frac{s}{m_Z^2}\delta_{\sigma,-\bar{\sigma}}\left[\epsilon^{0\star}_{Z_1}(\epsilon^{1\star}_{Z_2} + i\sigma\epsilon^{2\star}_{Z_2}) + \epsilon^{0\star}_{Z_2}(\epsilon^{1\star}_{Z_1} + i\sigma\epsilon^{2\star}_{Z_1})\right] \tag{2.17}$$

$$M^{f_5^V}_{AC}(\sigma, \bar{\sigma}, \lambda_{Z_1}, \lambda_{Z_2}) = -ief_5^V g_\sigma^{Vee}\frac{\sqrt{s}}{m_Z^2}\delta_{\sigma,-\bar{\sigma}}\left(\epsilon^{1\alpha\beta\rho} + i\sigma\epsilon^{2\alpha\beta\rho}\right)\epsilon^\star_{Z_1\alpha}\epsilon^\star_{Z_2\beta}(p_{1\rho} - p_{2\rho}) \tag{2.18}$$

Effect of anomalous couplings in ZZ events can be realised in number of ways:

- change in the observed cross section for the process, $e^+e^- \to$ ZZ,
- modification of the angular distribution of the Z, and

- change in the average polarisation content of the Z.

Figure 2.5 shows the change in the polar angle distribution of the Z due to contributions from various anomalous couplings. As it is seen, at large value of $|\cos\theta_Z|$, the cross section is expected to rise significantly. However, given the small number of $e^+e^- \to ZZ$ events produced with the data sample we are dealing with, the differential angular distribution does not show the expected sensitivity. Thus we compare the integrated number of expected events with non-zero values for different anomalous couplings with the data, result of which is described in Chapter 7.

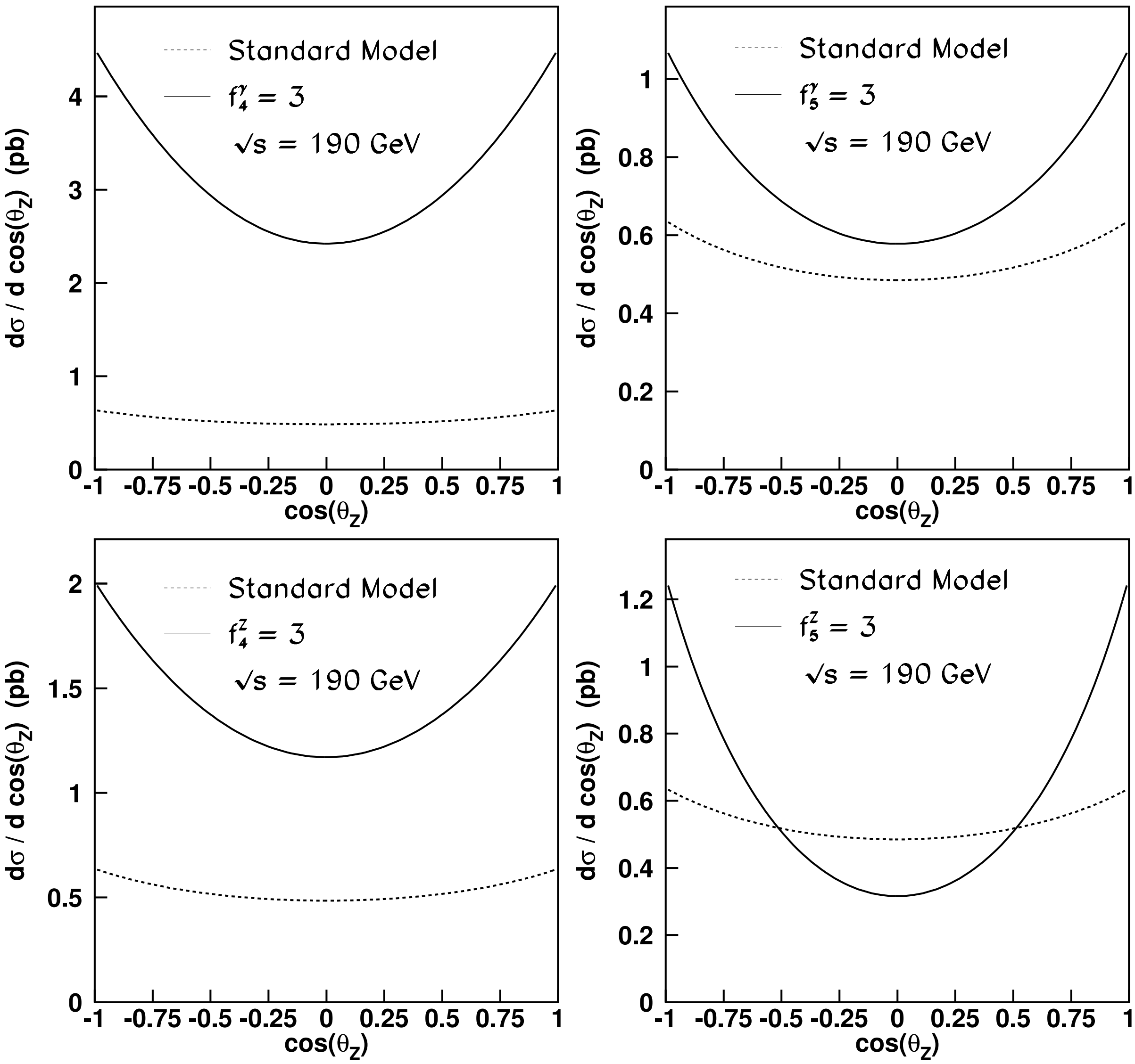

Figure 2.5: Modified angular distributions of the Z in presence of non-zero anomalous couplings. The dotted line is the Standard Model expectation and the solid line is the expectation in presence of one of the anomalous couplings.

2.4 Low Scale Gravity

It has been recently proposed [7, 8] that the hierarchy problem, *i.e.*, the vast difference between electroweak scale ($\approx 10^2$ GeV) and the scale at which gravitational interaction becomes strong, the Planck scale ($\approx 10^{19}$ GeV), could be solved by introducing Low Scale quantum Gravity (LSG) to the theory. According to the LSG-inspired model, the graviton can propagate in the $(4+n)$ dimensions with its strong effect constrained only to n extra dimensions. However, the SM particles are restricted to the usual four dimensions.

The presence of extra dimensions leads to significant deviation in the behaviour of gravity, such that the gravitational potential between two test masses m_1 and m_2 at a relative distance r will be,

$$V(r) \approx -\frac{m_1 m_2}{M_S^{n+2}} \frac{1}{r^{n+1}} \tag{2.19}$$

with M_S representing the effective Planck mass in the $(4+n)$ dimensions, also called "String scale". As we do not feel the effect of extra dimensions in day-to-day life, they must be in compact form being noticeable only at a distance much smaller than the size R of the dimensions. Equation 2.19 is then only valid for $r \ll R$. For masses placed farther apart *i.e.* $r \gg R$, we would get back the usual $1/r$ behaviour:

$$V(r) \approx -\frac{m_1 m_2}{M_S^{n+2} R^n} \frac{1}{r} \tag{2.20}$$

Comparing the above equation with standard expression for the gravitation potential, the following relation between the Planck scale and String scale is realised,

$$M_{Pl}^2 \approx R^n M_S^{n+2}. \tag{2.21}$$

Here the constant of proportionality depends on the topology of the extra dimensions. From Equation 2.21, $n = 1$ scenario is automatically excluded as it implies value of R

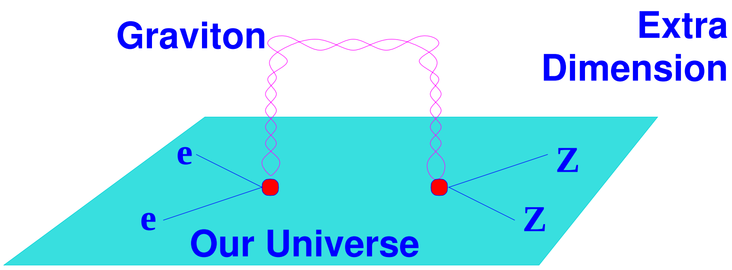

Figure 2.6: The s-channel graviton exchange diagram leading to the process $e^+e^- \to ZZ$.

comparable to the dimension of our solar system. However, for the case of $n = 2$ the transition of gravitational potential from $1/r$ to $1/r^3$ form will take place at a distance below 1 mm. This scenario has interesting theoretical implication for the process, $e^+e^- \to ZZ$.

In addition to the NC02 diagrams, additional contribution will come from the s-channel graviton exchange diagram (Figure 2.6) with coupling strength of the graviton proportional to $1/M_S$. The corresponding matrix element is given by [8],

$$\mathcal{M}_{\rm grav}(\kappa, \epsilon_+, \epsilon_-, s, t) \;=\; \frac{\lambda}{M_S^4}\, 4\left[s\mathcal{M}_1^\kappa - s(1-\beta_{\rm Z}\cos\theta_{\rm Z})(\mathcal{M}_3^\kappa - \mathcal{M}_2^\kappa)\right] \qquad (2.22)$$

where $\beta_{\rm Z}$ is the velocity of Z, $\theta_{\rm Z}$ is the angle between e^+ and Z in the centre-of-mass frame, κ is the electron helicity and ϵ_+ and ϵ_- are the polarisations of the Z bosons. The factor λ is introduced to absorb any model dependence which, in our discussion will be treated as ± 1. The sign of λ determines whether the interference with the SM amplitude gives a constructive or destructive contribution to the total cross section. Figure 2.7 shows the

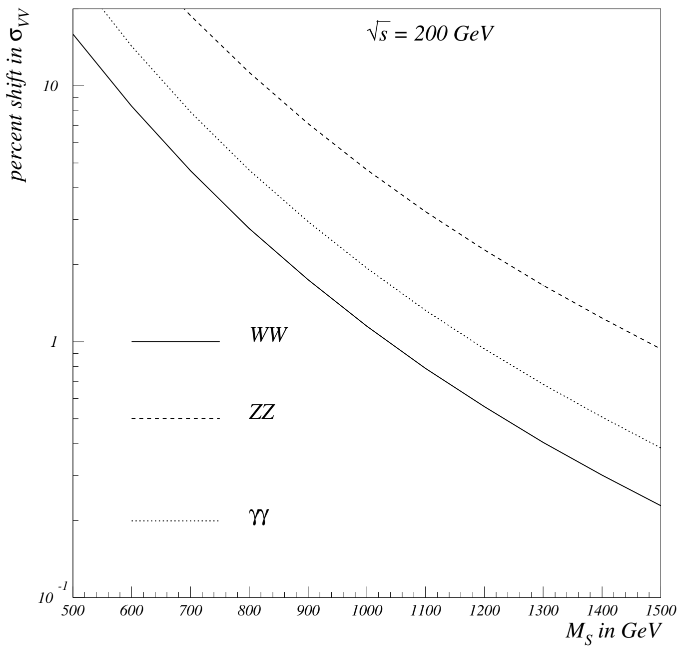

Figure 2.7: The deviation in percent of the cross section for $e^+e^- \to W^+W^-, ZZ$ and $\gamma\gamma$ from the SM prediction as a function of M_S at $\sqrt{s} = 200$ GeV. For $\gamma\gamma$ case, a cut $\cos\theta \le 0.9$ is imposed.

expected relative change in $\sigma_{\rm ZZ}$ at $\sqrt{s} = 200$ GeV for different M_S hypothesis.

2.5 Neutral Current Four-Fermion Production

The process $e^+e^- \to ZZ$, leading to four-fermion final state, is a subset of more generic four-fermion final states [9] originating from the neutral current processes. All possible classes of such diagrams are shown in Figure 2.8(a). Largest contribution comes from the multiperipheral diagram with two quasi-real photons exchanged leading to forward electrons plus a $f\bar{f}$ pair with non-resonant structure. However for the present study, we are not interested in this process. Rather we concentrate on the NC08 set of conversion diagrams comprising of ZZ (NC02), $Z\gamma^\star$ and $\gamma^\star\gamma^\star$ (NC06) processes. These processes play dominant role for the final state without electrons. In case of electrons in the final state, the dominant process is the bremsstrahlung diagram with t-channel photon exchange.

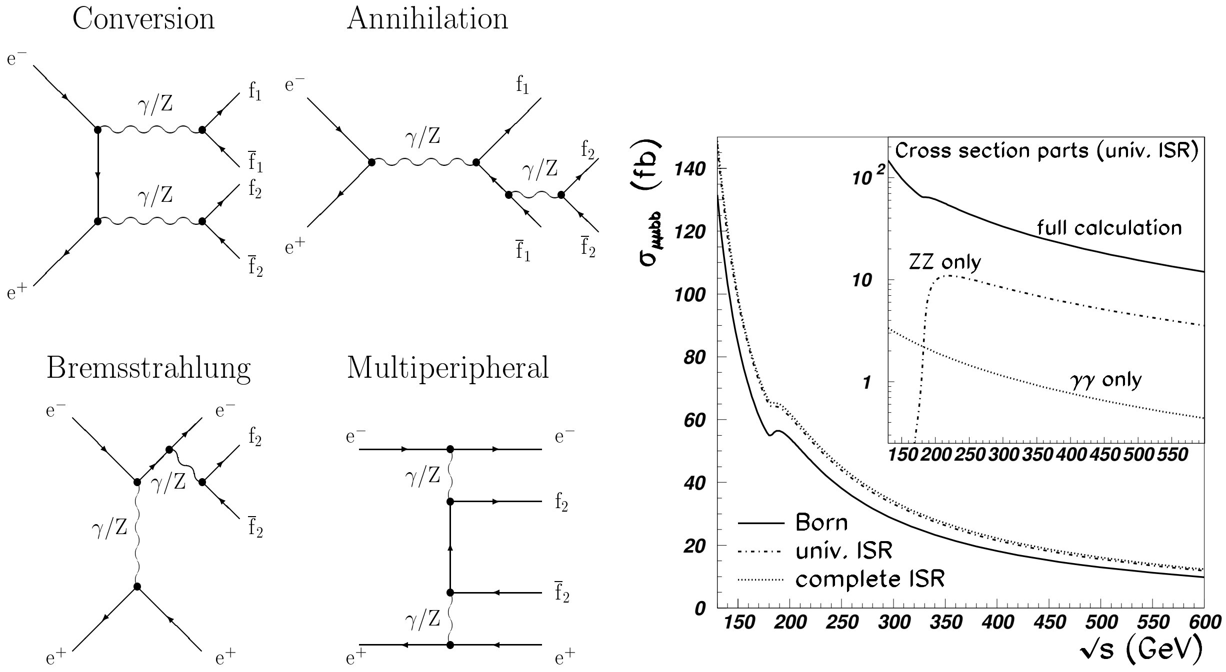

(a) Feynman diagrams for NC 4F production.

(b) Typical NC08 production cross section.

Figure 2.8: Schematic Feynman diagrams for the neutral current four-fermion production process and typical NC08 cross section for the process $e^+e^- \rightarrow b\bar{b}\mu^+\mu^-$.

In Figure 2.8(b), individual contributions from NC02 and NC06 diagrams as well as the contribution from the full NC08 diagram are shown for a typical four fermion production process, $e^+e^- \rightarrow b\bar{b}\mu^+\mu^-$.

References

[1] S.L. Glashow, Nucl. Phys. **22** (1961) 579;
S. Weinberg, Phys. Rev. Lett. **19** (1967) 1264;
A. Salam, "Elementary Particle Theory", ed. N. Svartholm, (1968) 367;
F. Halzen and A.D. Martin, "Quarks & Leptons", John Wiley & sons (1983).

[2] P.W. Higgs, Phys. Lett. **12** (1964) 132; Phys. Rev. Lett. **13** (1964) 508;
F. Englert and R. Brout, Phys. Rev. Lett. **13** (1964) 321;
G.S. Guralnik *et al.*, Phys. Rev. Lett. **13** (1964) 585.

[3] M.J.G. Veltman, Nucl. Phys. **B7** (1968) 637;
G. 't Hooft, Nucl. Phys. **B35** (1971) 167;
G. 't Hooft and M.J.G. Veltman, Nucl. Phys. **B44** (1972) 189.

[4] N. Cabibbo, Phys. Rev. Lett. **10** (1963) 531;
M. Kobayashi and T. Maskawa, Prog. Theor. Phys. **49** (1973) 652.

[5] R.W. Brown and K.O. Mikaelian, Phys. Rev. **D19** (1979) 922;
K. Hagiwara *et al.*, Nucl. Phys. **B282** (1987) 253;
A. Denner *et al.*, Nucl. Phys. **B306** (1988) 221.

[6] G.J. Gounaris *et al.*, Phys. Rev. **D61** (2000) 073013;
J. Alcaraz *et al.*, Phys. Rev. **D61** (2000) 075006.

[7] N. Arkani-Hamed *et al.*, Phys. Lett. **B429** (1998) 263;
G.F. Giudice *et al.*, Nucl. Phys. **B544** (1999) 3;
J.L. Hewett, Phys. Rev. Lett. **82** (1999) 4765.

[8] K. Agashe and N.G. Deshpande, Phys. Lett. **B456** (1999) 60.

[9] G. Altareli *et al.*, "Physics at LEP2", CERN 96-01, Volume 1.

Chapter 3

Experimental Apparatus

The Large Electron Positron (LEP) collider has been used to produce e^+e^- interactions at highest energies. To record a variety of particles produced in these interactions, the L3 detector is used. A brief description of the LEP collider and L3 detector is given here.

3.1 LEP Collider

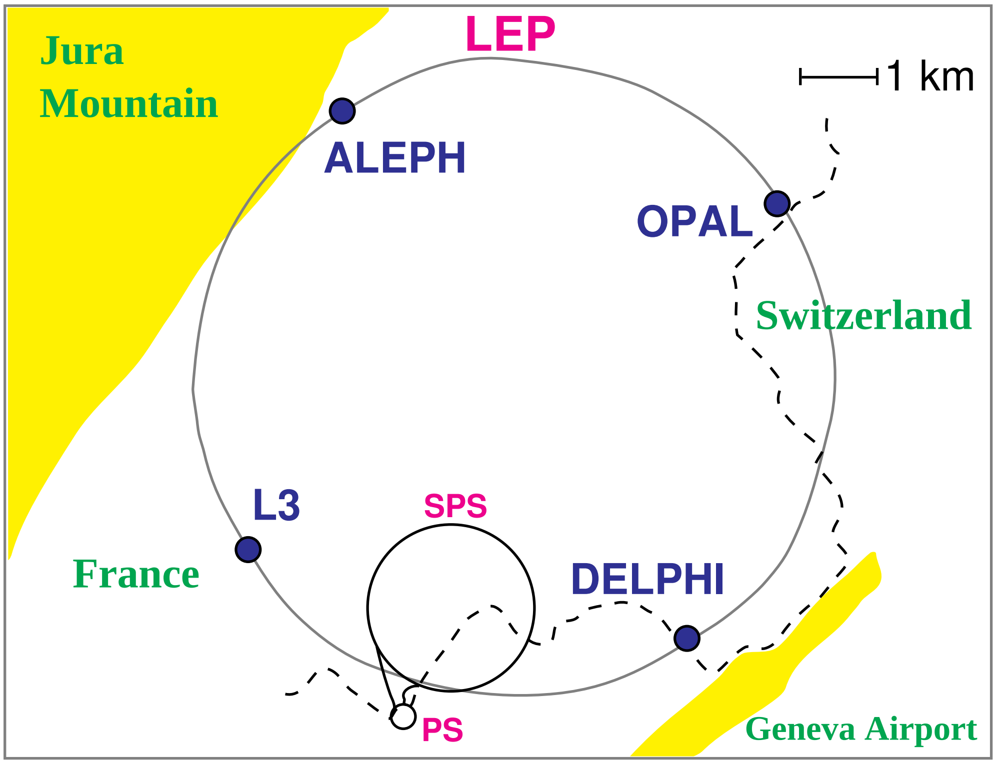

Figure 3.1: Schematic view of the LEP site.

The LEP collider [1] is located at the European Laboratory for Particle Physics (CERN) near Geneva, straddling the French-Swiss border at an average depth of about 100 m (see Figure 3.1). With a circumference of 26.67 km, it is the largest electron–positron collider built so far. Some of the important LEP parameters [2] are described in Table 3.1.

Shape	:	8 straight + 8 circular
Experiments	:	ALEPH, DELPHI, L3, OPAL
Data taking period	:	1989 – 2000
Bunch crossing time (μs)	:	22 (4 $\times$ 4 bunch mode)
Beam size : (σ_x, σ_y), σ_z	:	$(150, 10)\,\mu$m, 1 cm at LEP-I
Beam current (mA)	:	4/2.5 (LEP-I/II)
Beam Lifetime (hr)	:	10/5 (LEP-I/II)

Table 3.1: The LEP parameters.

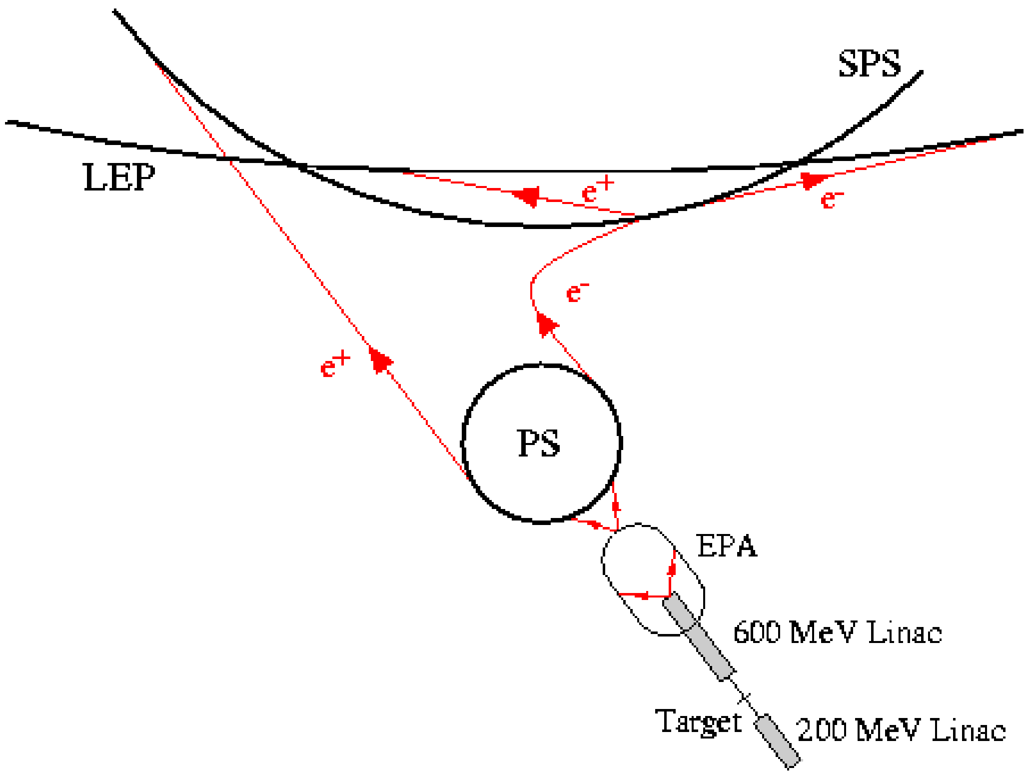

Figure 3.2: Different stages of injectors and accelerators at CERN.

The acceleration to the final collision energies at LEP proceeds through a chain of multi-purpose accelerators as shown in Figure 3.2. Electrons are generated by a high current tandem linear accelerator (Linac), and positrons are generated through bremsstrahlung (followed by pair production) by striking electrons from this 200 MeV Linac on a Tungsten target. A second Linac, known as LEP Injector Linac (LIL), is then used to accelerate both the electron and positron beams up to 600 MeV. Then the Electron Positron Accumulator (EPA) accumulates the particles of the LIL pulses into so-called bunches before passing them over to the Proton Synchrotron (PS). Real acceleration process starts with the PS, which accelerates the bunches up to 3.5 GeV. The Super Proton Synchrotron (SPS) further accelerates them up to 20 GeV and injects into the LEP main ring.

Once injected into LEP, the electron and positron beams are accelerated by radio frequency (RF) cavities installed in the straight sections and are guided around the circular arcs by dipole bending magnets. Focussing and corrections to the beams are achieved through a sophisticated system of quadrupoles, sextupoles and corrector magnets. The energy range over which the particles can be accelerated depends on the design of the collider involved. So is the case with LEP. The minimum energy is constrained by the betatron oscillation (amplitude inversely proportional to the square root of magnetic field). The maximum beam energy is limited by the RF power available to compensate the energy loss due to synchrotron radiation. For a charged particle, the synchrotron energy loss per each turn is proportional to $(\frac{\mathrm{E}^4}{m^4\rho})$, where E and m are the energy and mass of the particle and ρ is the bending radius. Thus for beam energies of 100 GeV, the maximum energy for which LEP was designed, the energy loss for each electron or positron is approximately 3 GeV per rotation.

3.2 The LEP Performance

Two fundamental parameters that characterise the performance of a particle collider are the "beam energy range" and the "luminosity". The energy clearly defines the kinematic accessibility of possible physics and the luminosity controls the possible event rate. In the following subsections, these two parameters are discussed, as realised with LEP.

3.2.1 Energy Record at LEP

In case of LEP, the beam energy range was clearly defined by the energy required to copiously produce the Z and $\mathrm{W}^{\pm}$ particles. From 1989 to 1995, the LEP-I period, e^+ and e^- beams were accelerated to energies of approximately 45 GeV, thus allowing collisions at centre-of-mass energies close to the Z mass. With a total of 17 million events recorded at the Z-peak by four LEP experiments, this period was dedicated to the extensive study of the Z-boson properties. Starting from the beginning of 1996 up to 2000, the LEP-II period as it is known, each year saw the energy moving up and up: crossing the W-pair production threshold in 1997, and reaching the milestone of 104.5 GeV energy per beam in 2000. This has provided an excellent opportunity to study the properties of W-boson and the self-interactions among the gauge bosons. In addition, it allowed increasing reach in the search of new particles, including the Higgs boson and supersymmetric (SUSY) particles. After a tumultuous last year, in which a slight excess of candidates hinted to a possible Higgs signal, the LEP machine was definitively shut down on November 2000 to pave way for the Large Hadron Collider (LHC).

3.2.2 Luminosity delivered by LEP

The luminosity for colliding beams is given by :

$$\mathcal{L} \;=\; \frac{N_e N_p n_b f_{rev}}{4\pi\sigma_x\sigma_y} \tag{3.1}$$

with $N_{e,p}$ number of e^-, e^+ per bunch, n_b number of bunches per beam, f_{rev} revolution frequency of the beams and $\sigma_{x,y}$ are the transverse beam sizes at the interaction point. The rate of interactions is directly proportional to the luminosity :

$$\frac{d\mathrm{N}}{dt} \;=\; \sigma \cdot \mathcal{L} \tag{3.2}$$

where σ is the interaction cross section. Thus for a given σ, the number of events expected for a physics process (N) increases with the integrated luminosity: $\mathcal{L}_{\mathrm{int}} = \int \mathcal{L}\,dt$.

The design peak luminosity of LEP, 1.3×10^{31} cm^{-2}sec^{-1}, was already achieved in year 1993 [3]. The target $\mathcal{L}_{\mathrm{int}}$ for LEP-II was 500 pb^{-1}, while final $\mathcal{L}_{\mathrm{int}}$ delivered by LEP was 800 pb^{-1}. A summary of the integrated luminosity collected with each experiment at LEP from 1989–2000 is given in Figure 3.3.

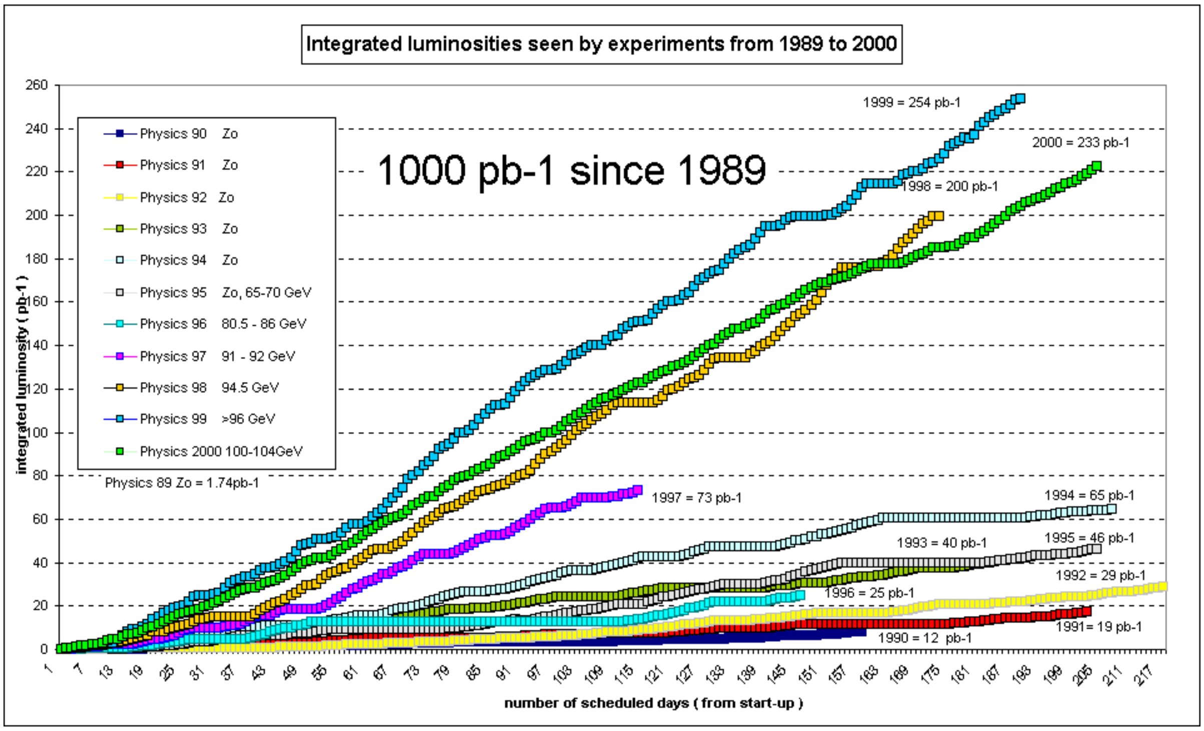

Figure 3.3: Summary of LEP luminosity from 1989–2000.

3.3 L3 Detector

Historically, most of the major discoveries in particle physics have been made with detectors specially designed to measure very precisely both the photon and lepton channels. This is, because these channels provide a clean signal with a small background contamination. To name a few, the discoveries of J/ψ [4] and Z [5] particles were possible only because of good di-lepton mass resolution of the detectors. The L3 detector was therefore

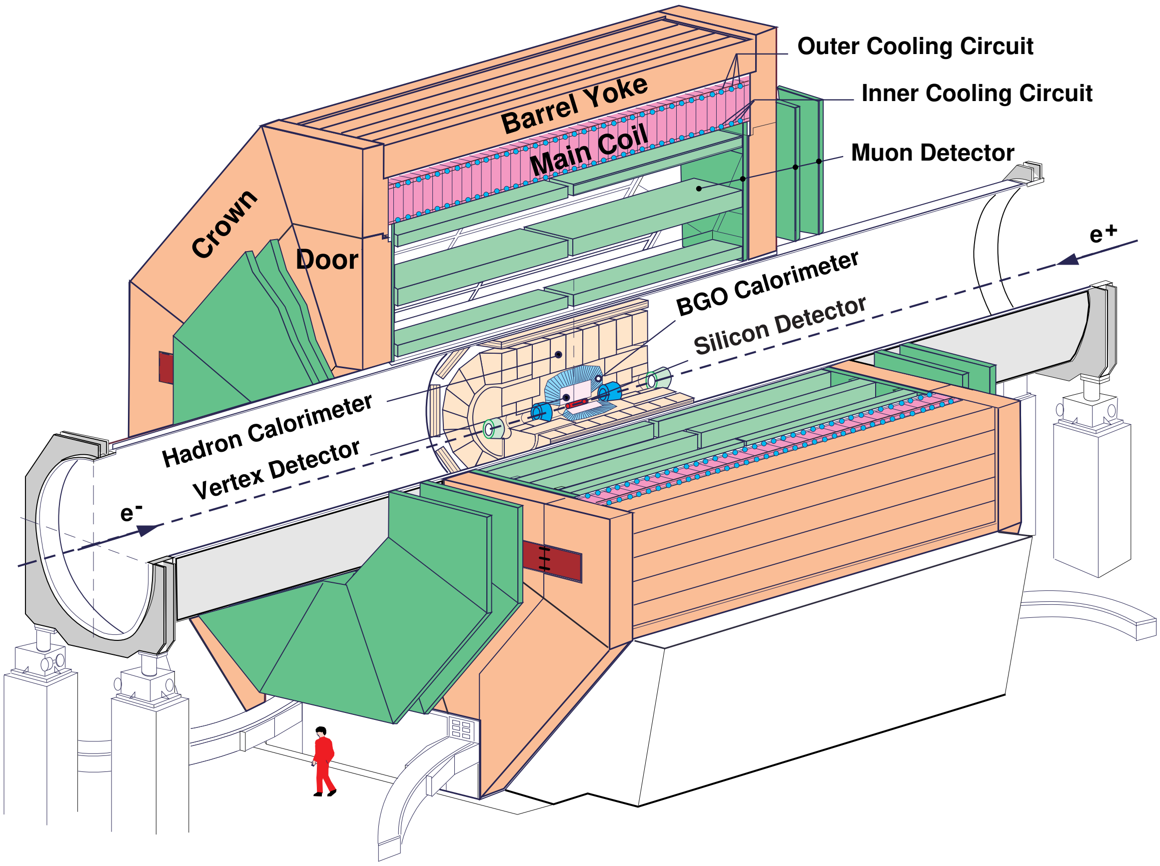

Figure 3.4: Perspective view of L3 detector.

designed with strong emphasis on high precision photon and lepton (electron and muon) measurements. Located at the second interaction point, it (Figure 3.4) was the largest of the four detectors at LEP: Aleph [6], Delphi [7], L3 [8] and Opal [9]. The operation of the detector began with the startup of LEP in 1989 and had continued until the shutdown of LEP in November 2000.

It was a hermetic detector with 99% of the total 4π solid angle coverage with length 14 m and diameter 16 m. The central tracking detector, the electromagnetic calorimeter, the scintillation counters, the hadron calorimeter, and the luminosity monitor were housed inside a 32 m long, 4.45 m diameter steel support tube (Figure 3.5), while the muon detector was mounted outside. All the sub-detectors, except a part of the muon detector, were immersed in a uniform 0.5 Tesla magnetic field along the beam direction, provided by 7.8 Kton octagonally shaped solenoidal magnet. An additional 1.5 Tesla toroidal magnetic field was added later for tracking the muon in extreme forward region. The angular coverage of the different sub-detectors are shown in Figure 3.5 in terms of the

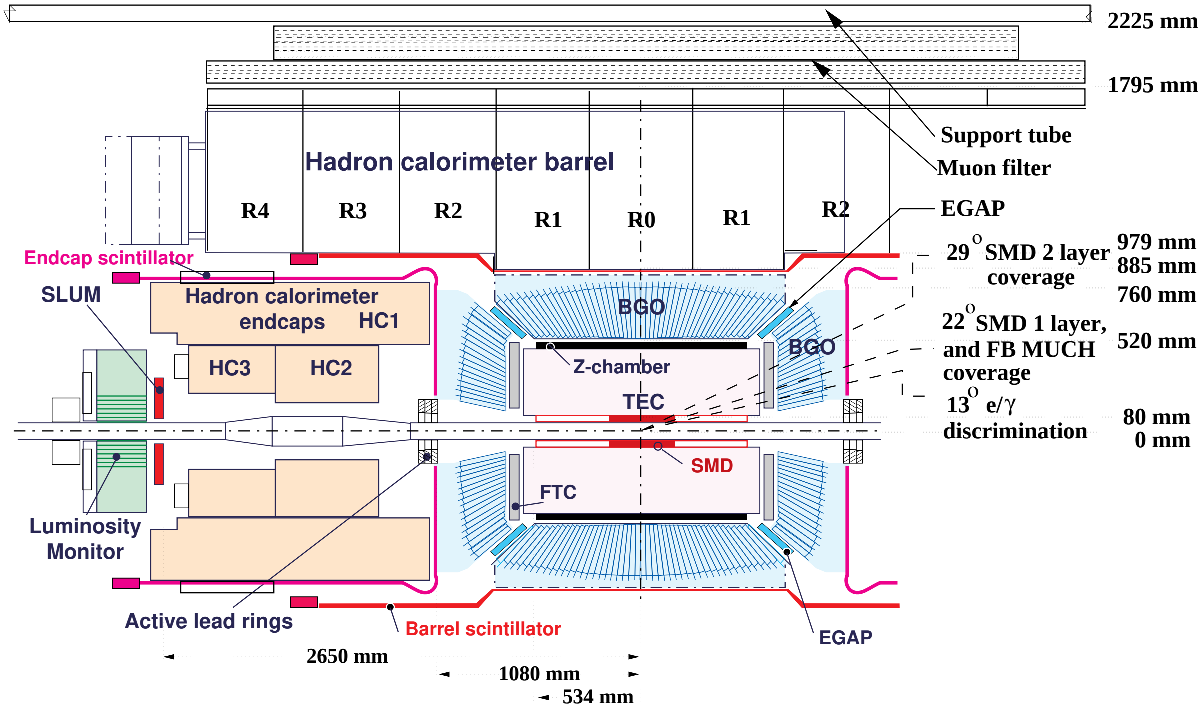

Figure 3.5: Inner components of the L3 detector housed inside the support tube.

polar angle. The individual sub-detectors are described in the following sub-sections with particular emphasis on those most important for this analysis.

3.4 Tracking

In the homogeneous magnetic field of L3, a charged particle follows a helical path. Due to the solenoidal nature of the magnetic field, this helix can be seen as a circle in the xy plane and a straight line in the sz plane (s represents the arc length in the xy plane or sagitta). The circle is parametrised in terms of its curvature, its distance of closest approach (DCA) with respect to a reference point and the azimuthal angle at the point of closest approach. From these quantities, the transverse momentum, p_T, of the track and sign of the charge of the particle can be inferred. The polar angle of the track is, however, determined from the measured z coordinate of the track. In L3, full track reconstruction and measurement of the track parameters is achieved by simultaneous measurement of the track coordinate along its trajectory, mainly by three sub-detectors;

- Silicon Microvertex Detector (SMD),

- Time Expansion Chamber (TEC), and
- Z Chamber.

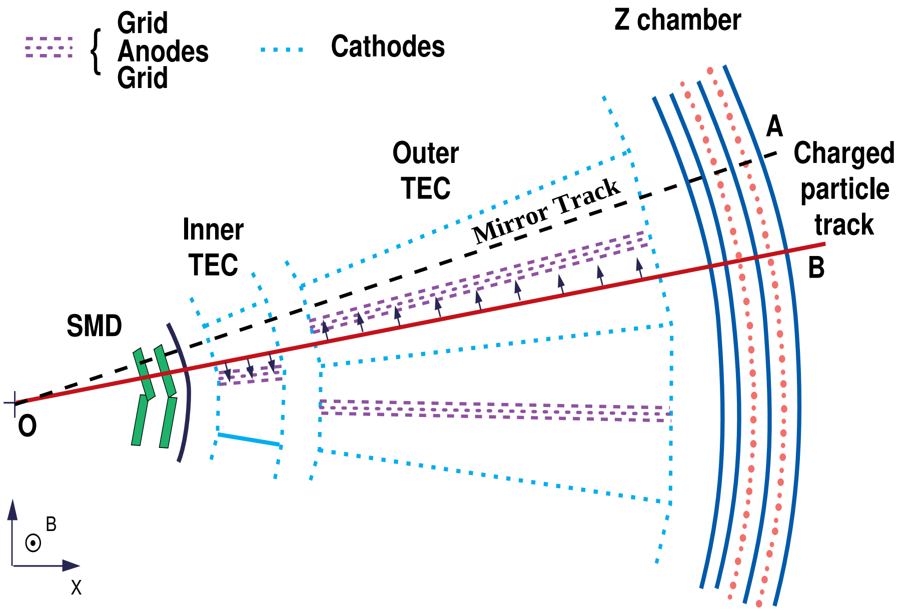

Figure 3.6: The tracking sub-detectors of the L3 experiment. A charged particle produced during an e^+e^- interaction will first cross the SMD, then the TEC and, finally the Z-Chamber before hitting the calorimetry.

The position resolution varies from 320 μm in the Z-Chamber, to 50 μm in the TEC, to 10 μm in the SMD. This clearly follows the progressive importance of extrapolating the measured track back to the interaction vertex. In the following, all the tracking sub-detectors are explained.

3.4.1 Silicon Microvertex Detector

The Silicon Microvertex Detector [10], the innermost sub-detector, was made up of two radial layers of Silicon micro-strips positioned at 6 cm and 8 cm from the beam pipe. The main aim was here, to measure very precisely the track parameters in order to pinpoint the impact parameter, used for efficient b-tagging. It provides good measurement of the $r\phi$ and rz coordinates for a polar angle range of $21.5° - 158.5°$ ($\approx 90\%$ angular coverage). Its high resolution also improves the transverse momentum resolution by approximately a factor of $\left(\frac{2}{3}\right)$ as compared to the TEC alone (see Figure 3.8(b)).

Each SMD layer has 12 modules which in turn has 4 sensors of dimensions $70\,\text{mm} \times 40\,\text{mm} \times 300\,\mu\text{m}$. On its junction side, each sensor strip measures the $r\phi$ coordinate, while the ohmic side has strips perpendicular to those of the junction side, in order to measure rz coordinates. An ionising particle passing through the Silicon sensor will produce electron-hole pairs. By applying a voltage bias between two sides of the sensor, electrons and holes

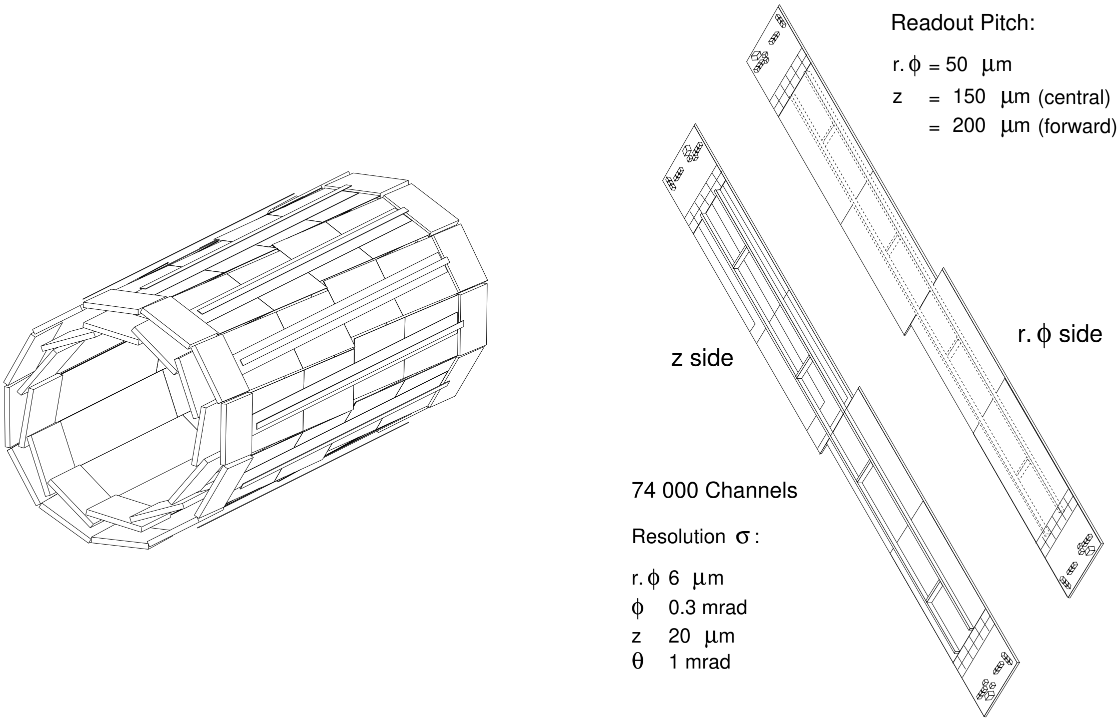

Figure 3.7: Perspective view of the Silicon microvertex detector and one of the ladders.

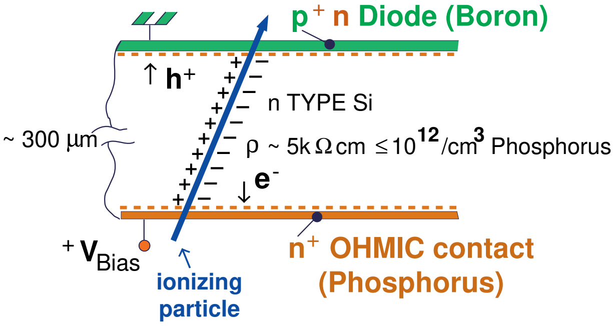

(a) Principle of detection of the SMD.

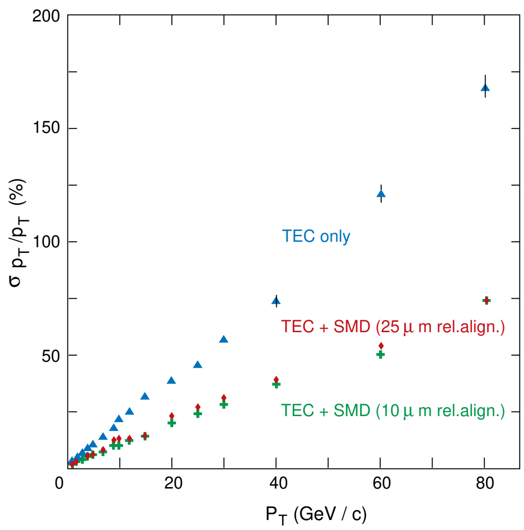

(b) Improved p_T resolution due to SMD.

Figure 3.8: Principle of operation of the SMD and improvement achieved in p_T resolution after including the SMD.

will drift to the nearest strips on both surfaces, allowing simultaneous measurement of $r\phi$ and rz coordinates (Figure 3.8(a)). The corresponding pitch and resolution are:

	Readout Pitch	Resolution[1]
Junction side ($r\phi$)	50 μm	10 μm
Ohmic side (z) (central)	150 μm	$(21 \oplus 15 \cdot \tan\lambda)$ μm
Ohmic side (z) (forward)	200 μm	$(21 \oplus 26 \cdot \tan\lambda)$ μm

3.4.2 Time Expansion Chamber

The Time Expansion Chamber [11] measures the time of arrival of the ionisation electrons at the anode wires, relative to a marker reference, to reconstruct the curvature of a charged track bending in the magnetic field. Slow drift velocity in a low diffusion gas in the drift region, followed by fast absorption by strong fields generated by focus wire near the anode characterise its *modus operandi* (see Figure 3.9).

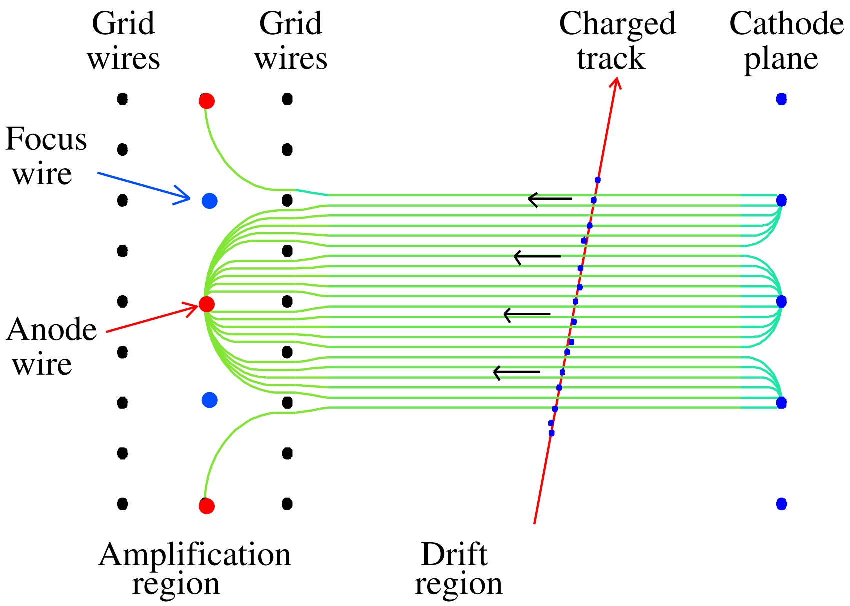

Figure 3.9: Principle of the Time Expansion Chamber.

The fiducial volume occupied by the TEC is: 8.5 cm $< r <$ 47 cm, 63 cm $< |z|$, and it comprises of 12 inner sectors with 8 anodes, and 24 outer sectors with 54 anodes. The gas mixture used is: 80% CO_2 + 20% iso-C_4H_{10} at pressure 2 bar with low diffusion coefficient, and low drift velocity ≈ 6 μm/ns. Measurement of the distance of the track from the anode plane is read out using Flash ADC with a centre-of-gravity method giving better spatial resolution.

The single track resolution is 50 μm, and the double track resolution is 450 μm. Ambiguity due to mirror tracks is resolved by matching the hits with the inner and outer TEC

[1] $\tan\lambda$ is the slope in the sz plane and is a constant for a given track.

(Figure 3.6). The transverse momentum resolution of the TEC combined with SMD is: $\sigma(1/p_T) = 0.012\ \mathrm{GeV}^{-1}$. It is also found that the calorimetric energy resolution of 11% improves to 8% after inclusion of charged track informations, as shown in Figure 3.10(b).

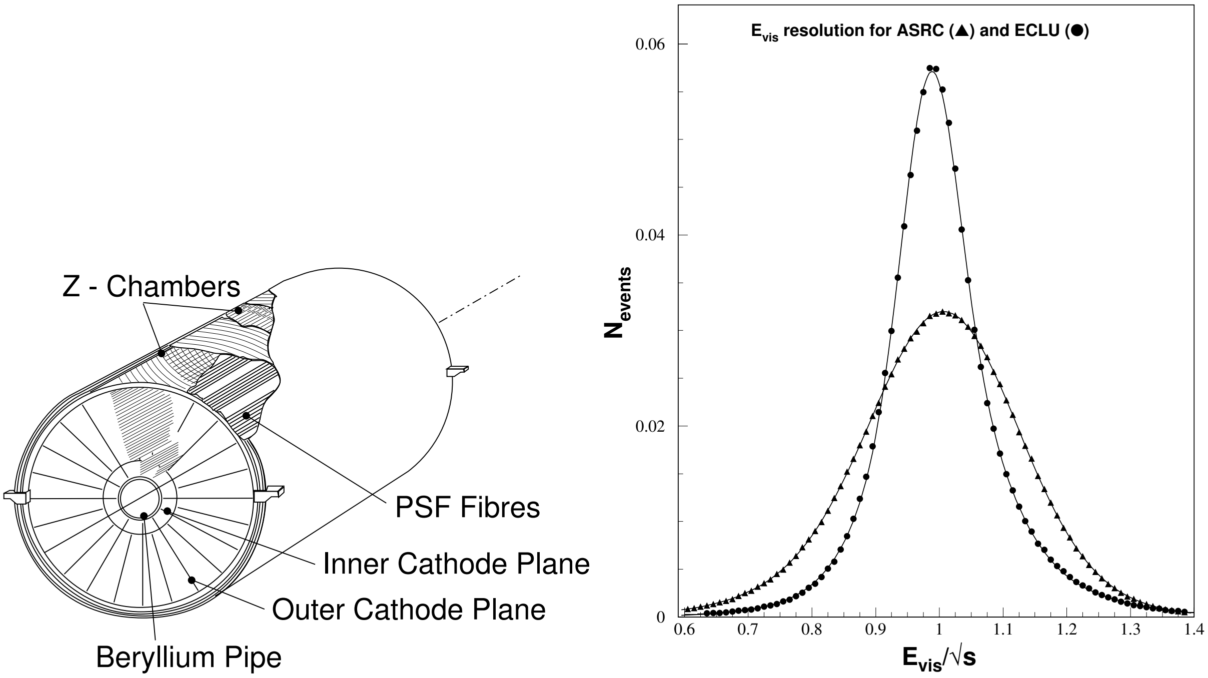

Figure 3.10: (a) A perspective view of the central track detector, and (b) Plot showing improvement in the calorimetric energy resolution including charged track information.

3.4.3 Z Chambers

Two layers of Z chambers [12] surrounding the TEC, at radial distances between 48 cm and 49 cm and having $|z|$-extent < 51 cm (Figure 3.10(a)), provide accurate measurements of z-coordinates of points along the trajectory of a charged particle. These chambers are proportional wire chambers with thickness 21.5 mm. The wire chambers operate in drift mode, with gas mixture of 80% Ar + 20% CO_2. Ionisation signals are read out by cathode strips, inclined with respect to the beam axis by $0°, 90°, \pm 69°$. This gives a z-coordinate resolution of 320 μm and double track resolution of 7 mm.

3.5 Calorimetry

Conceptually, calorimeter is a block of matter that interacts with an incident particle in such a way that all the energy of the particle gets absorbed in it. The energy deposition occurs in the form of particle cascades of ever degrading energies. Most of the energy is eventually dissipated in the form of heat, while a small but constant fraction of it gives a detectable signal *e.g.* scintillation light or ionisation pulse. Inferring this signal, one measures the energy and position of the incident particle.

3.5.1 Electromagnetic Calorimeter

The Electromagnetic Calorimeter (ECAL) [14] (Figure 3.11), made up of homogeneous Bismuth Germanium Oxide (BGO) crystals, measures total energy of electrons, positrons and photons accurately and serves as the first interaction length for measurements of hadrons along with the hadron calorimeter.

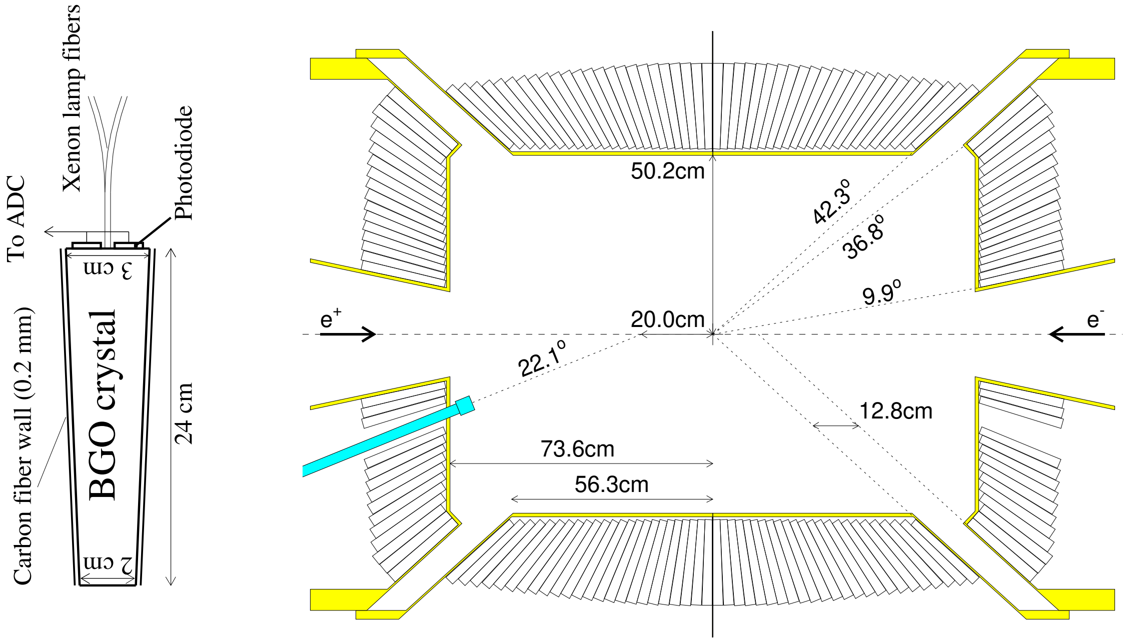

(a) A barrel BGO crystal. (b) Longitudinal view of BGO detector.

Figure 3.11: BGO crystal and L3 electromagnetic calorimeter.

The front face of a BGO crystal in the barrel is 2 cm × 2 cm, the back is 3 cm × 3 cm and has a length of 24 cm ($\approx$ 22 X_0). The material specifications of the BGO crystal are:

Density(ρ)	7.13 gm/cc
Radiation length(X_0)	1.12 cm
Moliere radius(R_M)	2.4 cm
Peak emission λ	480 nm
Decay time of light	300 ns
Temperature coefficient	$-1.55\%/^\circ$C
Nuclear interaction length(λ_I)	22 cm

There are 7680 crystals in the barrel and 3054 in the endcap, the temperature is monitored for 1 in 12 crystals. The material before ECAL barrel is 0.3 – 0.4 X_0 and bit larger in

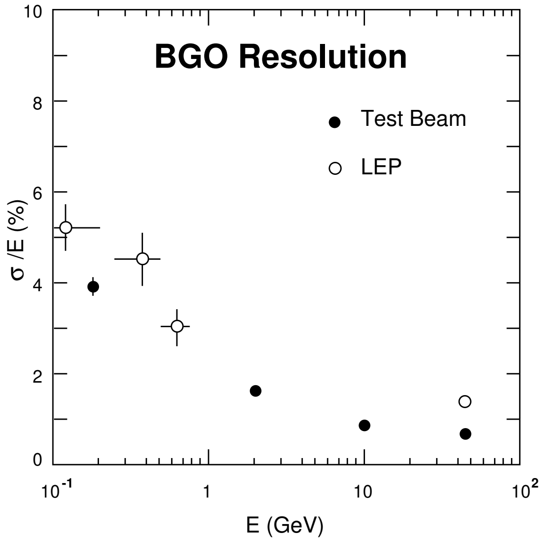

(a) Energy resolution of BGO calorimeter.

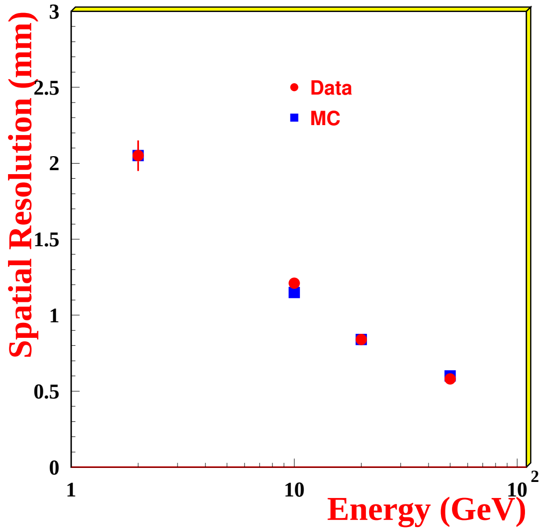

(b) Position resolution of BGO calorimeter.

Figure 3.12: Energy and position resolution of the BGO calorimeter.

case of endcap. Each crystal is read out by 2 photo-diodes, with a quantum efficiency of 70%. The BGO calorimeter was calibrated in test beams using electrons of energies 0.18, 2, 10 and 50 GeV. The energy resolution obtained is $\approx 5\%$ at 180 MeV, less than 2% above 2 GeV and about 1.2% at 45 GeV as shown in Figure 3.12(a). The linearity is better than 1%. The position resolution is determined by the centre-of-gravity method to be $\sim$ 2 mm (see Figure 3.12(b)) whereas the angular resolution is $\sim$ 1 mrad for electromagnetic showers at energy $>$ 2 GeV. The hadron/electron rejection ratio $\sim$ 1000 :1.

3.5.2 Gap Calorimeter

During the 1995/96 shutdown period, lead-scintillating fibre calorimeter (EGAP) [15] was installed in the gap between ECAL barrel and endcap, to make the calorimeter more hermetic. Each gap is filled up with 24 modules of trapezoidal blocks. They are placed side by side to fit the gap as shown in Figure 3.13. The gap between the modules is tilted by about 25 mrad with respect to the interaction vertex to avoid loss of particles in the cracks.

The ratio in volume between the lead and the fibres is 4 :1, giving X_0 = 0.72 cm, in order to ensure sufficient shower containment. The total thickness corresponds to 21 X_0. From the test beam study one obtains the energy resolution as :

$$\frac{\sigma(\mathrm{E})}{\mathrm{E}} = \left(2.3 + \frac{11.6}{\sqrt{\mathrm{E(GeV)}}}\right) \%$$

Angular resolution for EGAP is decided by the front size of the trapezoidal block, and is about 130 mrad.

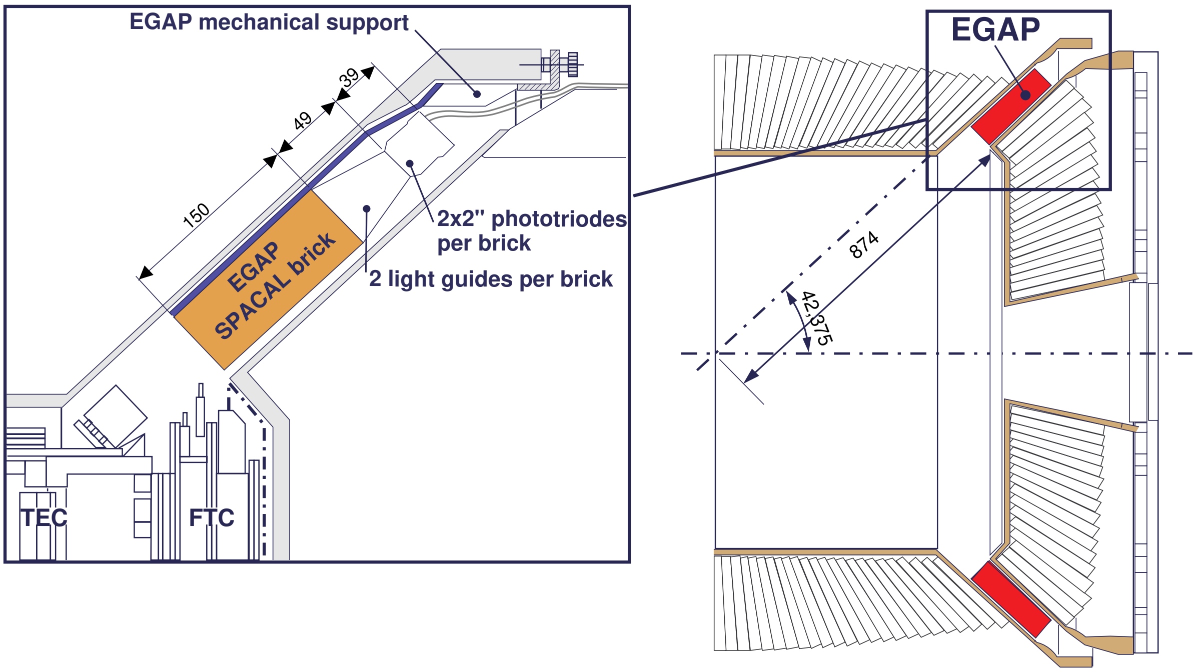

Figure 3.13: Lead-scintillating fibre calorimeter (EGAP).

3.5.3 Hadron Calorimeter

The Hadron Calorimeter (HCAL) [16] is a fine sampling calorimeter consisting of layers of uranium ($\lambda_I \sim 11$ cm) plates (5–10 mm) and brass tube proportional chambers (5.6 mm). The gas used is 80% Ar + 20% CO_2. The uranium plate acts as an absorber, while the proportional chamber enables us to record the charged particle along its path. The shower profile in the calorimeter is used to measure the energy of the impinging particle that initiates the shower.

The HCAL has a length of 472.5 cm, inner radius of 88.5–97.9 cm, and outer radius of 179.5 cm, with angular coverage ($35^\circ < \theta < 145^\circ$) for the barrel part and ($5.5^\circ < \theta, 180^\circ - \theta < 35^\circ$) for the endcap region. The barrel consists of 16 modules in ϕ and 9 modules in z, while the endcap consists of 6 modules made of 3 rings: HC1, HC2 and HC3. Corresponding to the barrel/endcap parts, there are 7968/2284 chambers. These chambers are grouped into towers with $\Delta\phi \approx 2.5^\circ$, $\Delta z \approx 6$ cm, and $\Delta r \approx 8$ cm.

The energy resolution of HCAL is $(\frac{\sigma_E}{E}) = (\frac{55}{\sqrt{E}} + 5)\%$, and the angular resolution is 2.5°. Material transversed by a particle inside the HCAL in conjunction with ECAL is $6 - 7\ \lambda_I$ depending upon the angle of incidence. Muon Filter [17] adds 1.03 absorption length to it. It comprises of 8 octants, 139 cm long. Each octant is made of 6 layers of 1 cm thick brass absorbers, interleaved with 5 layers of proportional tubes.

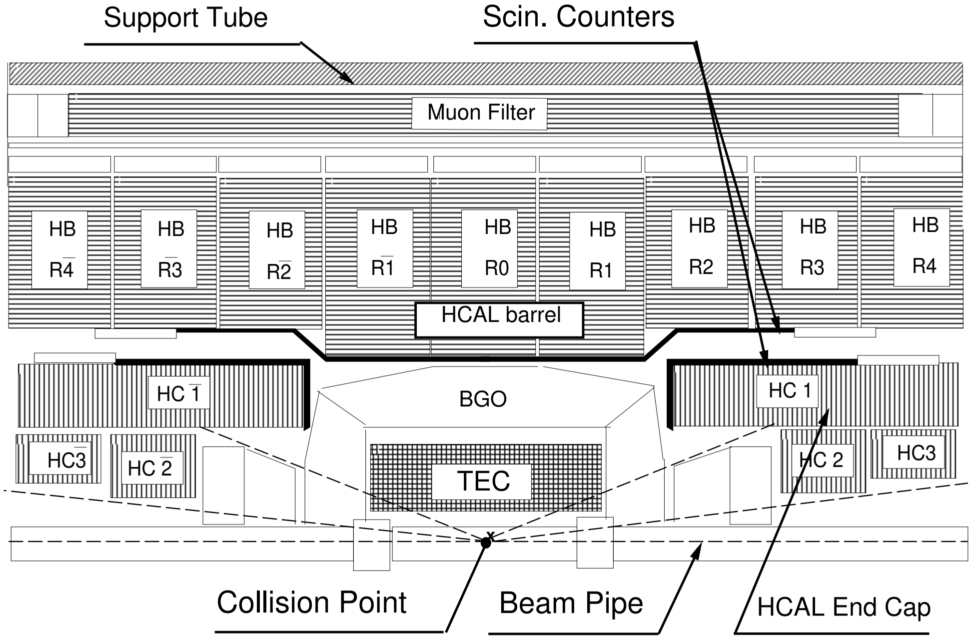

Figure 3.14: r-ϕ view of hadron calorimeter.

3.6 Muon Detection

One of the principal goals of L3 experiment is to identify and to measure the momentum of high energy muon. This is achieved by combining informations from all the sub-detectors. In the TEC the muon results in a track segment, in the BGO and hadron calorimeters in a position and energy loss measurement, and in the outer muon spectrometer in three accurate track segments. Measurement in the muon chamber provides the most vital information for selecting muons, and is the subject of next subsection.

3.6.1 Muon Chambers

The Muon Chamber (MUCH) [18] system, made with drift chambers, consists of a barrel part and forward-backward part. The barrel part comprises of 2 sets of 8 octants. Each octant has 5 precision (P) chambers: 2 Outer (MO), 2 Middle (MM) and 1 Inner (MI), and 6 Z-chambers: top and bottom covers of MI and MO (see Figure 3.15). The gas mixture and drift velocity (v_d) in the chambers are listed below:

Chambers	Gas	$v_d\,(\mu m/ns)$
P	38.5% ethane, 61.5% Ar	50
Z	8.5% ethane, 91.5% Ar	30

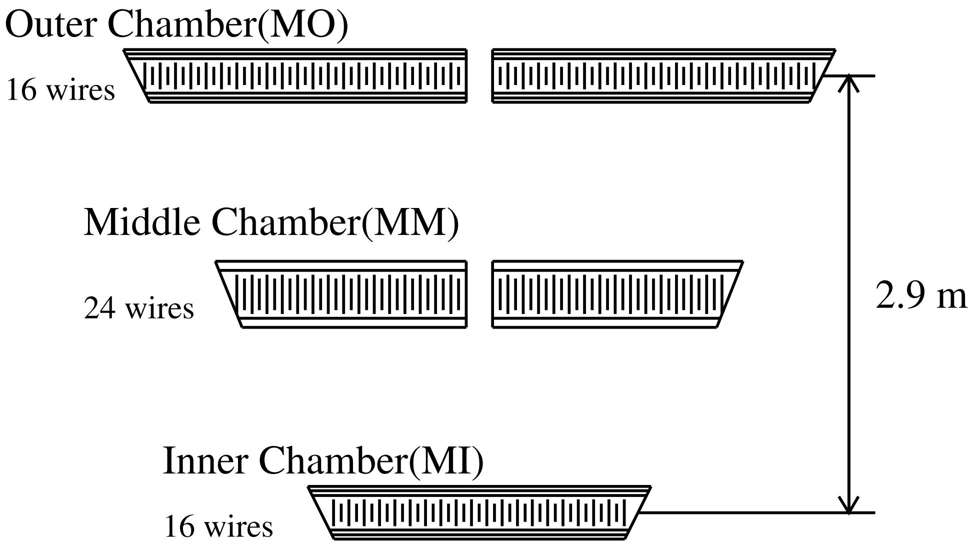

Figure 3.15: An octant of the muon chamber.

The principal measurement of the MUCH is measurement of the sagitta of a track bending under the magnetic field. In terms of the coordinate measurement in the different P segments, the sagitta is given by s = $(X_{MI} + X_{MO})/2 - X_{MM}$, each measurement having an uncertainty of $\varepsilon_i = 200\ \mu\mathrm{m}/\sqrt{N_i}$ ($i = \#$ wires in MI, MM, MO). This propagates into the intrinsic error on the sagitta measurement as: $\Delta s = \sqrt{(\varepsilon_{MI}/2)^2 + (\varepsilon_{MO}/2)^2 + (\varepsilon_{MM})^2}$.

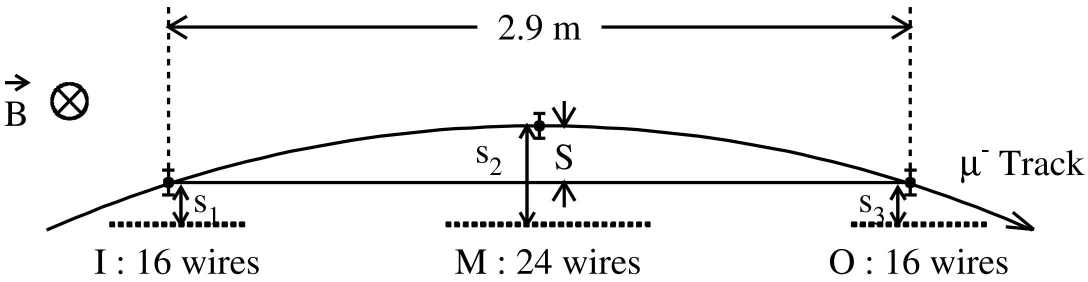

Figure 3.16: Sagitta measurement of a typical muon track.

The total error on the sagitta measurement is given by:

$$\begin{aligned} \Delta s &= (\text{intrinsic}) \oplus (\text{mult. scat.}) \oplus (\text{align syst.}) \\ &= 57\ \mu\mathrm{m} \oplus 35\ \mu\mathrm{m}(\text{at } 45\ \text{GeV}) \oplus 30\ \mu\mathrm{m} \quad \sim\ 73\ \mu\mathrm{m} \end{aligned}$$

This gives us momentum resolution of $(\frac{\Delta p}{p}) = (\frac{\Delta s}{s}) = 2.5\%$, and a corresponding di-muon mass resolution of $(\frac{\Delta m}{m}) = 1.8\%$. The precision of Z-chambers is $\simeq$ 500 μm, which translates to angular resolution of 0.3°. The angular coverage of the barrel muon chamber in terms of the polar angle is given by; $\theta, 180^\circ - \theta < 44^\circ$(MO), 35°(MM), 24°(MI).

The forward backward muon chambers (FBMU) [19] are mounted on the magnet doors (Figure 3.17), measuring the bending of muons in solenoidal (S-region) and toroidal (T-region) of the magnetic field. On either side of the interaction point, there are three layers of FBMU: Inner (FI), Middle (FM), and Outer (FO), each containing 16 drift chambers. The gas mixture used is 86% argon, 10% CO_2 and 4% isobutane.

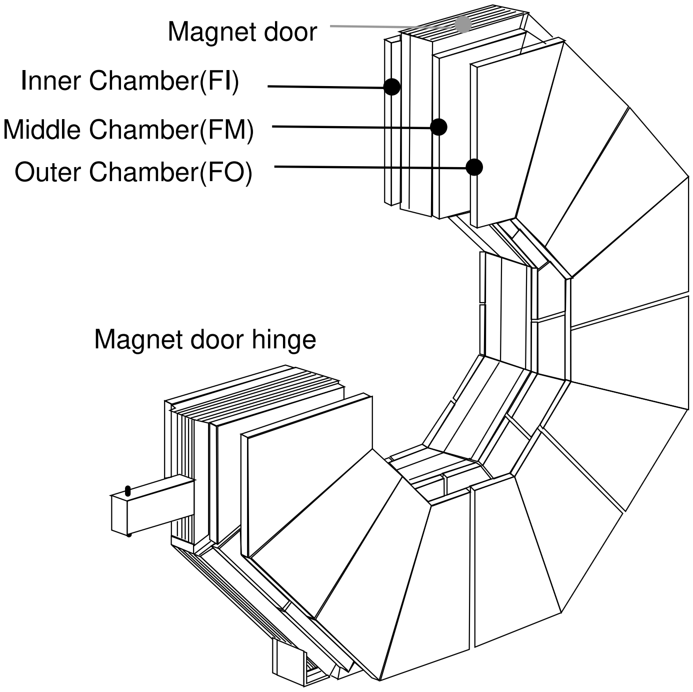

Figure 3.17: Forward backward muon chamber.

The momentum resolution worsens in the FBMU due to multiple scattering in the 1 m thick magnet doors. It deteriorates steadily (in the S-region) to a saturating 30% (in the T-region) at smaller angles, as shown Figure 3.18.

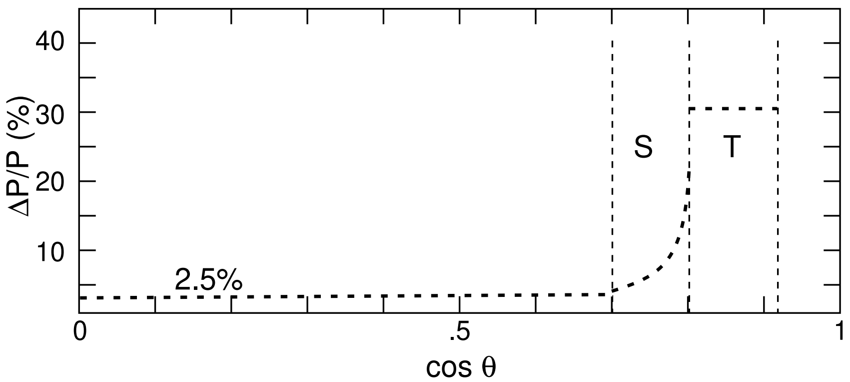

Figure 3.18: Momentum resolution for a 50 GeV muon as a function of the polar angle.

3.6.2 Scintillation Counters

The excellent time resolution of plastic scintillators is used in the scintillation counters to measure the time of flight of particles passing through the detector with respect to the beam crossing time. These are primarily used to distinguish genuine dimuon events (zero time difference between opposite counters) from cosmic muon events (time difference $\approx$ 5.8 ns). The scintillator hit multiplicity also helps on improving the trigger rate.

The barrel part consists of 30 plastic scintillation paddles of length 2.9 m and thickness 10 mm. Both ends of the paddles are connected by light-guides to the photomultipliers. In the rz plane, the counters mark the boundary between the electromagnetic and hadron calorimeter and are at a radial distance of 886 mm for $|z| < 800$ mm and 979 mm for 800 mm $< |z| <$ 1000 mm from the beam axis (see Figure 3.5). Polar angle coverage of the barrel counters is $34° < \theta < 146°$.

The endcap scintillation counter system [20] consists of 16 counters located between the electromagnetic and hadron calorimeter endcaps on either side of the interaction point. Counters are made out of 3 plates of 5 mm thick plastic scintillator. Light from each plate is collected by 10 wave-length shifting (WLS) fibres of diameter 1 mm glued into grooves of 1.5 mm $\times$ 1.5 mm. 30 fibres per counter-end are connected into an optical connector at the outer edge of the counters. A flexible guide of 30 fibres, each 1.7 m long, connects the counters to the photo tubes which are situated outside the hadron barrel. The counters having an inner (outer) radius of 230 mm (746 mm), are attached to the shielding of the BGO endcaps. The centre of the second scintillator plate is located at a distance of z = $\pm$ 1132.5 mm from the nominal interaction point, giving a polar angle coverage of $11.5° < \theta < 34.1°$. A time resolution of 0.46 ns has been achieved from the dimuon events in the barrel (see Figure 3.19 [13]), and 1.9 ns in the endcap. The efficiency of the scintillator hit for the dimuon events is larger than 99%.

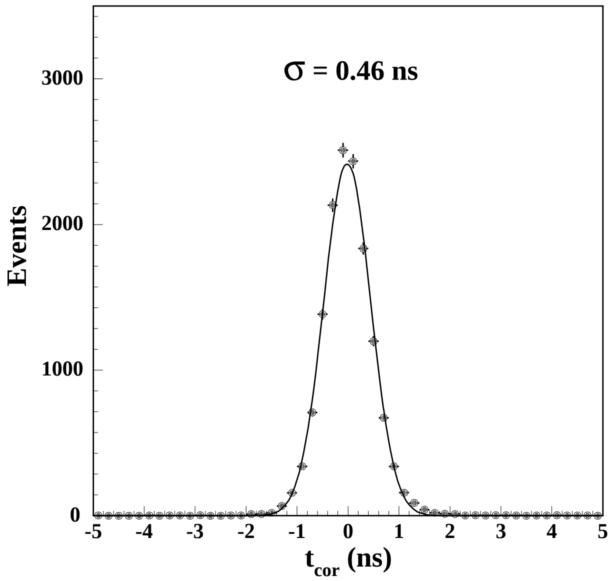

Figure 3.19: Timing resolution of the barrel scintillation counters.

3.7 Luminosity Measurement

In an electron positron collider like LEP, one usually determines the integrated luminosity ($\mathcal{L}_{\rm int}$) from the measured number of *low* angle Bhabha scattering events, $e^+e^- \to e^+e^-(\gamma)$. For low scattering angles the reaction is dominated by t-channel photon exchange diagram (Figure 3.20). The advantage with this process is that it is largely independent of Z parameters and theoretically well understood leading to small error on $\mathcal{L}_{\text{int}}$.

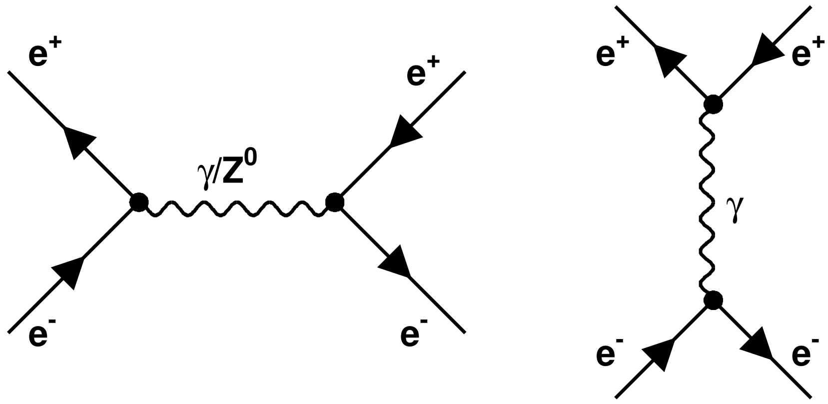

Figure 3.20: Diagrams of Bhabha scattering in the (a) s-channel and (b) t-channel.

In L3, the luminosity is measured by what is known as luminosity monitor [21]. It consists of two mirror symmetric halves (forward and backward) with respect to the beam axis. Each half-detector has two parts:

- A BGO crystal array of 304 crystals. These crystals are mounted in a cylindrical symmetry around the beam axis. The angular coverage is $31\,\text{mrad} < \theta < 62\,\text{mrad}$.
- A Silicon strip detector (SLUM) with good position resolution mounted in front of the BGO crystals. The purpose of this sub-detector is to measure precisely the geometrical acceptance of the BGO crystals. Knowledge of this geometry is very important in order to translate the observed Bhabha event rate into a luminosity measurement ($\sigma \propto \frac{1}{\theta^2}$).

The luminosity monitor is positioned at a distance of 2.65 m from the interaction point. The distance chosen is a compromise, it is (a) sufficiently far away from the interaction point in order to measure events at very low θ, and (b) sufficiently close to the origin for the systematic effect due to event selection not to dominate in the final measurement error. With the combination of BGO crystals and SLUM, the absolute luminosity has been measured with a precision of about 0.05% at the Z peak and $\sim$ 0.6% at high energy run.

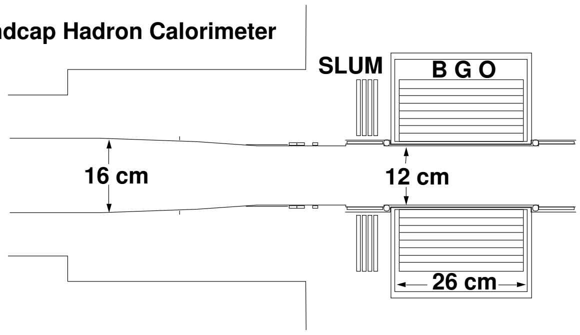

Figure 3.21: One side view of the luminosity monitor showing the position of SLUM and BGO crystals.

3.8 Trigger and Data-Acquisition

No matter how relevant the information might be coming from the detector, the complete readout sequence of an event takes about 500 μs (equivalent to 23 times of the beam crossing time). During this time period, no new event can be processed. Therefore, a multi-level trigger system is implemented to reduce this inherent dead time by allowing abortion of the readout sequence, if a piece of information is found to be faulty. This enables a new readout sequence to be started sooner for recording of a new event.

The trigger system proceeds as follows. At first, it has to decide, from the signals obtained from a detector component, if these signals are compatible with an e^+e^- interaction. Then, if the signal is relevant to an e^+e^- collision, it decides, depending on the quality of the response of the various subdetectors, to allow or veto the storage on tape of these signals as an event. The L3 trigger system is realised in three levels which are explained in following subsections. The difference between these levels is the complexity of the operations involved and the time needed to perform the calculations. This way, a lower-level trigger remains in a position to abort a readout sequence, before it is passed over to higher-level trigger that performs more time consuming operations.

Level-1 Trigger

The level-1 trigger [22] is a fast trigger based on the hardware response of various subdetectors. That's why it is alternatively known as "hardware trigger". The role of level-1 trigger is to initiate the readout sequence if an e^+e^- collision is detected and to perform simple tests on an event in order to decide to keep it or not for further processing. Its decision time is about 20 μs, and at this level the event rate is reduced from 45 kHz bunch crossing rate to about 20 Hz.

It consists of five independent sub-triggers; the energy trigger, the TEC trigger, the muon trigger, the scintillator trigger, and the luminosity trigger. In order to pass the level-1 trigger, an event has to be selected by at least one of the five sub-triggers. The energy trigger requires either

- a total energy of at least 25 GeV in the electromagnetic and hadron calorimeters, or
- a minimum energy of 15 GeV in the barrel region ($42° < \theta < 138°$) of calorimeters, or
- a minimum energy of 8 GeV in the barrel of the electromagnetic calorimeter alone.

The TEC trigger requires at least two tracks identified with a transverse momentum greater than 150 MeV and with a maximum acollinearity of 60°. The requirement in the scintillation counter trigger is a coincidence of at least 5 hits, in the counters during a 30 ns interval about the beam crossing time, which must extend over an azimuthal angular region of at least 90°. The muon trigger selects events with at least one particle which passes through the muon chambers with minimum transverse momentum of 1 GeV measured either in 2 out of 3 of the P-chambers, or in 3 out of 4 of the Z-chambers. All these quantities like track momenta *etc.* are approximated by comparing the raw signals with the lookup tables.

A positive decision from any of the individual level-1 triggers, initiates the detector data to be digitised and stored in multi-event buffers which takes around 500 μs, thereby causing the dead time for the data acquisition. However, in case of negative decision, this level does not produce any dead time.

Level-2 Trigger

The level-2 trigger [23] works in parallel to the level-1 trigger and has access almost to the same information as latter. However, it has more time to make a decision. Only events which were selected by only one of the level-1 sub-triggers are considered by level-2 (events with two level-1 sub-triggers are all accepted by level-2). It uses the coarse digitised data from various sub-detectors, and additional informations from combined energy clusters in the calorimeters, loosely reconstructed tracks and the interaction point. It spends about 8 ms on an event without inducing any dead time. It has a rejection power of 20 to 30% averaged over all first level triggers, and either passes all event information to an event builder memory or resets the event builder memories.

Level-3 Trigger

The principle of the level-3 trigger [24] (which is allowed ten times as much the time available to the previous levels) is similar to that of the second one, but accesses fully digitised data and bases its decision on recalculated and calibrated energies, fully reconstructed tracks and vertices which matched calorimetric clusters. On a positive third level trigger the data is transferred to the data acquisition system which is subsequently written to tapes at the rate of about 2-3 Hz.

Data Acquisition

The L3 Data Acquisition (DAQ) system [25] performs three basic tasks. It reads out the digitised data from the detector, storing the result for subsequent analysis. The data are also used to monitor the detector performance online. The average L3 DAQ efficiency is defined as the ratio of integrated luminosity, $\mathcal{L}_{\text{int}}$, recorded by the DAQ system to the $\mathcal{L}_{\text{int}}$ delivered by LEP, and it is about 92% as shown in the following table for last two years of data taking.

Year	$\mathcal{L}_{\text{int}}$ delivered	$\mathcal{L}_{\text{int}}$ recorded
1999	254 pb^{-1}	233 pb^{-1}
2000	233 pb^{-1}	217 pb^{-1}

Source of inefficiency is almost evenly distributed among different causes: problem with detector readout, fastbus, hardware and software problem, trigger hang-up *etc.*.

References

[1] LEP Design report CERN-LEP/84-01 (1984), Vol II;
H. Schopper, Phil. Trans. R. Soc. Lond. **A336** (1991) 179;
S. Meyers and E. Picasso, Contemp. Phys. **31** (1990) 387.

[2] Ian Wilson and Heino Henke, "The LEP Main Ring Accelerating Structure", CERN Yellow Report 89-09;
Particle Data Group, C. Caso *et al.*, Eur. Phys. J. **C3** (1998) 1.

[3] G. Arduini *et al.*, *LEP Operations, 1989-1995*, **CERN-SL/96-043**.

[4] J.J. Aubert *et al.*, Phys. Rev. Lett. **33** (1974) 1404;
J.E. Augustin *et al.*, Phys. Rev. Lett. **33** (1974) 1406.

[5] UA1 Collab., G. Arnison *et al.*, Phys. Lett. **B126** (1983) 398;
UA2 Collab., P. Bagnaia *et al.*, Phys. Lett. **B129** (1983) 130.

[6] ALEPH Collab., D. Decamp *et al.*, Nucl. Inst. Meth. **A294** (1990) 121.

[7] DELPHI Collab., P.A. Aarnio *et al.*, Nucl. Inst. Meth. **A303** (1991) 233.

[8] L3 Collab., B. Adeva *et al.*, Nucl. Inst. Meth. **A289** (1990) 35.

[9] OPAL Collab., K. Ahmet *et al.*, Nucl. Inst. Meth. **A305** (1991) 275.

[10] B. Alpat *et al.*, Nucl. Inst. Meth. **A315** (1992) 197;
M. Acciarri *et al.*, Nucl. Inst. Meth. **A351** (1994) 300;
M. Acciarri *et al.*, Nucl. Inst. Meth. **A360** (1995) 103.

[11] A.H. Walenta, IEEE Trans. Nucl. Sci. **26** (1979) 73;
H. Akbari *et al.*, Nucl. Inst. Meth. **A315** (1992) 161;
F. Beissel *et al.*, Nucl. Inst. Meth. **A332** (1993) 33.

[12] A. Breskin *et al.*, Nucl. Inst. Meth. **143** (1977) 29;
J. Chiba *et al.*, Nucl. Inst. Meth. **206** (1983) 451;
K. Deiters *et al.*, Nucl. Inst. Meth. **A323** (1992) 162.

[13] L3 Collab., O. Adriani *et al.*, Phys. Rep. **236** (1993) 1.

[14] J.A. Bakken *et al.*, Nucl. Inst. Meth. **228** (1985) 294;
J.A. Bakken *et al.*, Nucl. Inst. Meth. **254** (1987) 535;
J.A. Bakken *et al.*, Nucl. Inst. Meth. **275** (1989) 81.

[15] G. Basti *et al.*, Nucl. Inst. Meth. **A374** (1996) 293.

[16] L3 Collab., A. Arefiev *et al.*, Nucl. Inst. Meth. **A275** (1989) 71;
L3 Collab., A. Arefiev *et al.*, Nucl. Inst. Meth. **A285** (1989) 403;
L3 Collab., O. Adriani *et al.*, Nucl. Inst. Meth. **A302** (1991) 53.

[17] R. D'Alessandro, Nucl. Inst. Meth. **A289** (1990) 103;
L3 Collab., O. Adriani *et al.*, Nucl. Inst. Meth. **A300** (1991) 493.

[18] L3 Collab., G. Chiefari *et al.*, Nucl. Inst. Meth. **A277** (1989) 187;
L3 Collab., B. Adeva *et al.*, Nucl. Inst. Meth. **A323** (1992) 109.

[19] L3 Collab., A. Adam *et al.*, Nucl. Inst. Meth. **A383** (1996) 342.

[20] Ulrich Uwer, L3 Internal Note # 2003 (1996).

[21] I.C. Brock *et al.*, Nucl. Inst. Meth. **A381** (1996) 236.

[22] L3 Collab., R. Bizzari *et al.*, Nucl. Inst. Meth. **A283** (1989) 799;
L3 Collab., P. Bagnaia *et al.*, Nucl. Inst. Meth. **A324** (1993) 101;
L3 Collab., P. Bagnaia *et al.*, Nucl. Inst. Meth. **A344** (1994) 212.

[23] L3 Collab., Y. Bertsch *et al.*, Nucl. Inst. Meth. **A340** (1994) 309;
L3 Collab., S.P. Beingessner *et al.*, Nucl. Inst. Meth. **A340** (1994) 322.

[24] L3 Collab., C. Dionisi *et al.*, Nucl. Inst. Meth. **A336** (1993) 78.

[25] M. Fukushima, L3 Internal Note # 520 (1987);
C. Luci, L3 Internal Note # 2480l (1999);
C. Luci, L3 Internal Note # 2616a (2000).

Chapter 4

Reconstruction and Simulation

4.1 Event Reconstruction

The online system of the L3 detector basically provides raw detector quantities. These data are processed further by the reconstruction program [1]. The reconstruction includes the application of calibration constants, the construction of physically motivated objects such as tracks, calorimetric clusters, their cross assignment (track $\rightleftharpoons$ cluster), muons. A first classification of the event is made by assigning it to one or more analysis streams such as the hadronic stream, the tau stream or a stream related to new physics. The reconstructed data are written to the tape in three different forms of decreasing complexity.

- DRE (Data REconstructed) format: All most all informations of the raw data are available in this format.
- DSU (Data SUmmary) format: This format allows a redefinition and calibration of high level objects, such as tracks and clusters. Some part of the raw detector informations is still present.
- DVN (Data aVaNti) format: In this only the most important reconstructed quantities are stored. The information is sufficient for most analyses and the format provides fastest data access option.

Figure 4.1 shows the schematic view of the flow of data in the L3 reconstruction program starting with the raw detector signals and culminating in objects used in physics analyses.

4.1.1 TEC Track Reconstruction

Reconstruction in the central tracking chamber aims at measuring the momentum and the charge sign of all the charged particles in an event. As a first step, individual track segments in the transverse or bending plane are reconstructed from the hits on the anode wires. The track segments are then split and combined until satisfactory track fits are

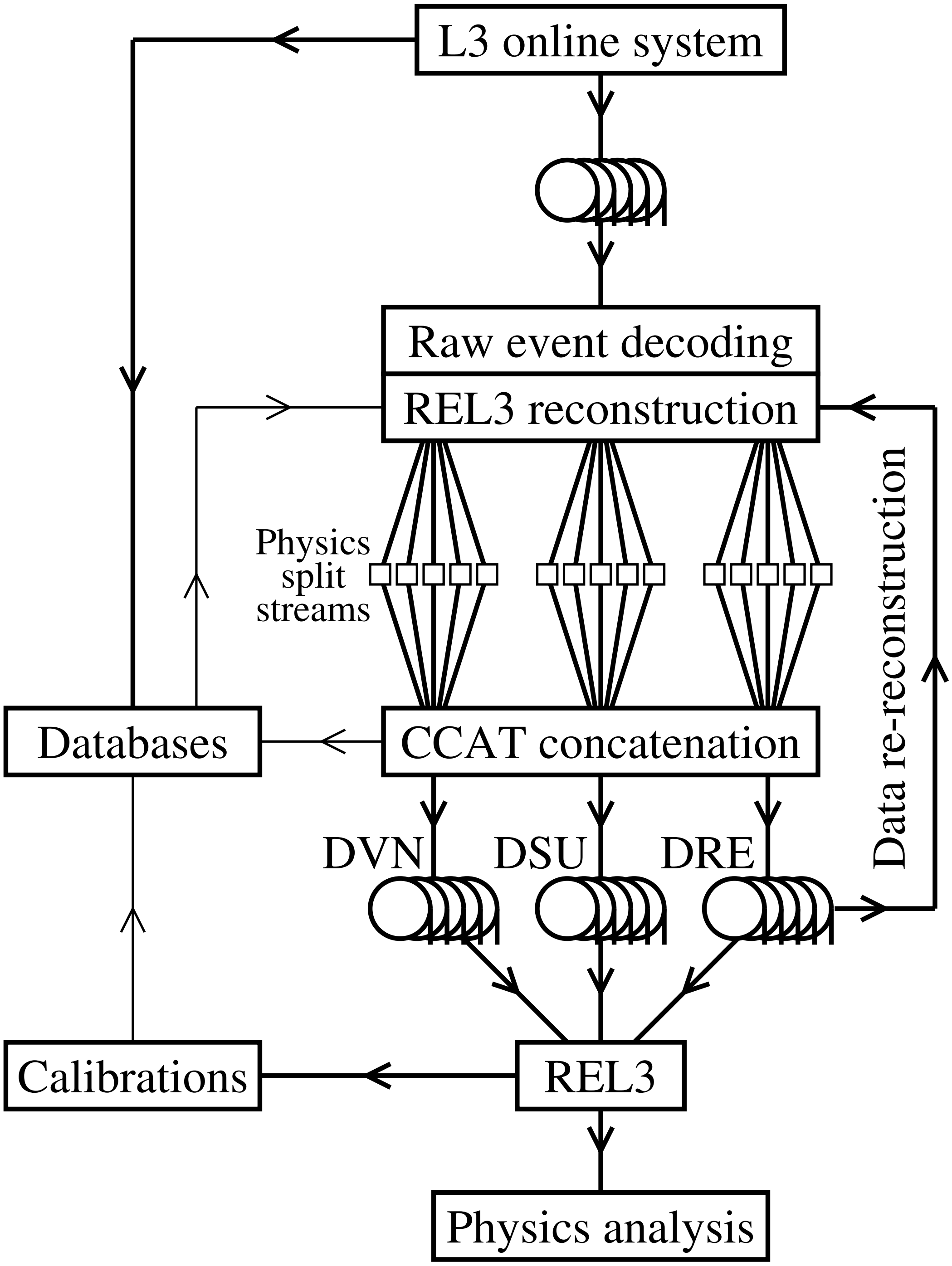

Figure 4.1: Schematic view of the data-flow from online system towards physics analyses.

obtained. By combining the segments in the inner and outer TEC with additional information coming from the SMD, the left-right ambiguities and problem of fictitious tracks are resolved. The polar angle θ is found out by combining information from the TEC with that obtained from the Z chambers. The basic set of parameters for a reconstructed track [2] consists of (see the side-by figure)

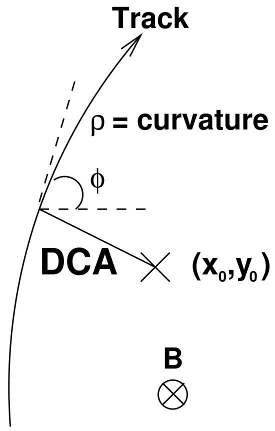

- number of hits on the track (N_{hit}),
- distance between the innermost and outermost hits (Span),
- momentum of the track ($p = p_T/\sin\theta$),
- distance of closest approach to the interaction vertex (DCA),
- azimuthal angle ϕ at the point of closest approach, and
- χ^2 of the track fit.

These parameters are used to select "good tracks" for physics analysis. In the following table, the adopted selection criteria used for selecting good track is summarised.

$\chi^2 > 0.0$	$N_{hit} > 3$	$N_{hit}/\text{Span} > 0.5$	$p_T > 200$ MeV	DCA < 50 mm

4.1.2 Electromagnetic Cluster Reconstruction

The purpose of cluster reconstruction in the electromagnetic calorimeter is to determine energy and directions of the particles interacting with the BGO. The energy deposits, each with value greater than the threshold of 10 MeV, are grouped together in the (θ, ϕ) plane. In an iterative procedure, local energy maxima or *bump* are selected with energy above 40 MeV and combined with the neighbouring bumps to form clusters. In principle, a bump represents single particle while a cluster would be a group of particles. In case of a cluster, the raw energy is calculated by summing all the energy deposits assigned to the cluster, while the direction is found from the centre-of-gravity of all assigned deposits. The raw energy is corrected by taking various loss factors *e.g.* lateral leakage into account. The cluster then could be classified as of electromagnetic origin, hadronic origin, or due to minimum ionising particle depending on the profile of the energy deposition. As an example, in Figure 4.2 the expected shower shape from a photon (an electromagnetic particle) is compared against that of a hadron. The quantities connected to the definition of a cluster are

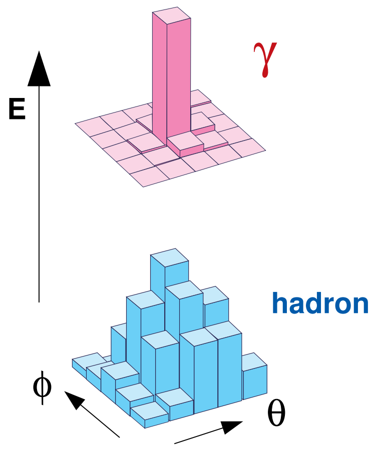

Figure 4.2: Shower shapes in the BGO Calorimeter.

- number of crystals assigned to the cluster ($N_{crystal}$),

- energy in 3×3 (E_9) and 5×5 (E_{25}) crystal matrices around the central crystal, and
- χ^2 of the shower shape fit assuming the cluster to be of electromagnetic origin.

4.1.3 Calorimeter Cluster Reconstruction

The hits seen in the hadron calorimeter are clustered in a similar way to the cluster reconstruction in the ECAL. The association, however, is more complex due to three dimensional nature of the hits. Thus clustering is performed both in the angular as well as radial directions unlike the case with ECAL. The resulting clusters in the hadron calorimeter are identified as either hadronic cluster or minimum ionising signal. These clusters are geometrically matched with the clusters of the ECAL, if the hadron cluster has energy deposited in the front part of the HCAL. The resulting object is called A Smallest Resolvable Cluster, or ASRC. It corresponds to either an electromagnetic cluster matched with a hadron calorimeter cluster, or else to an unmatched cluster having presence only in the HCAL. Besides the quantities connected to the definition of an electromagnetic cluster, the ASRC also carries the following informations of the hadron cluster on

- the hadronic energy of the cluster (E_{HCAL}), and
- the shower shape of the hadronic component.

For selecting good clusters considering the available informations from the ECAL and HCAL, the following set of quality cuts is used.

Type–1	$E_9 > 0.1$ GeV, $E_{\mathrm{HCAL}} > 0.9$ GeV	default ASRC type
Type–2	$E_9 > 0.1$ GeV, $N_{\mathrm{crystal}} > 1$	against hot BGO crystal and dead HCAL
Type–3	$E_9 = 0.0$ GeV, $E_{\mathrm{HCAL}} > 1.4$ GeV	reject the possibility of dead BGO
In each of the three cases, total ASRC energy is required to be at least 0.1 GeV.		

4.1.4 Muon Track Reconstruction

Tracks in the outer muon chambers are reconstructed by combining the hit signals in each of the three P-layers into track segments. Subsequently segments within one octant are used for building tracks. As the final step, tracks crossing octant boundaries are matched. The track momenta are corrected for energy loss due to multiple scattering in the calorimeters. Relevant track parameters are

- number of P and Z segments,
- momentum of the track as measured in the muon chamber,
- DCA after backtracking to the interaction point both in $r\phi$ and rz planes,
- significance on the DCAs on $r\phi$ and rz planes after track fitting,

- time of flight as measured by the scintillation counters, and
- energy deposited in the calorimeters (required for selecting MIP muon).

In Chapter 5, the selection methodology for muon identification is discussed in detail.

4.2 Monte Carlo Simulation

For precise measurements, the detailed understanding of the various detector components is inevitable. In high energy physics experiments, the description of the underlying physics processes (Event Generation) and the response of the detector (Detector Simulation) are obtained through Monte Carlo simulations.

4.2.1 Event Generation

Random events are generated according to probability distributions predicted by the physical theory (which may be just a model!). For each event, the particles are stored in form of particle identifications and energy-momentum four-vectors. Theoretical predictions for the observable quantities such as cross section, mass, decay width *etc.* are calculated by averaging over a large number of events. The point to be noted here is that none of the detector characteristics are used at this stage.

4.2.2 Detector Simulation

The next step after the event generation is the detailed simulation of the detector response. Each particle is tracked through the detector where the effect of energy loss, multiple scattering, showering in the detector materials is properly taken into account. All final particles are traced until they are either absorbed or leave the experimental setup. The final step is a simulation of the response of all the sensitive detector components. The L3 detector simulation is based on the detector simulation package **GEANT** [3]. For the simulation of hadronic interaction, GEISHA [4] program package is used. Time dependent detector inefficiencies *e.g.* inefficient TEC wires, noisy BGO crystals, or dead HCAL cells are reproduced in these simulations, as they are monitored during data taking periods. After detector simulation, both the data and simulated events exist in the same format. For physics analysis, they are treated alike so that the measured quantities could be compared against the simulated ones.

4.3 Data and Monte Carlo Samples

Our study comprises of the data samples collected by the L3 detector at $\sqrt{s} = 183$ GeV up to the highest energy achieved at LEP. Exact break-up of the integrated luminosity as a function of $\sqrt{s}$ is given in Table 4.1.

$\sqrt{s}$ (GeV)	$\mathcal{L}_{\text{int}}$ (pb^{-1})
182.7	55.3
188.6	176.8
191.6	29.7
195.5	83.7
199.5	82.8
201.7	37.0
205.1	77.8
206.8	138.8
Total	681.9

Table 4.1: Data luminosity analysed at different centre-of-mass energies.

The EXCALIBUR [5] Monte Carlo program is used to generate both the signal and background processes originating from neutral-current four fermion processes. Background processes which could mimic our signal are the QCD process, $e^+e^- \to q\bar{q}$, with leptons mostly coming from heavy quark decay and the semi-leptonic decay of W^+W^- events. They are generated using the KK2F [6] and KORALW [7] Monte Carlo programs respectively. To take care of possible contributions from two-photon hadronic final state, $e^+e^- \to (q\bar{q})e^+e^-$, we have used PHOJET [8] event generator. Table 4.2 gives an idea about the typical cross section and the size of the Monte Carlo sample of the various Standard Model processes studied.

The SM processes	No. of events	σ (pb)
$e^+e^- \to q\bar{q}$	909400	81.013
$\to W^+W^-$	407750	17.534
$\to q\bar{q}\ell^+\ell^-$(sig)	5818	0.157
$\to q\bar{q}\ell^+\ell^-$(bck)	59172	2.133
$\to (q\bar{q})e^+e^-$	6998000	16322.
$\to q\bar{q}q'\bar{q}'$	13000	1.019

Table 4.2: Typical size of the Monte Carlo sample and expected cross sections for different Standard Model processes studied (the given values correspond to $\sqrt{s} = 205\,\text{GeV}$). Here the 'sig' (signal) and 'bck' (background) are defined from the same $q\bar{q}\ell^+\ell^-$ sample after putting the signal definition cut.

4.3.1 Signal Definition

The signal process, $e^+e^- \to ZZ$, results in four fermion final state. There are also other neutral and charged current processes leading to same final state. Thus a set of phase space cuts [10] is applied to disentangle the signal out of the whole class of four-fermion final states. The invariant masses of the fermion pairs of same flavour are required to lie between 70 and 105 GeV. In case of final state with four leptons of same flavour, this criterion should be satisfied by any one of the two possible pairings. This is to reject the contributions from $Z\gamma^\star$ and $\gamma^\star\gamma^\star$ mediated final states. For the $q\bar{q}e^+e^-$ final state, an additional condition of $|\cos\theta_e| < 0.95$ is required to reject the remnants of multiperipheral diagram (θ_e is the polar angle of the e^+/e^-). The possibility of the four fermions originating from the decays of W-pair is vetoed by requiring the masses of the susceptible pair not to lie between 75 and 85 GeV. Figure 4.3 clearly shows the significance of the phase space cut on separating signal events from other four-fermion final states.

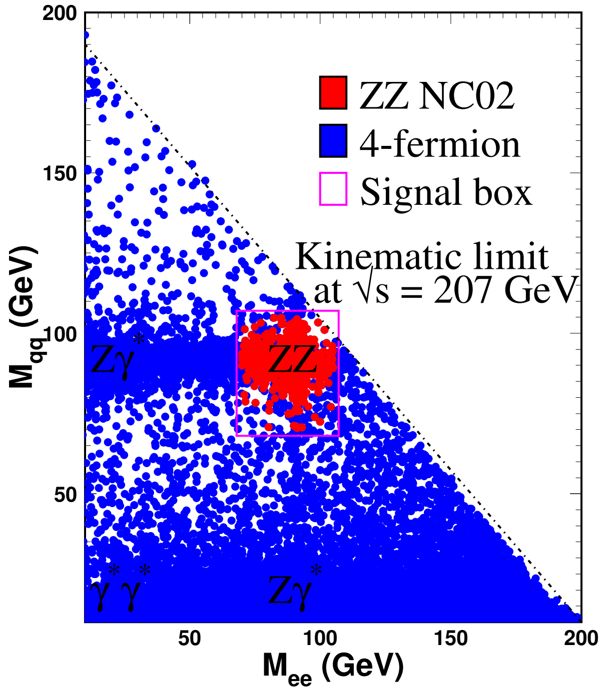

Figure 4.3: Utility of ZZ signal definition cuts: the distributions of (a) $M_{q\bar{q}}$ *vs* $M_{e^+e^-}$, and (b) $|\cos\theta_e|$ for the $q\bar{q}\ell^+\ell^-$ Monte Carlo sample.

4.3.2 Final State Studied

Out of all possible final states emerging out of Z-boson pair production, we have studied the one where one of the Z's decays to $q\bar{q}$ leading to two hadronic jets and other Z to a pair of leptons. Despite clean event topology due to presence of two well isolated leptons in the aforesaid final state, relatively low event rate (event fraction $\simeq$ 14%) requires delicate balance between lepton identification and kinematic selection. This forms the part of the following chapter, before we move over to measurements.

References

[1] S. Banerjee and F. Bruyant, L3 Note # 748 (1989).

[2] J. Alcaraz, L3 Note # 1666 (1995).

[3] GEANT Version 3.14 is used:
R. Brun *et al.*, "GEANT 3", CERN DD/EE/84-1 (Revised), September 1987.

[4] H. Fesefeldt, RWTH Aachen Report PITHA 85/02 (1985).

[5] EXCALIBUR Monte Carlo Program:
F.A. Berends *et al.*, Comp. Phys. Comm. **85** (1995) 437.

[6] KK2F Monte Carlo Program:
QCD parton shower and fragmentation process are taken from JETSET 7.4 [9];
S. Jadach *et al.*, Phys. Lett. **B449** (1999) 97.

[7] M. Skrzypek *et al.*, Comp. Phys. Comm. **94** (1996) 216;
M. Skrzypek *et al.*, Phys. Lett. **B372** (1996) 289.

[8] R. Engel, Z. Phys. **C66** (1995) 203;
R. Engel and J. Ranft, Phys. Rev. **D54** (1996) 4244.

[9] JETSET 7.4 Monte Carlo Program:
T. Sjöstrand, Comp. Phys. Comm. **82** (1994) 74.

[10] L3 Collab., M. Acciarri *et al.*, Phys. Lett. **B450** (1999) 281.

Chapter 5

Selection of $e^+e^- \to ZZ \to q\bar{q}\ell^+\ell^-$ Events

The goal of event selection is to obtain a large (efficiency) as well as pure (purity) signal sample, which could be later used to measure the cross section or search for new physics. This chapter explains all the steps involved in selecting the signal event, $e^+e^- \to ZZ \to q\bar{q}\ell^+\ell^-$.

5.1 Event Topology and Preselection

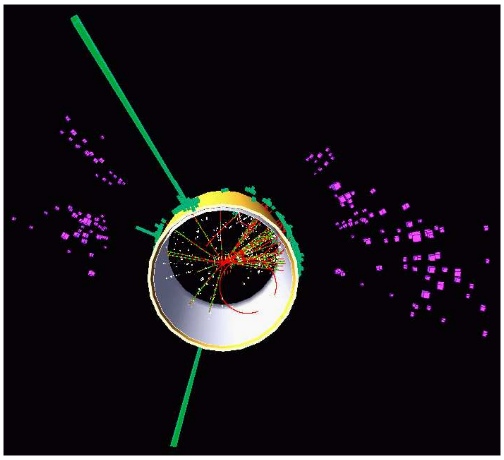

Figure 5.1: A typical $q\bar{q}\ell^+\ell^-$ event.

Topology of our signal event is characterised by two well isolated leptons and two hadronic jets recoiling against them (Figure 5.1). The distinctness of the signal topology in comparison to the background processes could be used at the preliminary stage of selection or preselection to reduce the obvious "background-type" events from the data sample without affecting the signal efficiency much. The preselection requirements are as follow :

- Balanced event topology with large visible energy and small missing momentum; $E_{vis}/\sqrt{s} > 0.45$, $E_{\perp}/E_{vis} < 0.4$ and $|E_{||}/E_{vis}| < 0.35$
- Large track and cluster multiplicity; # Track > 6 and # Cluster > 14
- Event with large effective centre-of-mass energy (veto on return-to-Z event); $\sqrt{s'}/\sqrt{s} > 0.55$
- Spherical event topology (rejection of two-jet like event); event Thrust < 0.96
- Thrust axis should point away from the beam-pipe (reject two photon background); $|\cos\theta_{thrust}| < 0.98$

Figure 5.2 – 5.3 show the distributions of the preselection variables for all energy-points added together. The agreement between the data and Monte Carlo is found to be good. Table 5.1 summarises the performance at preselection level.

N_{signal}	$N_{background}$	N_{tot}	N_{data}	$\epsilon_{q\bar{q}e^+e^-}$	$\epsilon_{q\bar{q}\mu^+\mu^-}$	$\epsilon_{q\bar{q}\tau^+\tau^-}$
78.7	21798.8	21877.5	22126	96.7	85.4	91.0

Table 5.1: Summary of the preselection performance in terms of signal, background, total event expected from Monte Carlo, observed data and efficiency of individual sub-channels.

5.2 Lepton Identification

The leptons; electron, muon and tau, are identified in the L3 detector using their characteristic signatures. Optimal identification method is devised to select good candidates in each category.

5.2.1 Electron Identification

An electron is identified by demanding a well isolated electromagnetic bump in the BGO calorimeter with an associated track in the tracking chamber (TEC). In order to ascertain the electromagnetic origin of the bump, we require the ratio of the energy sums of a 3×3 and 5×5 crystal map around the central crystal, $(\frac{E_9}{E_{25}})$, to be greater than 0.95. This quantity is corrected [1] by taking the lateral energy leakage in a standard electromagnetic shower into account. Due to narrow lateral shower profile caused by the electron, the ratio is closer to one. For the hadron it is quite smaller, since hadronic shower is wider in shape. Figure 5.4(a) shows the distribution of $(\frac{E_9}{E_{25}})$ as expected for an electron compared to that of the hadron. The case of electron inside the jet is rejected by constraining the energy deposited in the hadron calorimeter behind the bump, E_{HCAL}, to be at most 10% of the bump energy. Figure 5.4(b) compares the ratio of E_{HCAL} to the energy of an isolated

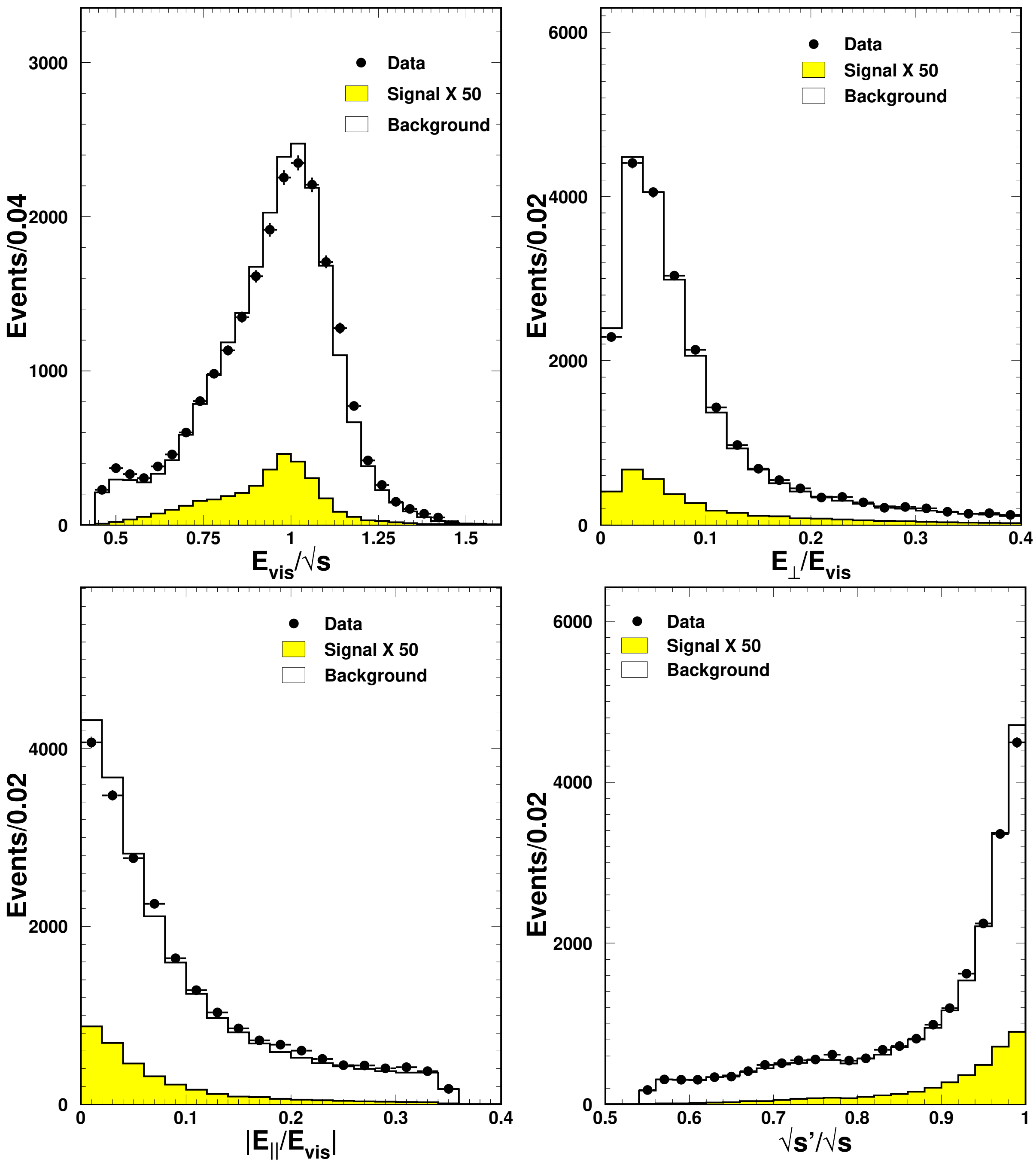

Figure 5.2: Distributions of the preselection variables: normalised (a) Visible energy, (b) Transverse energy imbalance, (c) Parallel energy imbalance, and (d) Effective centre-of-mass energy. All data are added together and the signal event is scaled up by 50.

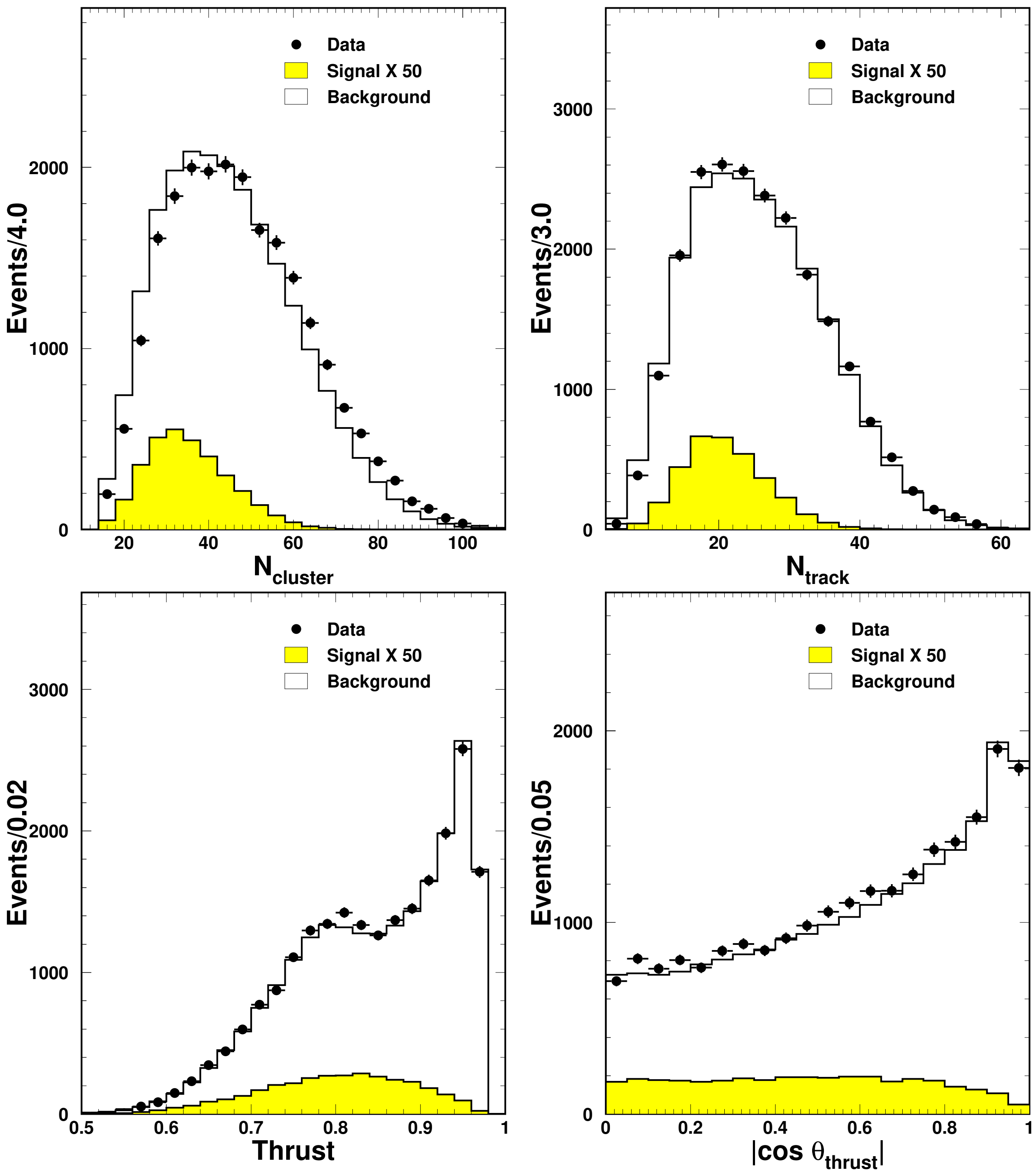

Figure 5.3: Distributions of the preselection variables: (a) # Cluster, (b) # Track, (c) Event Thrust, and (d) $|\cos\theta_{\mathrm{thrust}}|$. All data are added together and the signal event is scaled up by 50.

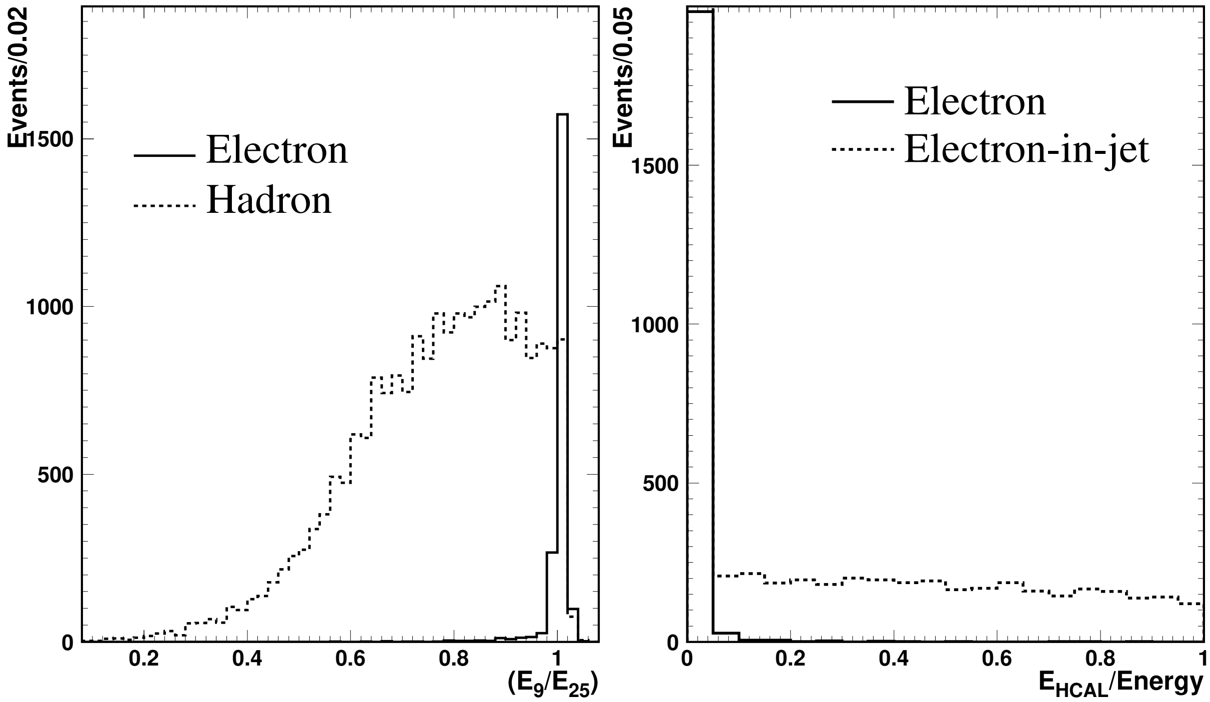

Figure 5.4: Distributions of the electron identifying variables; $(\frac{E_9}{E_{25}})$ and (E_{HCAL}/E) as expected in the controlled samples: $e^+e^- \rightarrow e^+e^-$ and $e^+e^- \rightarrow q\bar{q}$.

electron against the electron inside jet. As expected, for the isolated electron the ratio is closer to zero unlike the later. Photon and electron look alike inside the BGO. However, the electron leaves behind a trail of track in the TEC pointing to the bump measured in the BGO. The matching of the track and the bump can be used to distinguish between electron and photon. The matching is done in the $r\phi$ plane requiring $\Delta\phi$ $(|\phi_{\text{bump}} - \phi_{\text{track}}|)$ to be at most 15 mrad for the barrel part of the detector. For the end-cap, this criterion has been relaxed up to 40 mrad to encompass the insensitivity of the TEC in this region leading to badly measured track. To improve on the detection coverage, electrons in the gap calorimeter (EGAP) are also considered. Unlike the barrel and end-cap part, with EGAP one can not use the lateral shower information to select the electron due to bad energy resolution that leads to partial lateral shower containment. Here the electron is selected by using the informations from the hadron calorimeter behind EGAP (isolation) and the tracking chamber (track–matching). Figure 5.5 shows the matching in $\Delta\phi$ as a function of polar angle of the electron, and the relative number of electrons selected in the different parts of the calorimeter.

5.2.2 Muon Identification

Muon, being a minimum ionising particle (MIP), can easily penetrate through a large depth of matter without being disturbed too much. At L3, it is identified by a simulta-

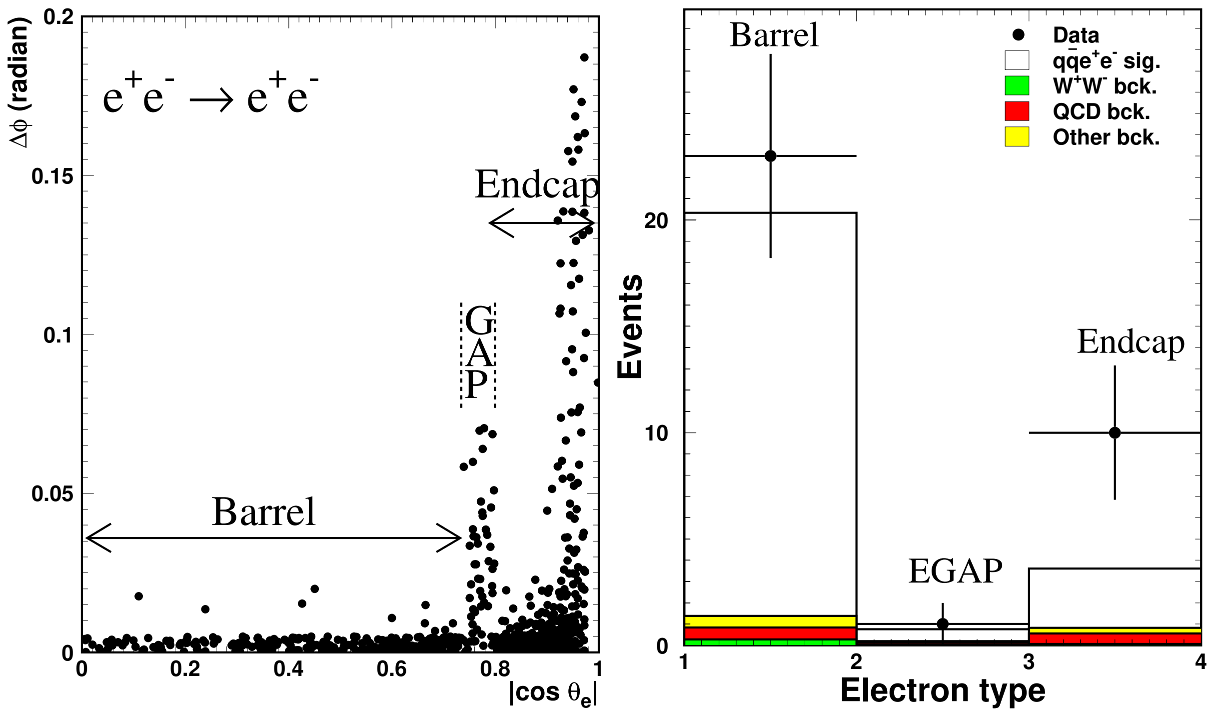

Figure 5.5: Distributions for $\Delta\phi$ *vs* $|\cos\theta_\mathrm{e}|$ in the controlled sample, $e^+e^- \to e^+e^-$, and the number of electrons selected in various parts of the detector.

neously matched track in the TEC and the outer muon chamber (MUCH) along with an associated MIP signal in the calorimeter [2]. Moreover, the energy deposition due to the muon is very much localised in space involving only few number of contiguous clusters. Considering all these properties, following quality cuts are applied to select the muon:

$$\begin{array}{rcl@{\qquad\qquad}rcl} \chi^2_\mathrm{norm} & < & 8.0 & (\mathrm{E}_{15}/\mathrm{E}) & < & 0.3 \\ (\frac{\mathrm{DCA}}{\sigma_\mathrm{DCA}})_\phi & < & 4.0 & |(\frac{\mathrm{DCA}}{\sigma_\mathrm{DCA}})_\mathrm{z}| & < & 4.0 \\ \mathrm{DCA}_\phi & < & 200\ \mathrm{mm} & |(\mathrm{DCA}_\mathrm{z})| & < & 150\ \mathrm{mm} \end{array}$$

where χ^2_norm is the χ^2 per degrees of freedom for matching the track reconstructed inside the TEC and MUCH, $\mathrm{DCA}_{\mathrm{z}(\phi)}$ is the distance of closest approach of the muon track to the primary vertex in rz $(r\phi)$ plane, σ_DCA is the r.m.s. variation on those quantities and E_{15} is the energy deposited in the calorimeters (both ECAL and HCAL) within 15° half-angle cone around the muon direction. Cuts on the DCAs and their significances are designed to suppress the cosmic ray background, whereas cut on $(\mathrm{E}_{15}/\mathrm{E})$ is for isolating the muon from neighbouring hadronic activity. A typical distribution of $(\mathrm{E}_{15}/\mathrm{E})$ for a good muon is compared with that of a muon inside jet in Figure 5.6(a). Muon that fails to give signal in the outer muon chamber can still be selected, if the profile of energy deposition in the calorimeters can be interpreted as due to a MIP having an associated track in the TEC. Muon falling under this category is referred as “AMIP muon” whereas the one reconstructed in the muon chamber is called “AMUI muon” throughout the thesis.

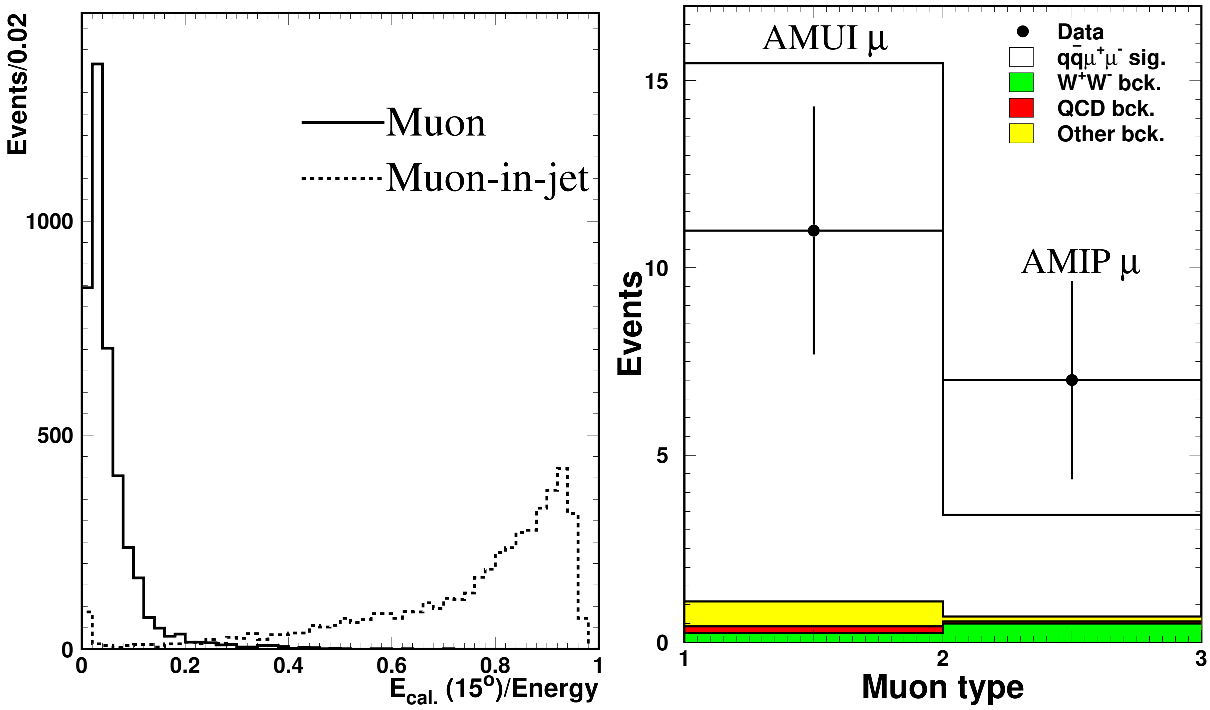

Figure 5.6: Distributions of the (E_{15}/E) in the controlled samples: $e^+e^- \rightarrow \mu^+\mu^-$ and $e^+e^- \rightarrow q\bar{q}$, and the number of selected AMUI and AMIP muons in the sample.

Selection of AMIP muon is particularly useful to take care of limited muon detection coverage in the extreme forward region. Figure 5.6(b) shows the relative fraction of muon identified as AMUI and AMIP in the selected sample.

5.2.3 Tau Identification

Tau leptons are short lived particles with a life time of about 2.9×10^{-13} second which corresponds to a decay flight length of ≈ 2 mm (for τ coming from Z-decay). Hence, only the visible decay products are observed in the detector. They carry a part of the initial energy of the τ-lepton, the remaining part goes undetected via neutrinos. Moreover, given the large boost available for the τ ($\beta \approx 0.999$), all the decay products are produced in a very narrow cone around its flight direction. Keeping this in mind, we have used cone algorithm (Figure 5.7) [3] to reconstruct the τ from its decay product. Here an energetic particle is taken as the seed of the jet and all the particles detected within a 15° cone are combined to get the jet energy and direction. The branching ratio $\tau \rightarrow \ell\nu\nu$ ($\ell =$ e or μ) amounts to 35% while hadronic decay mode covers the remaining 65% [4]. The hadronic decay mode includes both the decay to one charged particle (1-prong decay) or three charged particles (3-prong decay) with a relative ratio of 10:3. To take care of that, if an identified electron or muon matches with the cone jet, we consider it as a leptonic τ candidate. A hadronic τ candidate is selected with the following quality cuts:

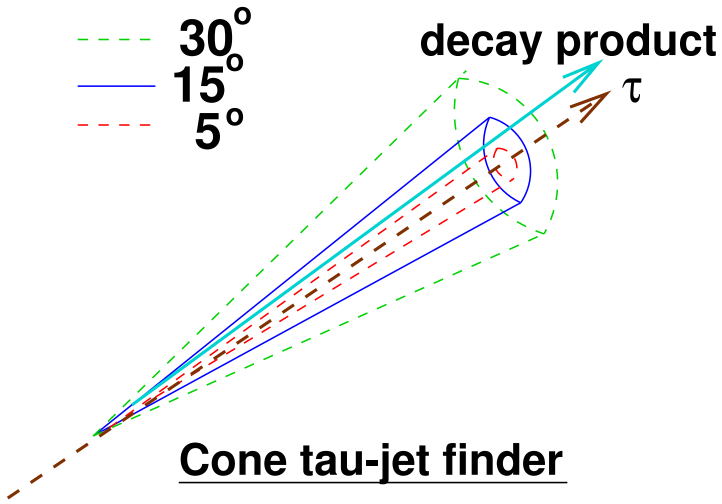

Figure 5.7: Principle of the cone τ-jet finder.

$$\begin{array}{rcl@{\qquad\qquad}rcl} (E_{jet}/\sqrt{s}) & \leq & 0.45 & (E_5/E_{30}) & \geq & 0.65 \\ \#\ \text{Track} & \in & [1,3] & \#\ \text{Cluster} & \leq & 8 \\ p_T^{max}\ (\text{GeV}) & \leq & 1.80 & & & \end{array}$$

where $E_{5(30)}$ is the energy associated within $5°(30°)$ cone around the jet direction and p_T^{max} is the maximum p_T[1] of a constituent particle with respect to the jet-axis. Figure 5.8 show the distributions for jet cluster and track multiplicity for τ and QCD jets.

5.2.4 Lepton Identification Efficiency

The lepton identification efficiency is computed from the $e^+e^- \rightarrow ZZ \rightarrow q\bar{q}\ell^+\ell^-$ Monte Carlo sample by taking the ratio of event selected at least with two reconstructed leptons

Electron	:	83%
Muon	:	64%
Tau	:	56%

Table 5.2: Summary of the lepton identification efficiency.

to the total number of event generated. Table 5.2 summarises the obtained efficiency with the adopted identification algorithm.

5.3 Kinematic Reconstruction

For the full reconstruction of the $q\bar{q}\ell^+\ell^-$ final state, we need to identify two hadronic jets (quarks manifest themselves only via narrow cone of hadrons emanating along their

[1] Both p_T and particle multiplicity are functions of the phase-space or invariant mass of the system.

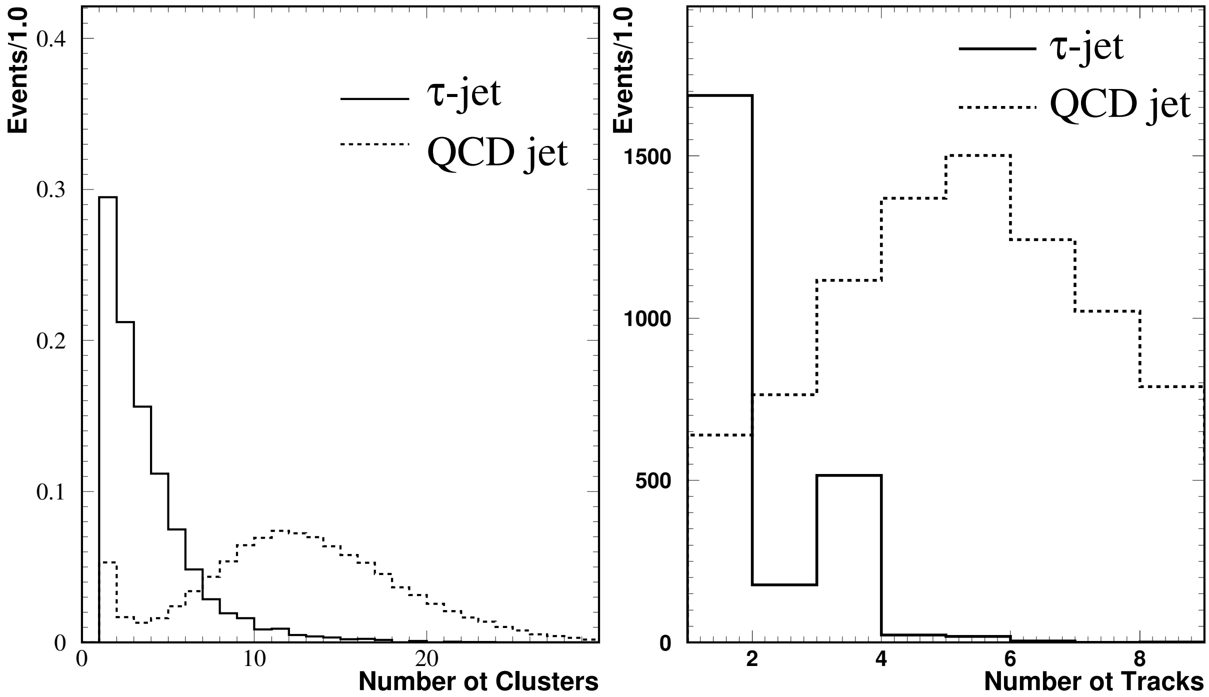

Figure 5.8: Distributions for (a) jet cluster and (b) track multiplicity, as expected in the controlled samples: $e^+e^- \to \tau^+\tau^-$ and $e^+e^- \to q\bar{q}$.

axes) in addition to two leptons. Also, a constrained kinematic fit is performed to use effectively all the informations available in the event.

5.3.1 Jet Clustering Algorithm

Clustering algorithms are used to combine energy deposits in the detector into larger unit to reveal the physical origin of an event. Particularly, so for the hadronic jet. In L3, we have access to the tracks reconstructed in the tracking chamber, to the clusters of calorimetric energy and to the muon momenta measured in the muon chamber. With all these informations at hand, individual clusters are combined into pseudo-particles by using the Durham algorithm [5]. Two particles, i and j, are combined into a pseudo-particle, if the parameter

$$y_{ij} \;=\; 2\frac{\min(E_i^2, E_j^2)}{E_{\text{vis}}^2}(1-\cos\theta_{ij}) \tag{5.1}$$

is below some pre-defined cutoff value y_{cut}, where $E_{i,j}$ are the energies of the particles, θ_{ij} is the opening angle between them, and E_{vis} is the total visible energy. The algorithm loops over all possible combinations of (i, j) and combines the particles with the smallest y_{ij} first. After having combined all particles, we have a new list of pseudo-particles which is then further subjected to Equation 5.1. This iteration continues till the full event (minus the two identified leptons) is clustered into two jets.

5.3.2 Kinematic Fit

In a $q\bar{q}\ell^+\ell^-$ event, owing to large fluctuation associated with a hadronic shower, the jet energies and angles are not so well measured as those of the leptons. Thus in order to improve the mass resolution of the reconstructed particles (here both the jets and leptons are referred as particles), a kinematic fit [6] is performed on the event. This is done by varying the four momenta of the particles within the resolution imposing the energy-momentum conservation (4C fit):

$$\sum_{i=1}^{4} \mathrm{E}_i \;=\; \sqrt{s}, \qquad \sum_{i=1}^{4} \vec{\mathrm{P}}_i \;=\; \vec{0}. \tag{5.2}$$

In such a fit, the measured parameters are varied until a solution is found which satisfies the constraints imposed and also minimises the χ^2 difference between the measured and fitted values:

$$\chi^2(\vec{x}, \vec{\lambda}) \;=\; (\vec{x} - \vec{x}_0)^\dagger \mathrm{V}^{-1} (\vec{x} - \vec{x}_0) + 2\vec{\lambda} \cdot \vec{f}(\vec{x}). \tag{5.3}$$

Here $\vec{x}_0$ represents the measured variables, V is the covariance or error matrix for the measured variables, $\vec{x}$ represents the variables to be varied in the fit, $\vec{f}(\vec{x})$ represents the constraint functions, and λ are the Lagrange multipliers. Figure 5.9 shows the relative

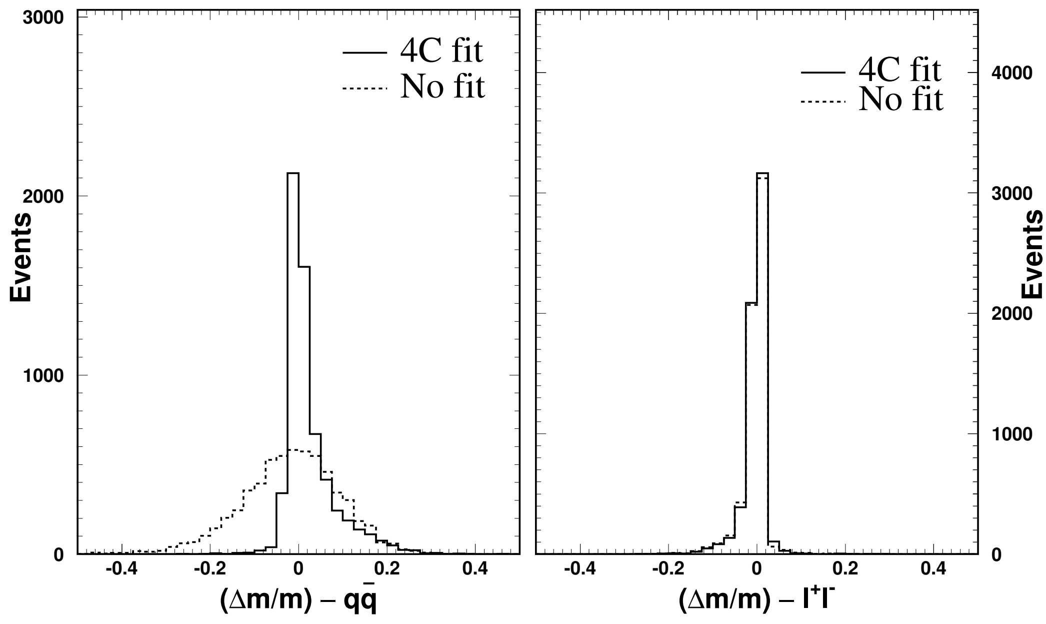

Figure 5.9: Relative change in the di-jet and di-lepton mass resolutions after the kinematic fit in the $q\bar{q}e^+e^-$ final state.

change in the di-jet and di-lepton masses before and after performing the fit. We find significant improvement in the di-jet mass resolution to about 5%, while for the di-lepton case there is practically no change. This is very much expected, in particular, for the $q\bar{q}e^+e^-$ and $q\bar{q}\mu^+\mu^-$ final states where the energy and angle of the leptons are precisely measured. The fact that both the Z's are resonantly produced is further utilised in the fit by constraining the di-jet and di-lepton masses to be equal. The resultant mass is referred as "5C-fit mass" or "equal mass" in the subsequent sections. The equal mass fit further improves the mass resolution resulting in better background rejection.

5.4 Event Selection

The selection procedure [7] evolves around the fact that, both the Z's are produced on the mass-shell leading to constraints on the reconstructed masses of the di-quark and di-lepton systems and finite boost for Z allowing to restrict on the energy-sharing or opening angle between the daughter particles. An optimal set of selection variables, meeting the above requirements, is chosen to discriminate the signal and background processes.

The precise values of the cuts are determined by minimising [8] the relative error on the expected signal cross section, $\left(\frac{\Delta\sigma_s}{\sigma_s}\right)$, with respect to the cut positions:

$$\left(\frac{\Delta\sigma_s}{\sigma_s}\right) = \sqrt{\frac{1}{\mathcal{L}_{\rm int}} \cdot \frac{\sigma_{\rm sig} + \sigma_{\rm bck}}{\sigma_{\rm sig}^2} + \left(\frac{\Delta\sigma_{\rm bck}}{\sigma_{\rm sig}}\right)^2 + \left(\frac{\Delta\epsilon_{\rm sig}}{\epsilon_{\rm sig}}\right)^2} \qquad (5.4)$$

where $\sigma_{\rm sig(bck)}$ and $\epsilon_{\rm sig}$ are the accepted signal(background) cross section and signal efficiency after the selection cuts and $\Delta\sigma_{\rm bck}$ and $\Delta\epsilon_{\rm sig}$ are the errors on accepted background cross section and signal efficiency calculated assuming Binomial statistics. Figure 5.10 illustrates the utility of cut optimisation for one of the selection variables, $M^{4C}_{q\bar{q}} + M^{4C}_{\mu^+\mu^-}$.

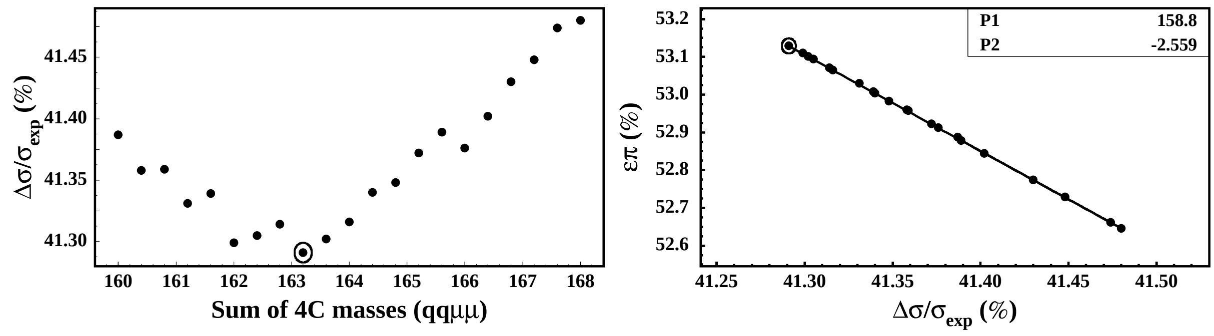

Figure 5.10: Distributions showing (a) change in relative error on the expected cross section with respect to change in cut position for the selection variable, $M^{4C}_{q\bar{q}} + M^{4C}_{\mu^+\mu^-}$, and (b) linear correlation between the error and the quality factor of selection.

As it is seen in Figure 5.10(a), the relative expected error is minimum at the adopted cut position indicated by the empty circle. The optimal nature of the analysis is further demonstrated in Figure 5.10(b) by showing linear correlation between the relative error and the quality factor (efficiency$\times$purity).

In the following sections, the selection variables are described one by one for each of the sub-channels; $q\bar{q}e^+e^-$, $q\bar{q}\mu^+\mu^-$ and $q\bar{q}\tau^+\tau^-$. The accompanying figures are the plots of the variables with all data combined. In these figures, all cuts except the one on the selection variable plotted are applied, to show the importance of that variable. The arrow indicates the typical cut position used at $\sqrt{s} = 189$ GeV, which are retuned at each energy to take care of changed event topology.

5.4.1 $q\bar{q}e^+e^-$ Sub-channel

Transverse energy imbalance: The $q\bar{q}e^+e^-$ event is characterised by large visible energy with small energy imbalance both along and transverse to the beam axis. In comparison, one of the major backgrounds, $W^+W^- \rightarrow q\bar{q}'e\nu$, is signalled by large imbalance due to the presence of neutrino. Thus, a cut on the transverse energy imbalance rejects most of this background as shown in Figure 5.11(a).
Energy sum of the two electrons: In the reaction, $e^+e^- \rightarrow ZZ \rightarrow q\bar{q}e^+e^-$, energy of each of Z's should be equal to the beam energy. This condition can be rephrased by saying the sum of the two electrons (here positron is also referred as electron for simplicity), or of the two jets should be equal to the beam energy. Since the L3 detector is equipped with excellent energy resolution for the electron, by constraining the energy sum of two electrons to be $\sqrt{s}/2 \pm \sigma_E$, most of the backgrounds can be rejected (see Figure 5.11(b)). Here σ_E is the energy resolution of the electron.
Energy variable: Energy variable [9] is the measure of uniformity on energy sharing among the four daughter particles, and is given by the following expression :

$$\text{Energy variable} \;=\; \frac{E_1 + E_2 - E_3 - E_4}{E_1 + E_2 + E_3 + E_4}. \tag{5.5}$$

Here E represents the ordered energy *i.e.* E_1 is the energy of the most energetic particle and so on. For the signal event, the energy is quite uniformly distributed among the daughter particles leading to small value for the energy variable. Thus, putting an upper limit on this variable reduces the contribution from the background events with the leptons coming from one of the quark-legs *e.g.* $e^+e^- \rightarrow q\bar{q}$.
Sum of the di-jet and di-electron masses: Since for the signal event the Z particles are resonantly produced, the sum of the di-jet and di-electron masses should be equal to twice the Z mass (182.36 GeV). However, given the di-jet mass resolution and finite width of Z (2.49 GeV), the cut on the sum of the masses is relaxed a bit. This cut mostly gets rid of the contribution from the non-resonant $q\bar{q}e^+e^-$ final state. Table 5.3 summarises all the selection cuts applied for selecting the $ZZ \rightarrow q\bar{q}e^+e^-$ events.

5.4.2 $q\bar{q}\mu^+\mu^-$ Sub-channel

Energy of the second muon: In the signal process, $e^+e^- \rightarrow ZZ \rightarrow q\bar{q}\mu^+\mu^-$, the second muon (second refers to the lesser energetic between the two muons) carries almost half of

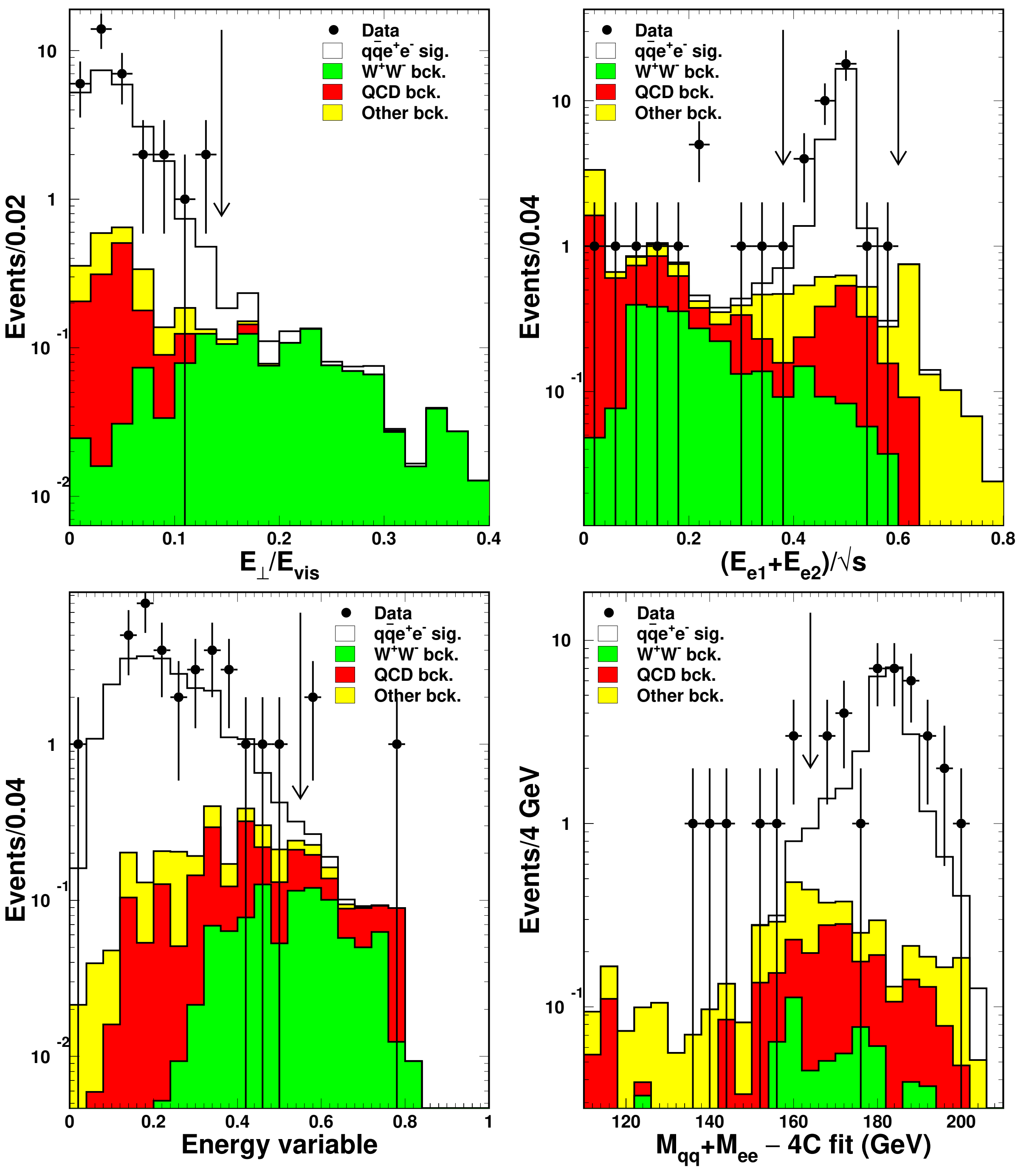

Figure 5.11: (N-1) plots of the selection variables used for selecting $q\bar{q}e^+e^-$ events: (a) Transverse energy imbalance, (b) Sum of the two electrons energies scaled to $\sqrt{s}$, (c) Energy variable, and (d) Sum of di-jet and di-electron masses after the kinematic fit.

Selection variables		Cut position at different $\sqrt{s}$ (GeV):			
		183	189	192–202	205–207
# Electron	$\geq$	2.000	2.000	2.000	2.000
$(E_{\perp}/E_{vis})$	$<$	0.120	0.140	0.140	0.150
$(E_{e1}+E_{e2})/\sqrt{s}$	$\in$	[0.40,0.60]	[0.40,0.56]	[0.40,0.60]	[0.42,0.60]
Energy Variable	$<$	0.600	0.500	0.450	0.520
$M^{4C}_{q\bar{q}} + M^{4C}_{e^+e^-}$ (GeV)	$>$	162.0	160.0	167.0	164.0

Table 5.3: Cuts applied for selecting $ZZ \rightarrow q\bar{q}e^+e^-$ events at different $\sqrt{s}$.

the Z energy *i.e.* $\sqrt{s}/4$. For the background processes, however, it is mostly soft or less energetic. Thus a lower cut on its energy can be used to control the background. Energy of the second muon is preferred over that of the first muon, since it is more precisely measured ($\sigma_p \propto 1/p^2$). Figure 5.12(a) shows the significance of this selection variable.
Sum of the di-jet and di-muon masses: Similar to the $q\bar{q}e^+e^-$ final state, we cut on the sum of the di-jet and di-muon masses to reject non-resonant contributions. Table 5.4 summarises all the selection cuts applied for selecting the $ZZ \rightarrow q\bar{q}\mu^+\mu^-$ events.

Selection variables		Cut position at different $\sqrt{s}$ (GeV):			
		183	189	192–202	205–207
# Muon	$\geq$	2.000	2.000	2.000	2.000
$(E_{\mu 2}/\sqrt{s})$	$>$	0.130	0.140	0.080	0.084
$M^{4C}_{q\bar{q}} + M^{4C}_{\mu^+\mu^-}$ (GeV)	$>$	160.0	160.0	167.0	164.0

Table 5.4: Cuts applied for selecting $ZZ \rightarrow q\bar{q}\mu^+\mu^-$ events at different $\sqrt{s}$.

5.4.3 $q\bar{q}\tau^+\tau^-$ Sub-channel

Normalised visible energy: In the $q\bar{q}\tau^+\tau^-$ final state, there are at least two neutrinos leading to small visible energy and large momentum imbalance. Thus putting an upper cut on normalised visible energy as shown in Figure 5.13(a), one gets rid of the backgrounds with large visible energy *e.g.* $ZZ \rightarrow q\bar{q}q'\bar{q}'$.
Opening angle between two τ's in Z rest frame: This is the opening angle between two taus after deboosting their four momenta to Z rest frame. Here the boost factor of the Z is calculated from the recoiling $q\bar{q}$ system. Ideally, one would expect it to peak around 180°. However, due to large missing energy associated with the signal, it gets distorted to somewhat lower value (Figure 5.13(b)). It has got a reasonable discriminating power to cut down the backgrounds.
Raw hadronic mass: This is the most effective variable to control the background in case of $q\bar{q}\tau^+\tau^-$ final state which is defined as the effective hadronic mass recoiling against

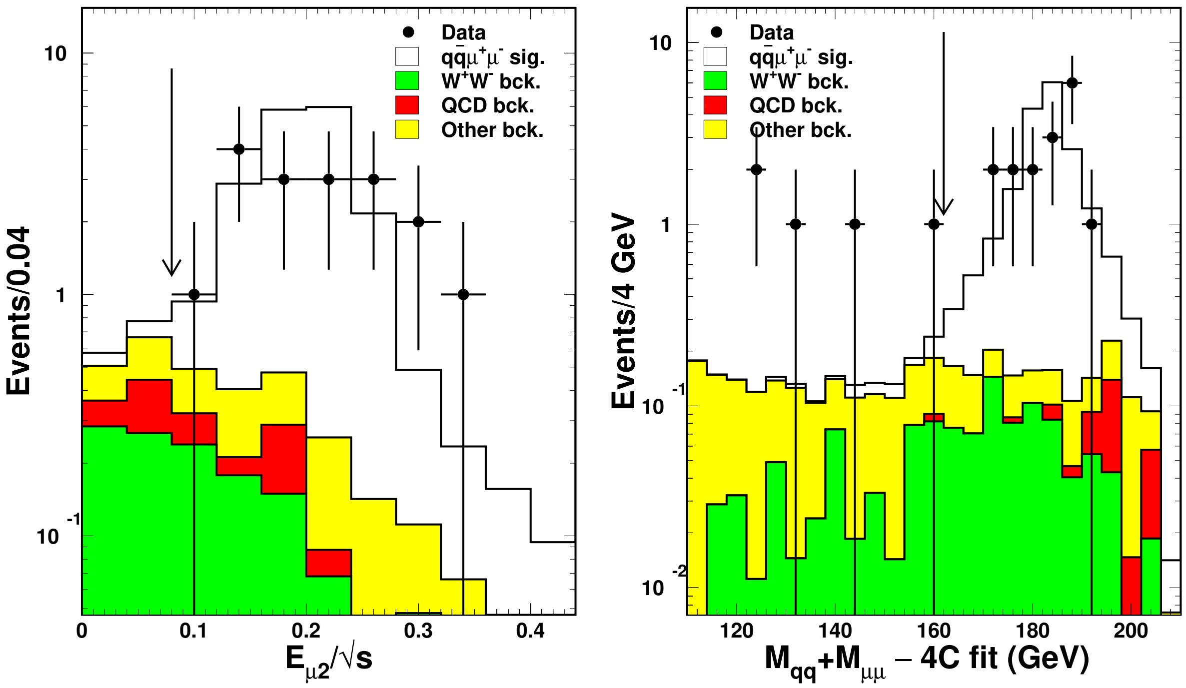

Figure 5.12: (N-1) plots of the selection variables used for selecting $q\bar{q}\mu^+\mu^-$ events: (a) Energy of the second muon scaled to $\sqrt{s}$, and (b) Sum of di-jet and di-muon masses after the kinematic fit.

the $\tau^+\tau^-$ system. It is expected to peak around the Z mass for the signal unlike the backgrounds. Constraining this variable to be $M_Z \pm \Delta$, a significant fraction of the backgrounds mostly from the process, $W^+W^- \to q\bar{q}'\tau\nu$, is rejected. Here Δ is the resolution of the hadronic mass.

Sum of the di-jet and di-tau masses: For the $q\bar{q}\tau^+\tau^-$ final state, the kinematic fit works reasonably well despite bad energy resolution of the $\tau^+\tau^-$ system. Thus putting a cut on the sum of the di-jet and di-tau masses obtained after the kinematic fit, we get rid of some part of the backgrounds mostly from the non-resonant diagrams. Table 5.5 summarises all the selection cuts applied for selecting the $ZZ \to q\bar{q}\tau^+\tau^-$ events.

Selection variables		Cut position at different $\sqrt{s}$ (GeV):			
		183	189	192–202	205–207
# Tau	$\geq$	2.000	2.000	2.000	2.000
$(E_{vis}/\sqrt{s})$	$<$	1.020	0.980	1.030	1.030
$\alpha_{\tau^+\tau^-}$ (rad)	$>$	2.600	2.500	2.480	2.320
$M_{q\bar{q}}^{raw}$ (GeV)	$\in$	[64.,112.]	[62.,112.]	[60.,115.]	[58.,112.]
$M_{q\bar{q}}^{4C} + M_{\tau^+\tau^-}^{4C}$ (GeV)	$>$	174.0	166.0	162.0	175.0

Table 5.5: Cuts applied for selecting $ZZ \to q\bar{q}\tau^+\tau^-$ events at different $\sqrt{s}$.

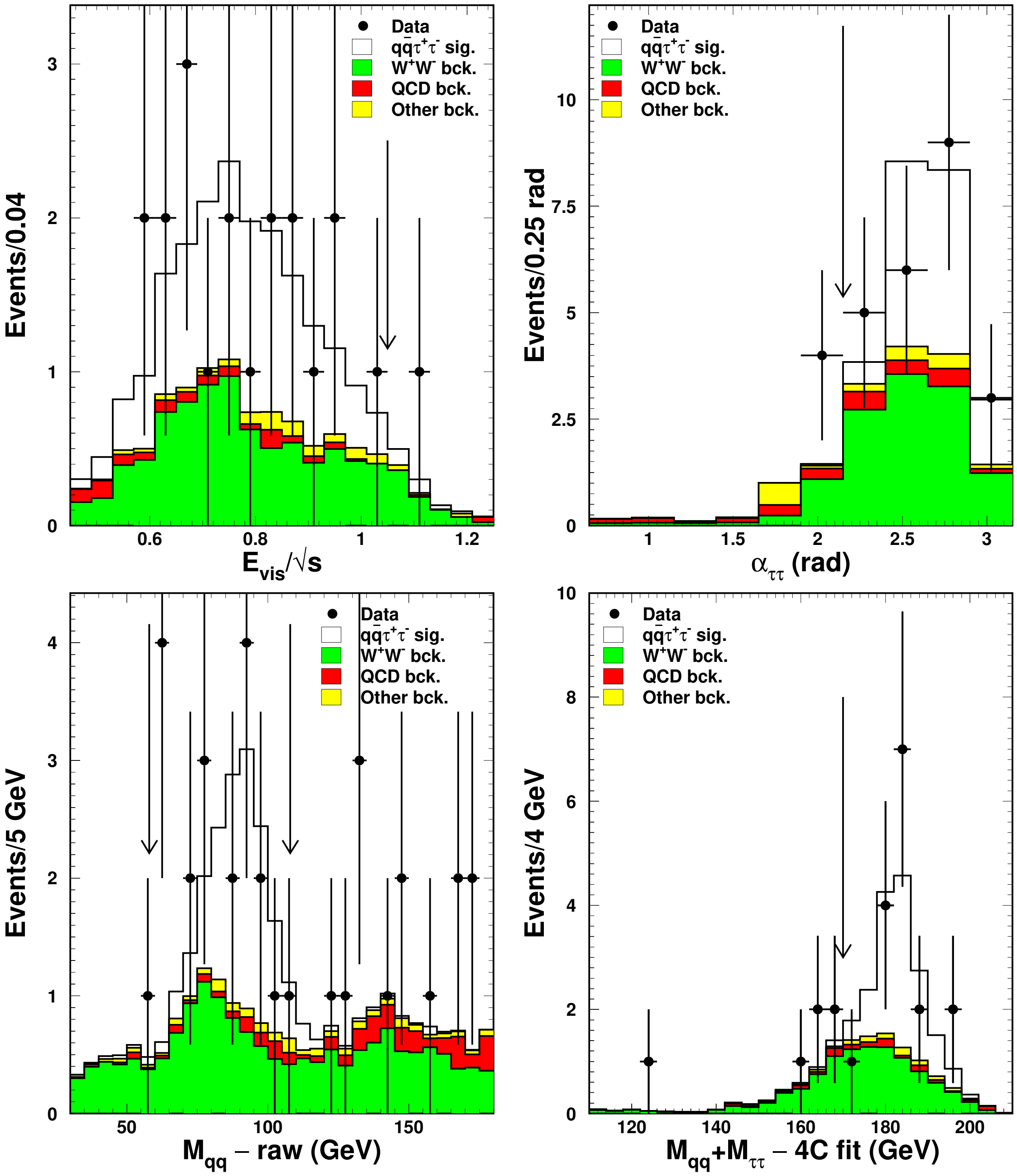

Figure 5.13: (N-1) plots of the selection variables used for selecting $q\bar{q}\tau^+\tau^-$ events: (a) Normalised visible energy, (b) Opening angle between two τ's in Z rest-frame, (c) Raw hadronic mass, and (d) Sum of di-jet and di-tau masses after kinematic fit.

5.4.4 Selection Performance

Selection performance is summarised in Table 5.6 with a detailed account of overall selection efficiency for all three sub-channels, purity of the signal sample, expected number of signal, backgrounds events and observed number of data events. In total, we select 71 candidates in data in comparison to 63 events expected from simulation (N_{signal}=50, $N_{background}$=13). By suitably choosing the selection variables and by properly retuning

$<\sqrt{s}>$ (GeV)	Final state	Selection efficiency (%)			Purity (%)	N_{signal}	$N_{background}$	N_{data}
		$\epsilon_{q\bar{q}e^+e^-}$	$\epsilon_{q\bar{q}\mu^+\mu^-}$	$\epsilon_{q\bar{q}\tau^+\tau^-}$				
183	$q\bar{q}e^+e^-$	75.5	–	–	88.5	0.77±0.04	0.10±0.03	2.00
	$q\bar{q}\mu^+\mu^-$	–	59.4	–	86.2	0.44±0.01	0.07±0.01	0.00
	$q\bar{q}\tau^+\tau^-$	2.1	5.7	25.6	49.0	0.25±0.02	0.26±0.03	1.00
189	$q\bar{q}e^+e^-$	75.4	–	–	93.5	4.76±0.13	0.33±0.06	8.00
	$q\bar{q}\mu^+\mu^-$	–	62.1	0.2	91.0	3.64±0.08	0.36±0.05	3.00
	$q\bar{q}\tau^+\tau^-$	0.2	5.9	27.7	48.3	2.01±0.08	2.15±0.14	4.00
192	$q\bar{q}e^+e^-$	72.1	–	–	96.9	0.94±0.03	0.03±0.01	1.00
	$q\bar{q}\mu^+\mu^-$	–	60.2	0.2	93.3	0.70±0.01	0.05±0.01	1.00
	$q\bar{q}\tau^+\tau^-$	1.1	8.3	31.6	50.5	0.46±0.02	0.45±0.03	0.00
196	$q\bar{q}e^+e^-$	74.6	–	–	89.8	2.81±0.09	0.32±0.14	4.00
	$q\bar{q}\mu^+\mu^-$	–	61.3	0.1	90.2	2.21±0.04	0.24±0.08	3.00
	$q\bar{q}\tau^+\tau^-$	1.8	8.8	31.9	50.3	1.52±0.05	1.50±0.10	3.00
200	$q\bar{q}e^+e^-$	73.5	–	–	91.5	2.90±0.09	0.27±0.06	5.00
	$q\bar{q}\mu^+\mu^-$	–	59.8	0.5	92.8	2.32±0.04	0.18±0.02	4.00
	$q\bar{q}\tau^+\tau^-$	1.3	5.6	28.4	53.8	1.39±0.05	1.19±0.07	1.00
202	$q\bar{q}e^+e^-$	68.6	–	–	77.6	1.35±0.04	0.39±0.22	1.00
	$q\bar{q}\mu^+\mu^-$	–	59.9	0.3	93.5	1.15±0.02	0.08±0.01	1.00
	$q\bar{q}\tau^+\tau^-$	3.8	4.5	27.7	54.2	0.65±0.02	0.55±0.03	1.00
205	$q\bar{q}e^+e^-$	73.5	–	–	90.1	3.19±0.04	0.35±0.04	4.00
	$q\bar{q}\mu^+\mu^-$	–	61.2	0.3	89.2	2.39±0.04	0.29±0.03	2.00
	$q\bar{q}\tau^+\tau^-$	2.8	4.8	27.5	57.6	1.40±0.06	1.03±0.06	4.00
207	$q\bar{q}e^+e^-$	74.2	–	–	90.3	5.60±0.04	0.60±0.06	9.00
	$q\bar{q}\mu^+\mu^-$	–	59.9	0.3	89.9	4.27±0.02	0.48±0.05	4.00
	$q\bar{q}\tau^+\tau^-$	2.1	4.8	28.3	58.3	2.49±0.02	1.78±0.11	5.00
					Total	49.61±0.26	13.05±0.38	71.00

Table 5.6: Summary of selection performance in terms of overall signal efficiency, purity of the signal sample, expected signal, background and observed data events. Uncertainties on the signal and background expectations, due to finite Monte Carlo size, are also given.

them to take into account the change in signal topology, we have been able to keep the selection efficiency almost unchanged with $\sqrt{s}$ for all the three sub-channels. The average efficiencies are estimated to be 74%, 61% and 36% for the $q\bar{q}e^+e^-$, $q\bar{q}\mu^+\mu^-$ and

$q\bar{q}\tau^+\tau^-$ sub-channels respectively. Cross efficiencies among different channels are found to be negligible, only exception being the $q\bar{q}\tau^+\tau^-$ final state. In this case, other two sub-channels have got reasonable cross contributions due to their identical final state with the $q\bar{q}\tau^+\tau^-$ sub-channel when both the taus decay leptonically.

The detailed break up of the background content is given in Table 5.7. As it is seen, contribution from W-pair is the most dominant one, while QCD and non-resonant four fermion processes play secondary role. The major source of the backgrounds, W^+W^-, is

W^+W^-		QCD	Non-reso	Others
$q\bar{q}'\ell\nu$	$q\bar{q}'q'\bar{q}$	process	4-fermion	process
55.4%	9.9%	16.8%	16.4%	1.5%

Table 5.7: Percentile break up of the background content.

mostly constituted by the semileptonic final states. It should be further noted here that among the three sub-channels, the $q\bar{q}\tau^+\tau^-$ accounts for largest background contamination.

References

[1] Y. Karyotakis and M. Wadhwa, L3 Internal Note # 1727 (1995).

[2] O. Adriani *et al.*, Nucl. Inst. Meth. **A302** (1991) 53.

[3] H.J. Behrend *et al.*, Phys. Lett. **B110** (1982) 329.

[4] C. Caso *et al.*, *Review of Particle Physics*, Eur. Phy. J. **C3** (1998) 1.

[5] S. Catani *et al.*, Phys. Lett. **B269** (1991) 432;
S. Bethke *et al.*, Nucl. Phys. **B370** (1992) 310.

[6] S. Banerjee *et al.*, L3 Internal Note # 1947 (1996).

[7] G. Mohanty, *Measurement of* ZZ *cross section from '99 data*, Talk given at L3 General Meeting, CERN, Switzerland, June 2000;
G. Mohanty, *Status of* ZZ *analysis on Y2K data*, Talk given at L3 Analysis Workshop, BalatonFüred, Hungary, June 2001;
T. Aziz and G. Mohanty, L3 Internal Note # 2726 (2002).

[8] For minimisation purpose, MINUIT version 94.1 is used:
F. James and M. Roos, Comp. Phys. Comm. **10** (1975) 343.

[9] T. Aziz and G. Mohanty, L3 Internal Note # 2606 (2000).

Chapter 6

Measurement of the Cross Section

This chapter describes the measurement of the cross section for the process, $e^+e^- \to ZZ \to q\bar{q}\ell^+\ell^-$ as well as for the full process, $e^+e^- \to ZZ$. Towards the end of the chapter, study of the inclusive $b\bar{b}$ final state is also discussed.

6.1 The $e^+e^- \to ZZ \to q\bar{q}\ell^+\ell^-$ Cross Section

The selected number of $e^+e^- \to ZZ \to q\bar{q}\ell^+\ell^-$ events in data, N_{obs}, can be translated into the measured cross section, σ, and the statistical error on it, $\Delta\sigma$, for the process by using the following equation:

$$\sigma \;=\; \frac{N_{obs} - N_{bkg}}{\epsilon_{sig} \cdot \mathcal{L}_{int}}, \quad \text{and } \Delta\sigma \;=\; \frac{\sqrt{N_{obs}}}{\epsilon_{sig} \cdot \mathcal{L}_{int}}. \tag{6.1}$$

Here N_{bkg} is the expected background, ϵ_{sig} is the overall signal efficiency, both estimated from high statistics Monte Carlo samples, and $\mathcal{L}_{int}$ is the total integrated luminosity. However, there is a subtle problem on using the event-counting method as described in Equation 6.1, because one tends to overestimate the statistical error on the measured cross section due to low statistics (small N_{obs}) associated with the considered process. Instead, we fit the most discriminative variable, equal mass spectrum, to a maximum binned log-likelihood function [1]:

$$-2 \cdot \log(\text{likelihood}) \;=\; -2 \cdot \sum_{i=1}^{N_{bin}} (n_i \cdot \log\, \mu_i - \mu_i + \log\, n_i!) \text{ with } \mu_i = X \cdot s_i + b_i \tag{6.2}$$

to extract the cross section. Here N_{bin} is the total number of bin, n_i, s_i and b_i are the number of data, signal and background events in i-th bin respectively and X is the ratio of the measured cross section to the Standard Model value. In case a zero value of X is contained within 1σ confidence interval around the maximum of the log-likelihood function, we calculate a 95% C.L. upper limit on the cross section. Otherwise the value of X at the maximum is quoted as the measured cross section with the 1σ interval as the statistical error on it.

Figure 6.1 shows the distribution of the equal mass spectrum integrated over the full data sample along with measured cross section ratio, X. We find decent agreement with

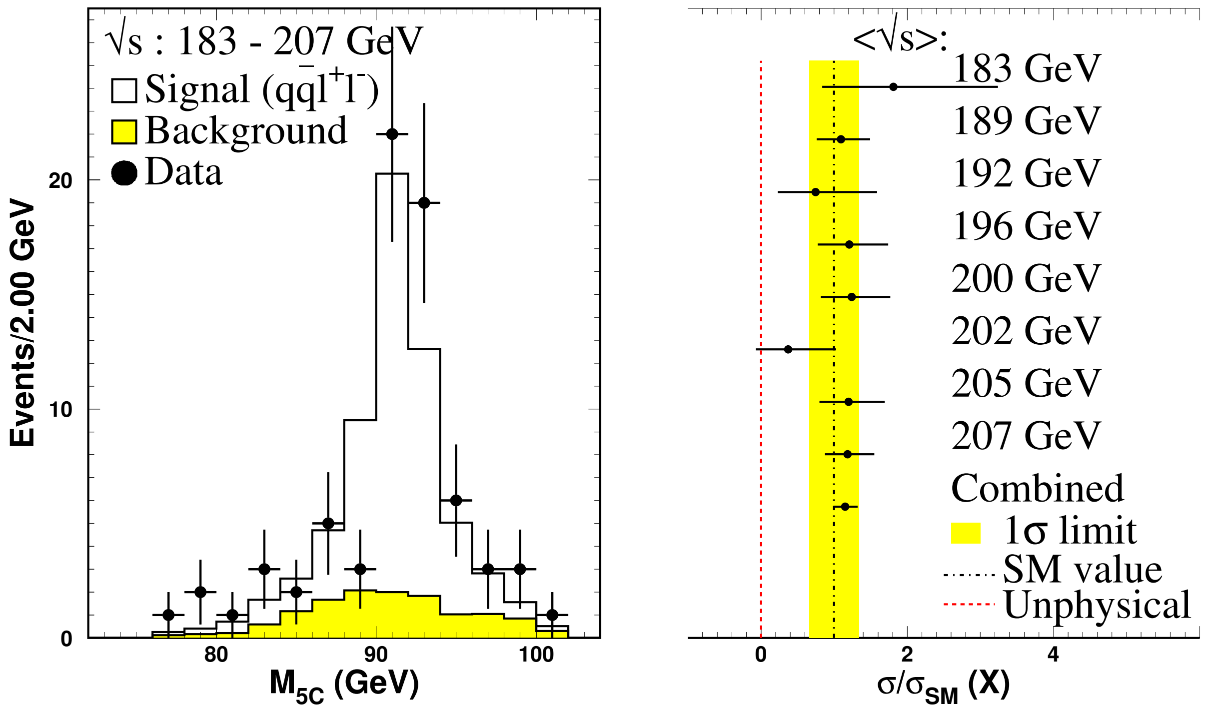

Figure 6.1: (a) Distribution of the equal mass spectrum, the final variable used for extracting the $e^+e^- \rightarrow ZZ \rightarrow q\bar{q}\ell^+\ell^-$ cross section, and (b) measured values of (σ/σ_{SM}) at different $\sqrt{s}$. We quote a 95% C.L. upper limit for $\sqrt{s} = 192$ and 202 GeV.

the Standard Model expectation both for the mass distribution as well as cross section.

6.2 Study of Systematic Errors

There are several sources of systematic error in the cross section measurement. The ones studied here are :

1. Selection Criteria
2. Background Normalisation
3. Uncertainty on Energy Scale
4. Lepton Identification
5. Monte Carlo Statistics

We have taken care of all these sources for the data collected at $\sqrt{s} = 192 - 207$ GeV during year 1999 and 2000, of a total integrated luminosity of 450 pb^{-1}. For the earlier data samples, systematic error due to finite Monte Carlo statistics is calculated while for the remaining sources we have simply migrated the percentile error as calculated later. It should be made clear, however, that in our case the total error is dominated by the statistical part ($\Delta^{stat} \simeq 20\%\ \sigma$) with systematic error having less significant role to play.

6.2.1 Selection Criteria

The variation of the measured cross section with selection cuts gives a measure of the systematic effect due to selection criteria. The systematic error S and the statistical error on it, ΔS are defined as:

$$\mathrm{S} = \frac{(\sigma_0 - \sigma_i)}{\sigma_0} \tag{6.3}$$

$$\Delta\mathrm{S} = \Delta\left(\frac{\sigma_i}{\sigma_0}\right) = \left(\frac{\sigma_i}{\sigma_0}\right) \cdot \sqrt{\left(\frac{\Delta\sigma_i}{\sigma_i}\right)^2 + \left(\frac{\Delta\sigma_0}{\sigma_0}\right)^2} \tag{6.4}$$

where σ_0 is the measured cross section when all the cuts are at their nominal positions and σ_i is the cross section when the cut being investigated is at its i-th position while all other cuts are at their nominal values and $\Delta\sigma_{0(i)}$ are the statistical error on those quantities. The range of variation of the cut position is chosen close to the detector resolution for that quantity. The error due to a cut is then the weighted average of |S| for the various cut positions. Figure 6.2 shows the variation of S as a function of cut position of the selection variables.

Final state	Selection variables	Error S(%)	Weight (%)	Total S(%)
$\mathrm{q\bar{q}e^+e^-}$	$(\mathrm{E_\perp/E_{vis}})$	0.90	39.6	4.46
	$(\mathrm{E_{e1} + E_{e2}})/\sqrt{\mathrm{s}}$	1.32		
	Energy Variable	4.70		
	$\mathrm{M^{4C}_{q\bar{q}} + M^{4C}_{e^+e^-}}$	1.12		
$\mathrm{q\bar{q}}\mu^+\mu^-$	$(\mathrm{E}_{\mu 2}/\sqrt{\mathrm{s}})$	0.86	49.1	
	$\mathrm{M^{4C}_{q\bar{q}}} + \mathrm{M^{4C}_{\mu^+\mu^-}}$	0.73		
$\mathrm{q\bar{q}}\tau^+\tau^-$	$(\mathrm{E_{vis}}/\sqrt{s})$	2.15	11.3	
	$\alpha_{\tau^+\tau^-}$	15.47		
	$\mathrm{M^{raw}_{q\bar{q}}}$ - Low	3.24		
	$\mathrm{M^{raw}_{q\bar{q}}}$ - High	1.63		
	$\mathrm{M^{4C}_{q\bar{q}}} + \mathrm{M^{4C}_{\tau^+\tau^-}}$	4.69		

Table 6.1: Channel wise break up of the systematic error due to selection criteria

The systematic error due to selection criteria is performed in two steps. First we compute the systematics due to selection of each of the three sub-channels ($\mathrm{q\bar{q}e^+e^-}$, $\mathrm{q\bar{q}}\mu^+\mu^-$ and $\mathrm{q\bar{q}}\tau^+\tau^-$) independently. This is done by adding the errors due to all selection

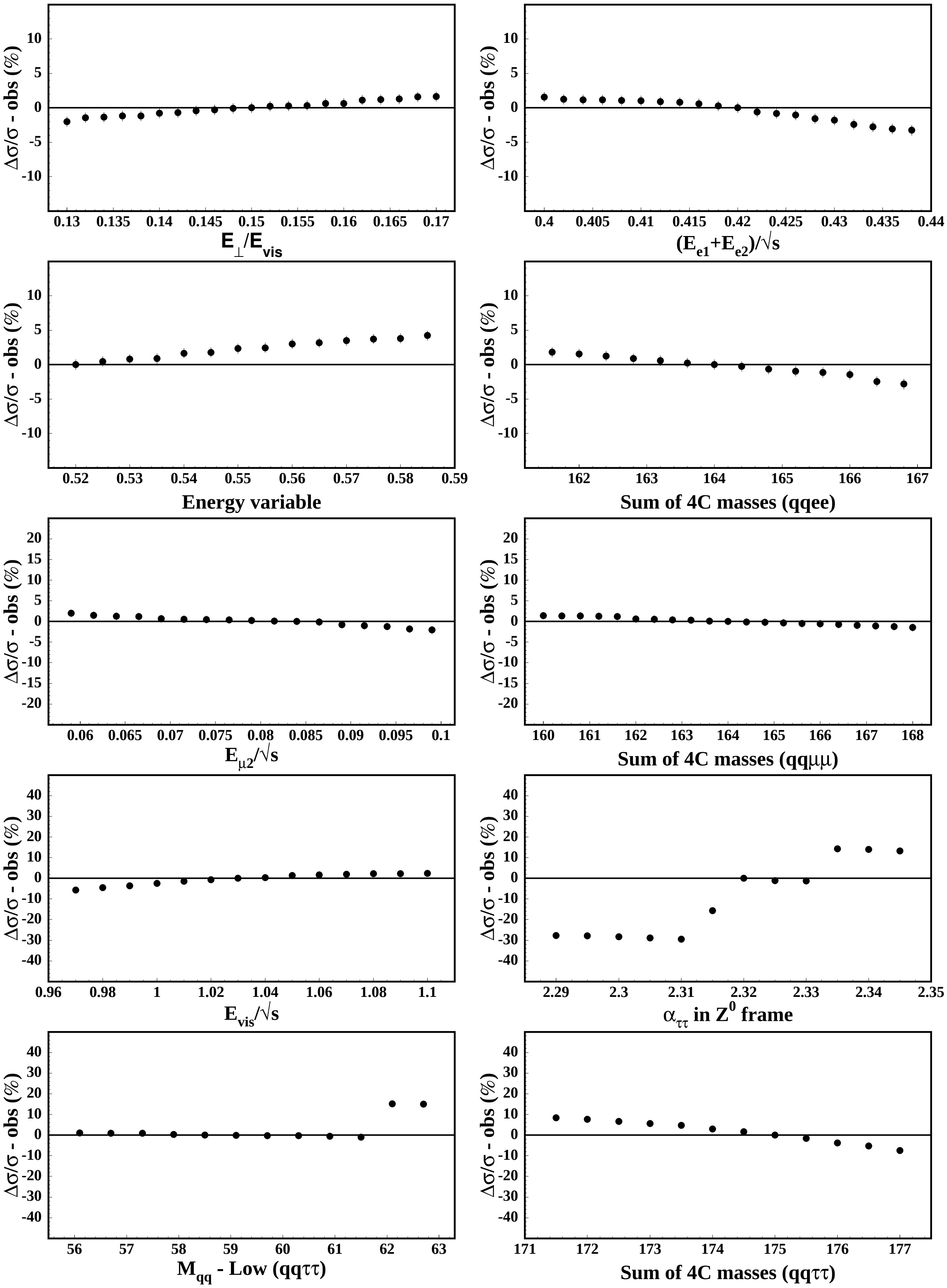

Figure 6.2: Change in cross section w.r.t. change in cut position of the selection variables.

variables for the respective sub-channels in quadrature after subtracting the statistical part in quadrature. Finally we take the weighted average with weight $\propto \frac{1}{\Delta_i^2}$ to get the final number (here Δ_i corresponds to the contribution of i-th sub-channel to the total statistical error). Table 6.1 summarises the channel wise break up of the systematic error which is estimated to be 4.46%.

6.2.2 Background Normalisation

Our selection algorithm also selects a few background events along with the signal events. The contribution from these backgrounds is estimated using various Monte Carlo samples. Any possible uncertainties on the background cross section will modify the shape of the final distribution used for extracting the signal cross section and hence, will contribute to the overall systematic error.

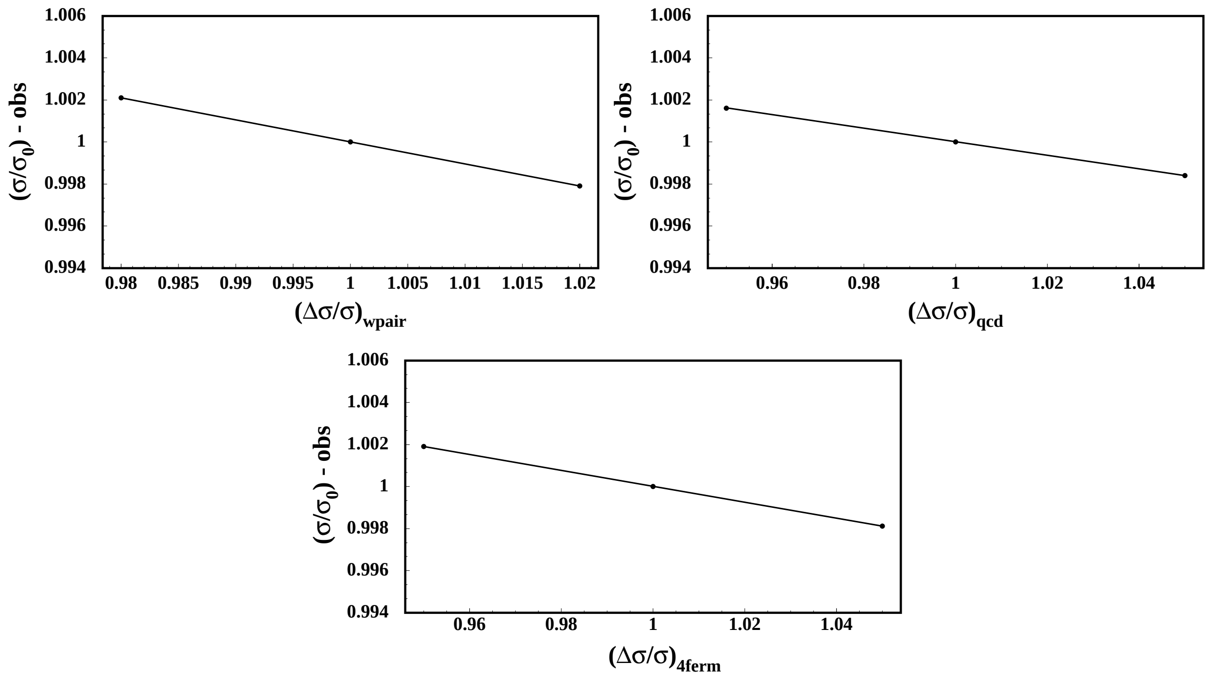

Figure 6.3: The distribution of (σ/σ_0) as a function of the cross section for different background processes.

To estimate this effect, we vary the cross section of all the contributing background processes in a reasonable range as agreed upon by four LEP experiments and re-fit the final mass distribution to extract the signal cross section. The slope in the distribution of the relative change in the observed cross section, $(\frac{\sigma}{\sigma_0})$, is attributed to the systematic error. Figure 6.3 shows the distribution of $(\frac{\sigma}{\sigma_0})$ as a function of the cross section for the different background processes. The total systematic error due to uncertainty on the background cross section is estimated to be 0.32% as summarised in Table 6.2.

Background process	Variation of cross section	$\delta\sigma/\sigma$ (%)
$e^+e^- \to W^+W^-$	2%	0.21
$e^+e^- \to q\bar{q}$ (QCD)	5%	0.16
Non-reso 4fermion	5%	0.19
	Total	0.32

Table 6.2: Systematic contribution from background normalisation

6.2.3 Uncertainty on Energy Scale

Inter-calibration mismatch among different parts of the detector leads to uncertainty on the absolute scale of the measured jet energy. This may affect our measurement, since the final state we are interested in, also involves hadronic jets. To quantify this effect, we scale up and down the measured jet energies by 2% and see the relative change in the measured cross section (Figure 6.4). The maximal relative change with respect to

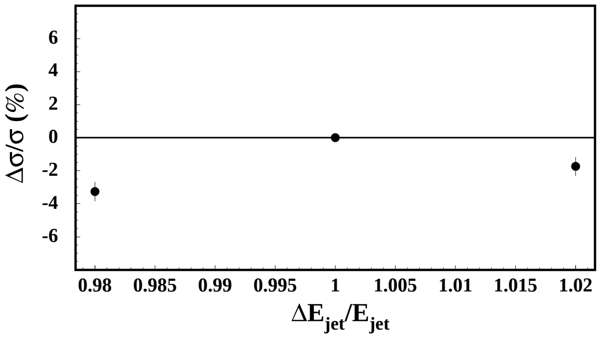

Figure 6.4: Distribution of $(\Delta\sigma/\sigma)$ as a function of the jet energy.

the nominal value, module statistical uncertainty on the cross section, is quoted as the systematic error due to energy scale. In our case, it is found out to be 1.6%.

6.2.4 Lepton Identification

Since lepton identification forms one of the crucial elements of this analysis, we need to study possible systematic contribution due to the adopted identification method. The study is carried out in two steps. Firstly, the maximal difference in the shape of the expected (Monte Carlo) and observed (data) distribution of a lepton identifying variable around the nominal cut value is attributed as the systematic error due to the said variable. Figure 6.5 shows the relative change in the number of expected and observed events around the nominal cut position for the lepton identifying variables. For each lepton class $(e/\mu/\tau)$, we calculate the systematics error by adding the contributions from different lepton identifying variables in quadrature. The total error is then, the weighted average

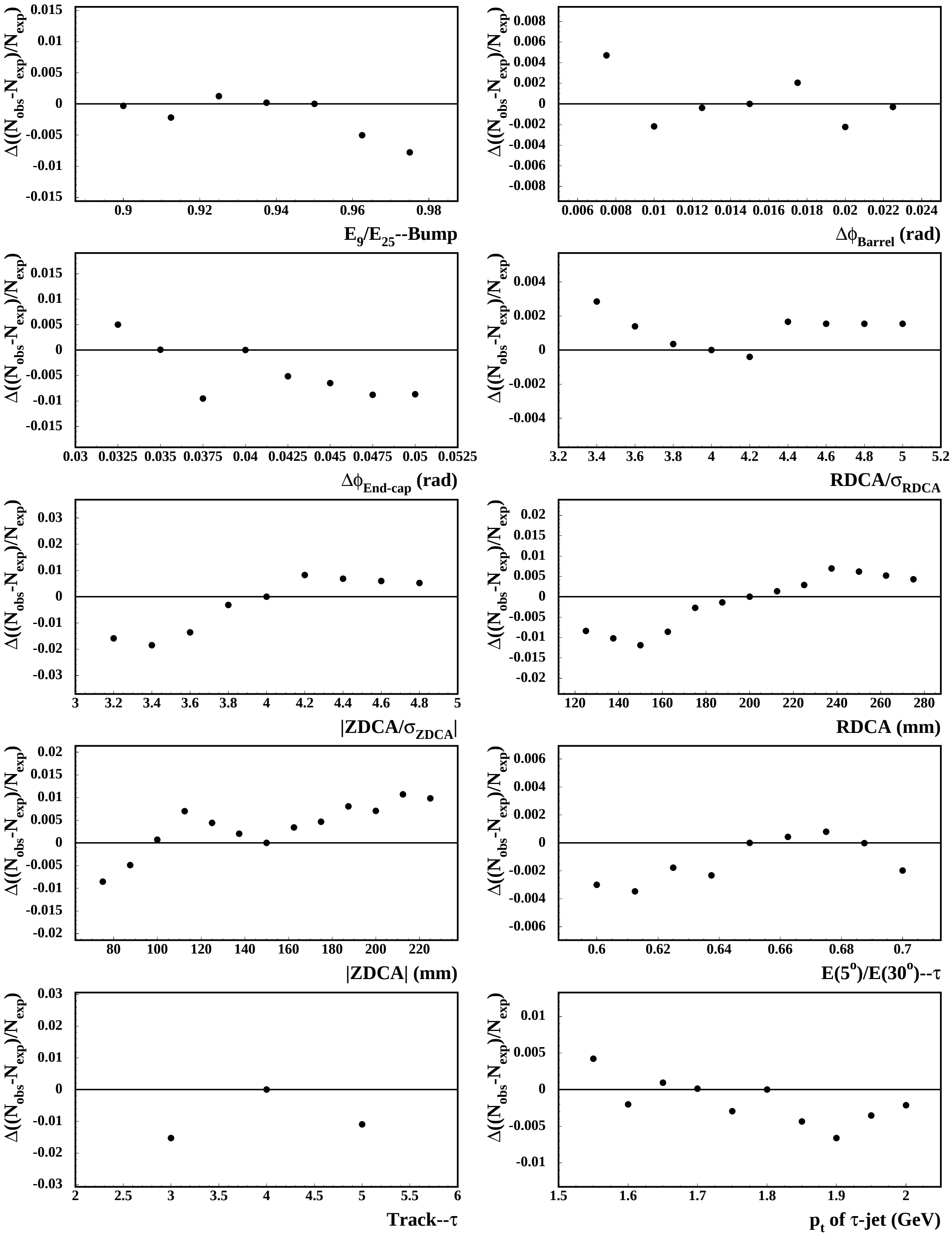

Figure 6.5: Relative change in number of expected and observed events w.r.t. change in the cut position for the lepton identifying variables. Here RDCA and ZDCA refer to the DCAs in $r\phi$ and rz planes respectively.

Lepton Type	Lepton ID variables	Error (%)	Reconstruction Efficiency(%)	Total (%)
Electron	$(\frac{E_9}{E_{25}})$	0.8	82.9	1.8
	$(\Delta\Phi)_{\rm Barrel}$	0.5		
	$(\Delta\Phi)_{\rm Endcap}$	0.9		
Muon	$(\frac{\rm DCA}{\sigma_{\rm DCA}})_\phi$	0.3	64.3	
	$\lvert(\frac{\rm DCA}{\sigma_{\rm DCA}})_{\rm z}\rvert$	1.8		
	$\rm DCA_\phi$	1.2		
	$\lvert(\rm DCA_z)\rvert$	1.1		
	(E_{15}/E)	0.9		
Tau	(E_5/E_{30})	0.3	56.0	
	# Track	1.5		
	$\rm p_T^{max}$ (GeV)	0.7		

Table 6.3: Systematic contribution from various lepton identifying variables

of the error due to each lepton class (weight $\Rightarrow$ reconstruction efficiency). Table 6.3 summarises the detailed break up of the systematic error due to lepton identification, which is estimated to be 1.8%.

6.2.5 Monte Carlo Statistics

We estimate the selection efficiencies both for signal and background processes from high statistics Monte Carlo samples. However, those samples being of finite size introduce uncertainties on the efficiency of the respective processes. The uncertainty on the expected number of events for i-th process, $\Delta \mathrm{N}_i$, (calculated using Binomial distribution) [2] and the total error due to finite MC size, S, are defined as:

$$\Delta \mathrm{N}_i = \sigma_i \cdot \mathcal{L}_{\rm int} \cdot \Delta\epsilon_i = \sigma_i \cdot \mathcal{L}_{\rm int} \cdot \sqrt{\frac{\epsilon_i(1-\epsilon_i)}{\mathrm{G}_i}} \tag{6.5}$$

$$\mathrm{S} = \frac{\sqrt{\sum_{i=1}^{n}(\Delta \mathrm{N}_i)^2}}{\sum_{i=1}^{n}\mathrm{N}_i} \text{ with } \mathrm{N}_i = \sigma_i \cdot \mathcal{L}_{\rm int} \cdot \epsilon_i \tag{6.6}$$

where ϵ_i, G_i and σ_i are the selection efficiency, number of generated events and cross section for i-th process and n is the total number of processes including the signal process. In Table 6.4, we summarise year wise systematics contribution due to finite MC size.

6.3 Final Results

The measured cross section for the process, $\mathrm{e^+e^-} \rightarrow \mathrm{ZZ} \rightarrow \mathrm{q\bar{q}}\ell^+\ell^-$, along with the errors are given in Table 6.5. Figure 6.6 shows the variation of the measured cross sections as a function of centre-of-mass energy together with the expectation from the Standard

Year	S (%)	Year	S (%)
1997	3.37	1998	1.79
1999	1.49	2000	0.75

Table 6.4: Systematics due to finite Monte Carlo statistics

$<\sqrt{s}>$ (GeV)	$\sigma(e^+e^- \to ZZ \to q\bar{q}\ell^+\ell^-)$ (pb)	σ_{SM} (pb)
182.7	$0.0786^{+0.0622}_{-0.0422} \pm 0.0031$	0.043
188.7	$0.1120^{+0.0408}_{-0.0340} \pm 0.0067$	0.103
194.5	$0.1475^{+0.0585}_{-0.0481} \pm 0.0086$	0.134
200.2	$0.1437^{+0.0601}_{-0.0495} \pm 0.0097$	0.151
204.8	$0.1895^{+0.0784}_{-0.0630} \pm 0.0100$	0.158
206.8	$0.1896^{+0.0584}_{-0.0496} \pm 0.0101$	0.160

Table 6.5: Measured cross sections for the process $e^+e^- \to ZZ \to q\bar{q}\ell^+\ell^-$ along with the SM predictions. Errors given in the measurement are respectively statistical and systematic.

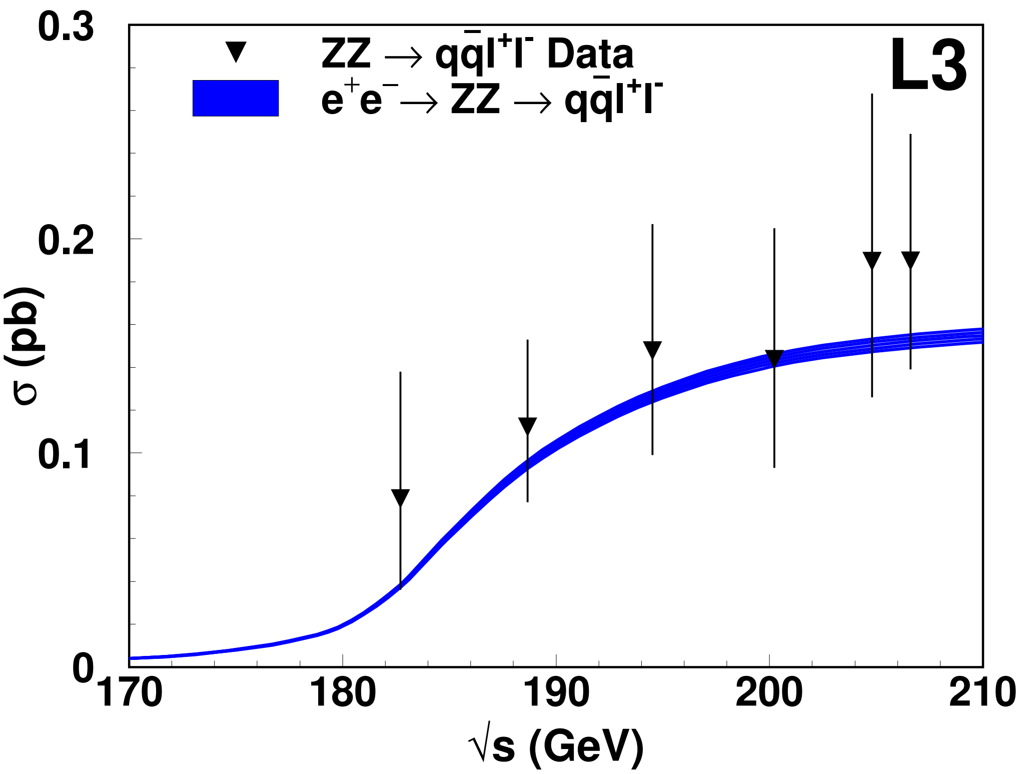

Figure 6.6: Standard Model prediction for the $e^+e^- \to ZZ \to q\bar{q}\ell^+\ell^-$ and the corresponding measurement. A 2% theoretical uncertainty is assigned to the prediction.

Model. Due to very low statistics at $\sqrt{s} = 192$ and $202\,\mathrm{GeV}$ leading to 95% C.L. upper limit on the cross section, we have added those to the nearest energy points *i.e.* 196 and 200 GeV respectively. We find reasonable agreement between our measurement [3] and the Standard Model prediction.

6.4 The $e^+e^- \to ZZ$ Cross Section

A global likelihood fit is performed to the final variables of all the visible final states emerging out of the process, $e^+e^- \to ZZ$, in order to extract the cross section for the process. The result [4] is found to be in good agreement with the Standard Model prediction, as shown in Figure 6.7.

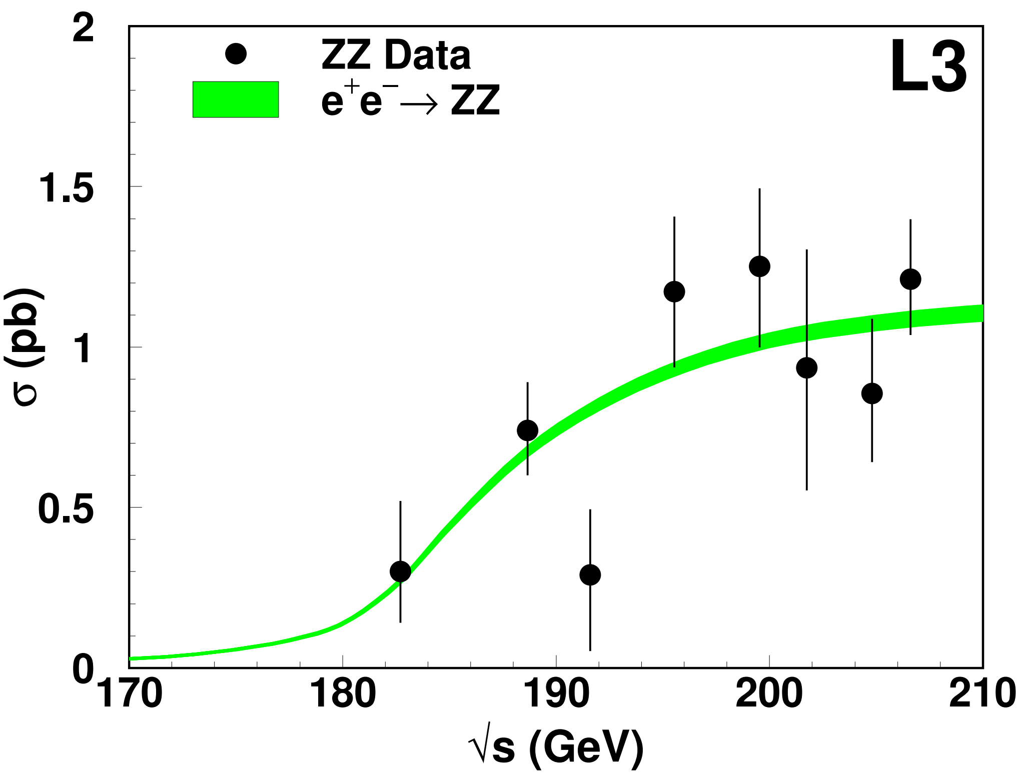

Figure 6.7: Standard Model prediction for the $e^+e^- \to ZZ$ cross section and the corresponding measurement. A 2% theoretical uncertainty is assigned to the prediction.

6.5 Study of Inclusive $b\bar{b}$ Final State

At LEP energies, the Standard Model Higgs boson is expected to be produced mainly via Higgsstrahlung process [5], $e^+e^- \to HZ$, as shown in Figure 6.8(a). Small additional contributions are expected from the t-channel W/Z boson fusion diagrams (Figure 6.8(b)),

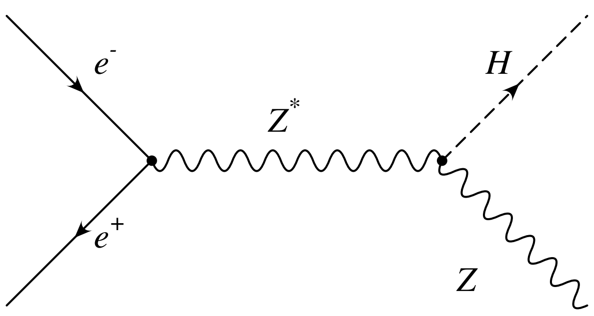

(a) Higgsstrahlung diagram.

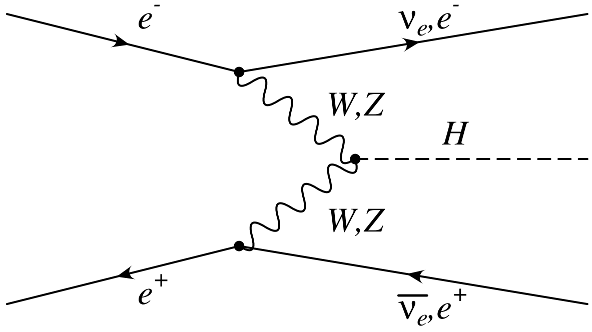

(b) Vector boson fusion diagram.

Figure 6.8: Standard Model Higgs production processes at LEP.

which produce a Higgs boson along with either a pair of neutrinos or electrons. For masses in the vicinity of 115 GeV (kinematic limit for Higgsstrahlung diagram at $\sqrt{s} \approx 206$ GeV), the SM Higgs boson decays mainly to $b\bar{b}$ (74%), while decays to $\tau^+\tau^-$, $WW^\star$, gluon pairs and $c\bar{c}$ are all less important (Figure 6.9). Thus $HZ \to b\bar{b}X$ constitutes the major final state topology via which an intermediate-mass Higgs ($m_H \lesssim 140$ GeV) could be detected. Here X represents different decay channels of the Z boson; $q\bar{q}$, $\ell^+\ell^-$ or $\nu\bar{\nu}$. This process has final state same as the ZZ process, where one of the Z's decays to $b\bar{b}$. Thus the process, $ZZ \to b\bar{b}X$, should be closely investigated as the major background for the Higgs production at LEP. Moreover, it tests the detector capability to discover Higgs as these two processes have similar, and non-interfering scattering amplitudes [5, 6]. In other word, if one finds significant enhancement on the measured $ZZ \to b\bar{b}X$ cross section over the SM value, one has to closely look at the result from direct Higgs search. Having justified the importance of the inclusive $b\bar{b}X$ final state, we now turn to the corresponding measurements.

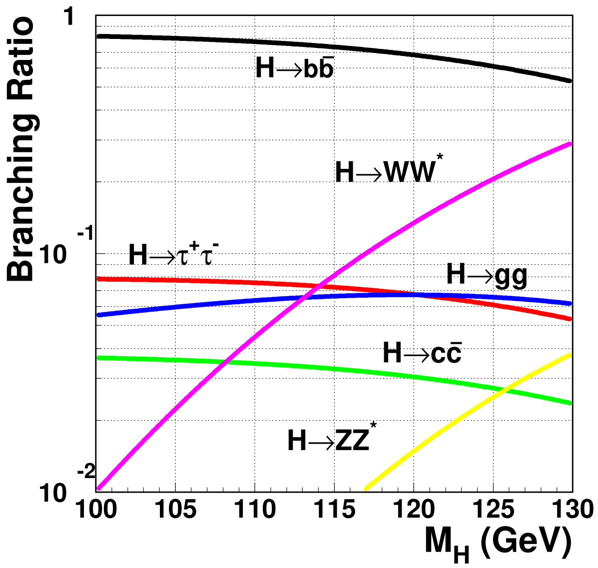

Figure 6.9: The SM Higgs decay branching ratios.

6.5.1 The $e^+e^- \to ZZ \to b\bar{b}\ell^+\ell^-$ Cross Section

For studying the $b\bar{b}\ell^+\ell^-$ or in general $b\bar{b}X$ final state, identification of b-jet or "B-tagging" is very important. B-tagging is mainly based on the lifetime information of the hadronic jets. The typical lifetime of the hadrons with b-quark as one of the constituents, is about

1.5×10^{-12} s [7]. Hadrons without b-quark live either shorter (c-hadrons $\approx 0.5\times10^{-12}$ s), or longer (uds-hadrons $> 10^{-8}$ s). The latter decay far away from the interaction point. Apart from the lifetime, there are other variables which can be used to distinguish b-hadrons from others. Those are charged particle multiplicity and the jet mass at the decay point, tertiary decay vertices from cascade decays, difference in jet shape and prompt leptons from the semileptonic b decays. The L3 b-tagging technique [8] takes into account all these characteristics of the jet while computing the jet b-tag or simply the jet-tag. Figure 6.10 shows the neural network jet-tag output for the calibration data taken at the Z-peak in 1997. Measurement of the $e^+e^- \rightarrow ZZ \rightarrow b\bar{b}\ell^+\ell^-$ cross section is performed in several steps. First we compute the jet-tag for the two hadronic jets in the selected sample of $e^+e^- \rightarrow ZZ \rightarrow q\bar{q}\ell^+\ell^-$ events. The mass information is combined with the jet-tags to build the final $b\bar{b}\ell^+\ell^-$ discriminant [9]. For that, first the equal mass and the b-tag of the two jets are mapped to achieve uniform distribution for the background. Then the product of their observed values is calculated event-by-event basis. Finally the confidence level is computed for the product of three uniformly distributed quantities to be less than the observed product. This confidence level is expected to be low for the signal and flat for the background. The final discriminant is the negative logarithm of this confidence level. Figure 6.11 show the distributions of the equal mass spectrum, b-tag of the two jets, and the final discriminant for $b\bar{b}\ell^+\ell^-$ selection. The final discriminant is fitted to a binned log-likelihood function to calculate the $b\bar{b}\ell^+\ell^-$ cross section. Due to low statistics, the full data samples ($\sqrt{s} = 183 - 208\,\text{GeV}$) are added together to give a luminosity-averaged cross section value:

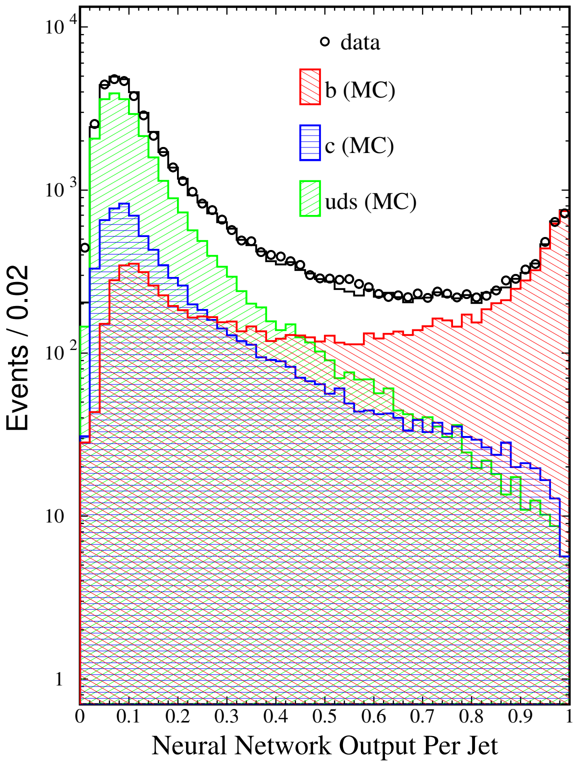

Figure 6.10: The neural network jet-tag output in 1997 Z-peak data and Monte Carlo.

$$\boxed{\sigma_{ZZ\,\rightarrow\, b\bar{b}\ell^+\ell^-}(<\sqrt{s}>= 196.7\text{ GeV}) = 0.034^{+0.015}_{-0.014} \pm 0.002\text{ pb},\ \sigma_{SM} = 0.027\text{ pb}}$$

The first error is the statistical component and the second one is due to systematic contribution. Here $<\sqrt{s}>$ refers to the luminosity averaged centre-of-mass energy.

6.5.2 The $e^+e^- \rightarrow ZZ \rightarrow b\bar{b}X$ Cross Section

Similar to the measurement of the $e^+e^- \rightarrow ZZ$ cross section, the final discriminant of $b\bar{b}\ell^+\ell^-$ final state is combined with that of the $b\bar{b}q\bar{q}$ and $b\bar{b}\nu\bar{\nu}$ final states through a

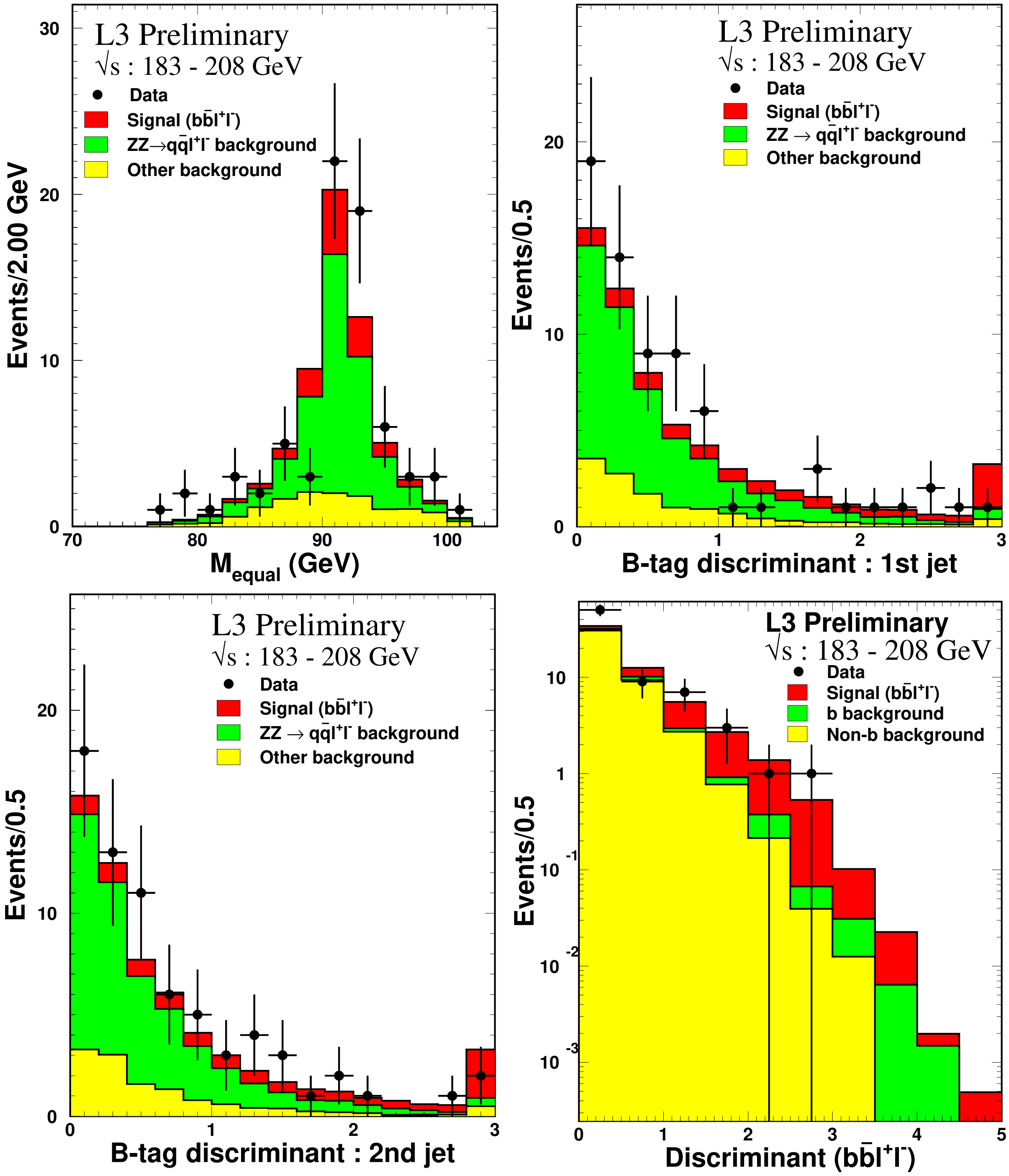

Figure 6.11: Distributions of the equal mass spectrum, b-tag of the two jets and the final discriminant for $b\bar{b}\ell^+\ell^-$ final state. Here all energy points are added together.

global likelihood. The global likelihood is fitted to calculate the $e^+e^- \to ZZ \to b\bar{b}X$ cross section, result of which is shown in Figure 6.12. The measurement is found to be in agreement with the $ZZ \to b\bar{b}X$ predictions [4], and the statistics is quite poor to say anything about Higgs production.

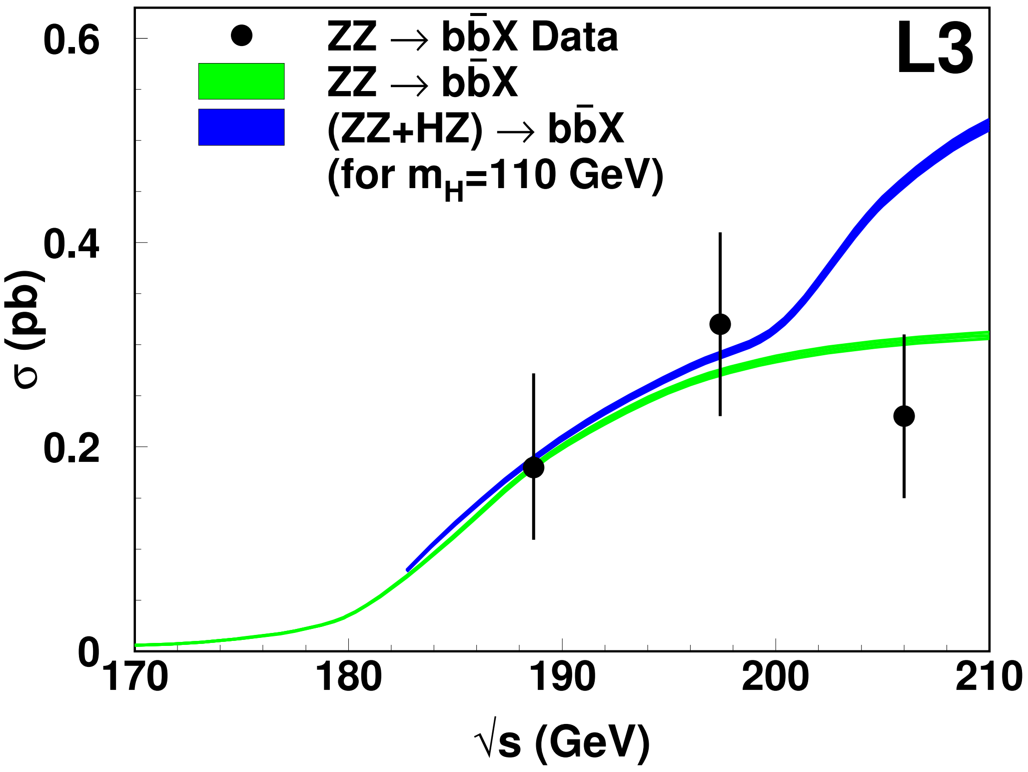

Figure 6.12: Standard Model prediction for the $e^+e^- \to ZZ \to b\bar{b}X$ cross section and the corresponding measurement. The combined prediction of HZ and ZZ processes leading to $b\bar{b}X$ final state is also given.

References

[1] W.T. Eadie *et al.*, *Statistical Methods in Experimental Physics*, North-Holland (1971);
L. Lyons, *Statistics for nuclear and particle physicists*, Cambridge Univ. Press (1986).

[2] G. D'Agostini, *Bayesian reasoning in High Energy Physics*, CERN 99-03, July 1999.

[3] T. Aziz and G. Mohanty, L3 Internal Note # 2726 (2002).

[4] L3 Collab., M. Acciarri *et al.*, Phys. Lett. **B450** (1999) 281;
L3 Collab., M. Acciarri *et al.*, Phys. Lett. **B465** (1999) 363;
L3 Collab., M. Acciarri *et al.*, Phys. Lett. **B497** (2001) 23;
G. Mohanty, L3 Internal Note # 2542l (2000);
Contributed to the 2002 summer conferences, L3 Internal Note # 2770 (2002).

[5] G. Altareli *et al.*, "Physics at LEP2", CERN 96-01, Volume 1.

[6] E. Boos *et al.*, Z. Phys. **C67** (1995) 613;
Marta Felcini, in *private communication.*

[7] C. Caso *et al.*, *Review of Particle Physics*, Eur. Phys. J. **C3** (1998) 1.

[8] J. Branson *et al.*, L3 Internal Note # 2108 (1997);
O. Adriani *et al.*, Phys. Lett. **B307** (1993) 237;
T. Aziz, PPE/L3 Note, May 7 (1992);
T. Aziz, *Measurement of R_b from hadronic decay of the* Z, Talk given at 5th International Symposium on Heavy Flavour Physics, July 1993.

[9] Chris Tully, L3 Internal Note # 2422ag (1999);
Chris Tully, in *private communication.*

Chapter 7

Search for Physics beyond Standard Model

In this chapter, we discuss how the selected sample of $e^+e^- \to ZZ \to q\bar{q}\ell^+\ell^-$ events is utilised to search for physics beyond Standard Model in the sector of anomalous gauge couplings and low scale gravity.

7.1 Anomalous Trilinear Gauge Couplings

As explained in Chapter 2, presence of anomalous couplings in Z-pair production [1] will basically lead to change in the measured cross section for the process and modification of the angular distribution of the Z. In principle, the angular variables inherit better sensitivity for the anomalous couplings as compared to other. It is, however, quite difficult to disentangle the anomalous effect from the usual SM expectation using these variables, due to large statistical uncertainties (see Figure 7.1). Thus we have concentrated on the measured cross section and have closely studied the equal mass spectrum, the variable used for calculating the cross section. Though the measured cross section also has large statistical error, it is comparatively better as it depends on the integral distribution unlike the angular variables. In what follows in this section, we are going to discuss how the effect of anomalous couplings are introduced to modify the mass distribution via reweighting method and the result on anomalous couplings obtained by a log-likelihood fit to the modified mass distribution.

7.1.1 Method of Reweighting

In order to take into account the anomalous effect with sufficient accuracy, the correct matrix elements have to be calculated for which one needs to generate large sample of Monte Carlo events with non-zero values of anomalous couplings. However, from practical point of view, this method is not quite convenient. Instead, a reweighting method is used for a single set of generated events to obtain the anomalous distribution. It is achieved

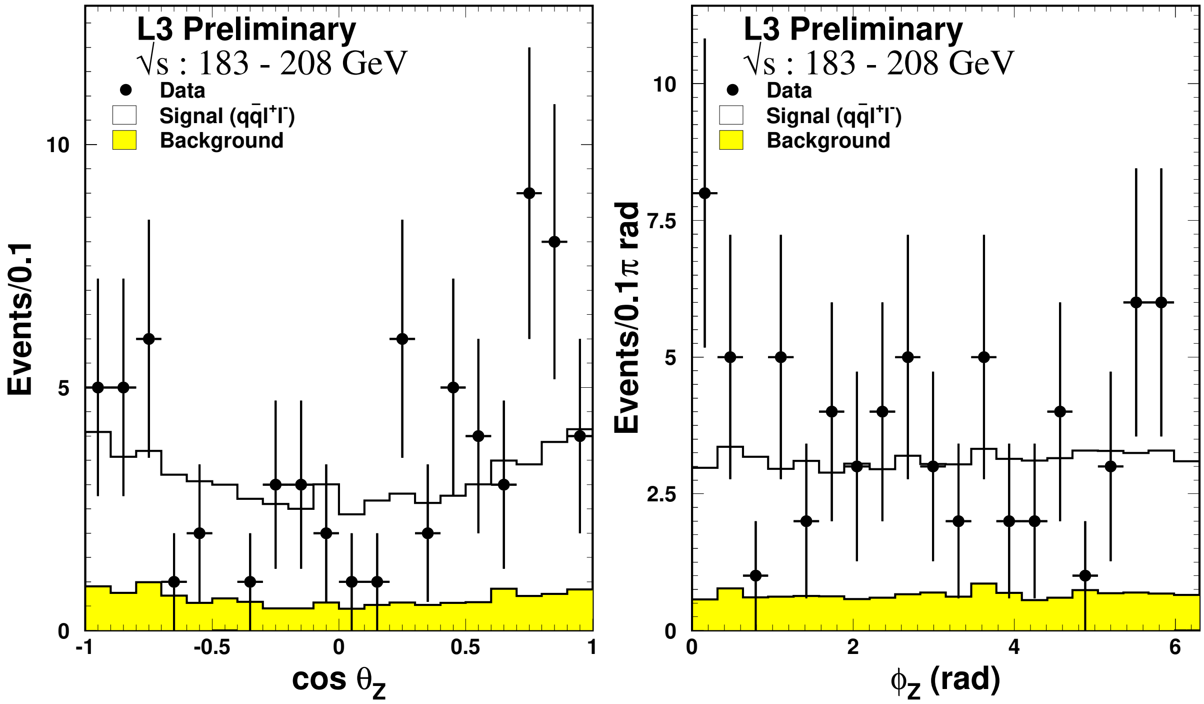

Figure 7.1: Angular distributions of the produced Z-boson; (a) $\cos\theta_{\mathrm{Z}}$, and (b) ϕ_{Z}.

by weighting each generated event by a factor:

$$W(\{p^\nu\}, f_i^{\mathrm{V}}) \equiv \frac{\frac{1}{4}\sum_\lambda \left|(\mathcal{M}_{\mathrm{SM}}(\{p^\nu\},\lambda) + \mathcal{M}_{\mathrm{AC}}(\{p^\nu\},\lambda,f_i^{\mathrm{V}}))\right|^2}{\frac{1}{4}\sum_\lambda \left|\mathcal{M}_{\mathrm{SM}}(\{p^\nu\},\lambda)\right|^2}, \tag{7.1}$$

The weight factor W depends on the helicities of the initial electron/positron, the helicities of the final state four fermions and the phase space. After reweighting, the distributions according to given values of the anomalous couplings f_4^{V}, f_5^{V} ($\mathrm{V} = \mathrm{Z}, \gamma$) are obtained. Detector effects are properly taken into account for events reweighted at generator level.

7.1.2 Results on Anomalous Couplings

To determine the values of the anomalous couplings from the equal mass spectrum, the following binned likelihood function [2] is maximised:

$$\log \mathcal{L}(f_i^{\mathrm{V}}) = \sum_{j=1}^{\mathrm{N_{bin}}} \left[N_{obs}(j) \log N_{exp}(j, f_i^{\mathrm{V}}) - N_{exp}(j, f_i^{\mathrm{V}})\right]. \tag{7.2}$$

Here $\mathrm{N_{bin}}$ is the total number of bins and $N_{obs}(j)$ is the number of data events in j-th bin. The expected number of events in j-th bin is computed for each f_i^{V} fixing the other three to their SM values, and is given as $N_{exp}(j, f_i^{\rm V}) = N_{sig}(j, f_i^{\rm V}) + N_{bck}(j)$. Possible correlations among different couplings are considered by two-dimensional fitting.

No significant deviation from the Standard Model prediction is observed, which is translated into a 95% C.L. limit on the anomalous couplings. Table 7.1 summarises all the obtained limits compared with the respective SM predictions. Figure 7.2 shows the

$-0.37 \leq f_4^{\rm Z} \leq 0.43$	(SM: $f_4^{\rm Z}$=0)
$-0.82 \leq f_5^{\rm Z} \leq 0.94$	(SM: $f_5^{\rm Z}$=0)
$-0.25 \leq f_4^{\gamma} \leq 0.22$	(SM: f_4^{γ}=0)
$-0.49 \leq f_5^{\gamma} \leq 0.55$	(SM: f_5^{γ}=0)

Table 7.1: The 95% confidence level limits on the anomalous gauge couplings.

result of the two-dimensional fitting used to extract possible correlation among various couplings. We do not find any significant correlation and the results are found to be in consistent with the SM predictions.

7.2 Low Scale Gravity

Effect of low scale gravity is studied, basically, in a log-likelihood fit where the $\mathrm{e^+e^-} \to \mathrm{ZZ}$ cross sections measured at different centre-of-mass energies are compared to the Standard Model prediction plus a LSG contribution. In the following sections, we describe the experimental procedure used, in detail, before moving over to the result.

7.2.1 Experimental Procedure

The LSG contribution to Z-pair at Born level [3] is already described in Chapter 2. To take into account higher order corrections to the process involving ISR radiation, finite width effect *etc.*, following procedure is applied. First the SM cross section for the process, $\mathrm{e^+e^-} \to \mathrm{ZZ}$, is calculated from the Born level amplitudes. A correction factor, $\mathcal{A}$, is calculated as the ratio of the cross section in which all the higher-order corrections are properly taken care of (calculated using EXCALIBUR program) to the Born-level cross section. Figure 7.3 shows the values of $\mathcal{A}$ as estimated at different $\sqrt{s}$. Then the Z-pair cross section is calculated in the presence of LSG and it is multiplied by $\mathcal{A}$. From the comparison of this value with the measured cross section at different energies, a likelihood function is built as follows [4] :

$$\log \mathcal{L}(\Lambda) \;=\; \sum_i \left[\sigma_i^{obs} \cdot \log(\sigma_i^{obs}/\sigma_i^{exp}(\Lambda)) - (\sigma_i^{obs} - \sigma_i^{exp}(\Lambda))\right] \tag{7.3}$$

with $\sigma^{exp}(\Lambda) = \sigma^{\rm SM} + \sigma^{\rm LSG}(\Lambda)$, and $\Lambda = \frac{\lambda}{M_S^4}$. Here i denotes the energy point, σ^{obs} is the measured ZZ cross section and $\sigma^{\rm SM,LSG}$ are the expected cross sections with the Standard

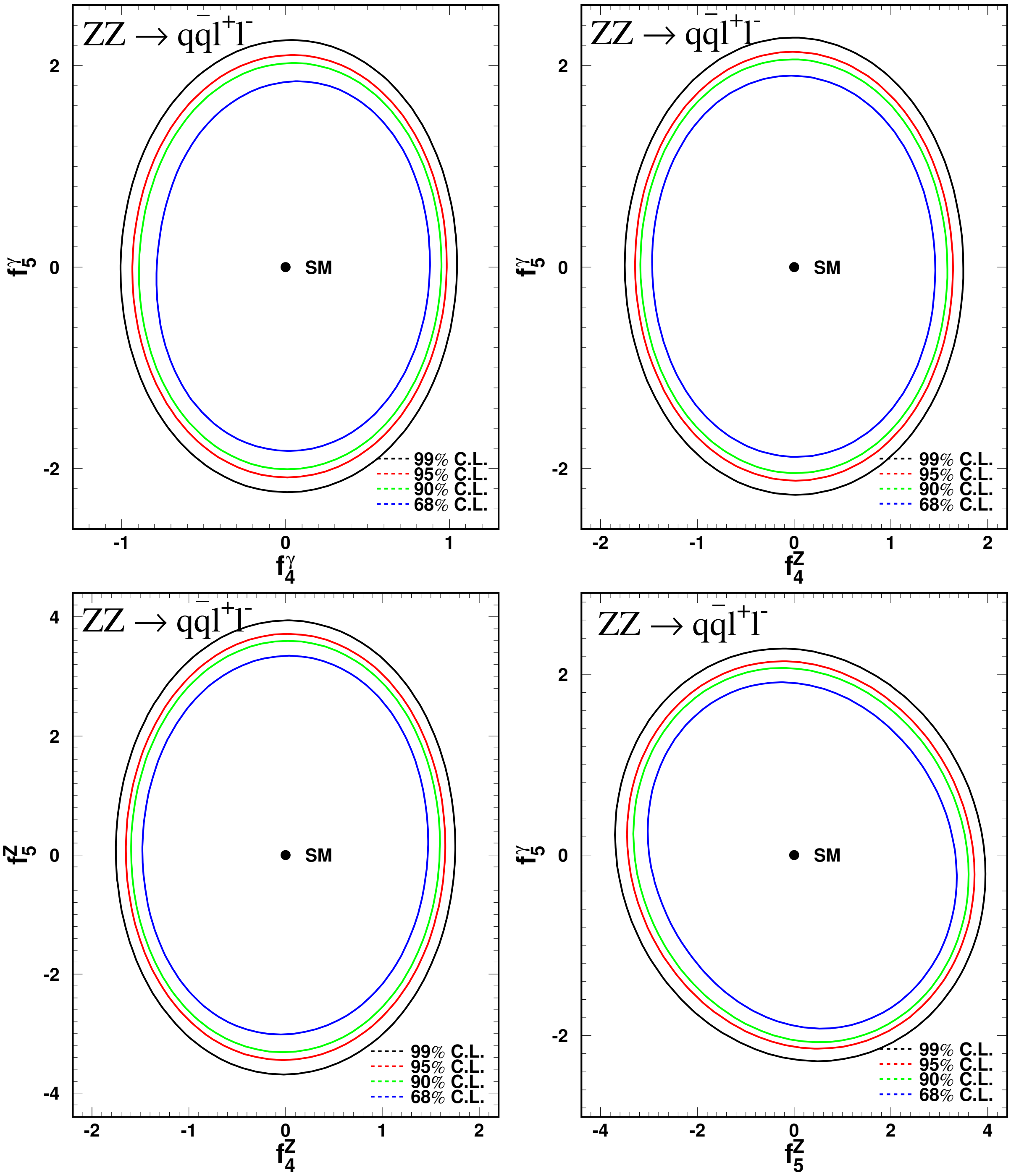

Figure 7.2: Two-dimensional contour plots showing possible correlations among various anomalous couplings. The SM prediction is indicated by the black dot.

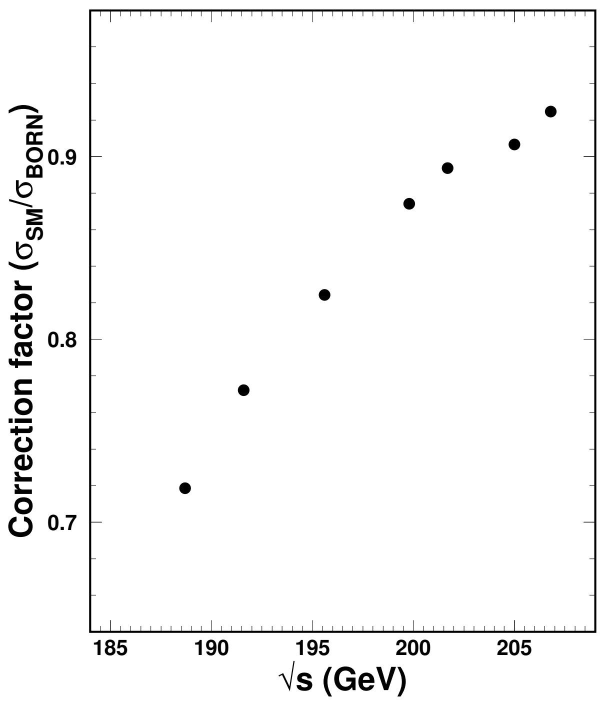

Figure 7.3: Correction factor to the Born level cross section as calculated at different $\sqrt{s}$.

Model and Low Scale Gravity after correction. Calculation of the 95% confidence level (C.L.) limits on Λ_+ and Λ_-, in case of null result, follows from the integration of the probability density function which is constructed out of the likelihood function [5] :

$$\int_0^{\Lambda_+^{95}} \mathcal{L}(\Lambda)\, d\Lambda = 0.95 \int_0^{+\infty} \mathcal{L}(\Lambda)\, d\Lambda, \tag{7.4}$$

and

$$\int_{-\Lambda_-^{95}}^{0} \mathcal{L}(\Lambda)\, d\Lambda = 0.95 \int_{-\infty}^{0} \mathcal{L}(\Lambda)\, d\Lambda. \tag{7.5}$$

In our analysis, we have used the full ZZ cross section instead of the cross section for the process, $ZZ \rightarrow q\bar{q}\ell^+\ell^-$, to have better statistical sensitivity.

7.2.2 Results on LSG

Figure 7.4(a) shows the deviation expected on the equal mass spectrum with additional LSG contribution corresponding to a string scale of $M_S = 475\,\text{GeV}$. No significant deviation is found compared to the Standard Model expectation leading to 95% C.L. lower limit on M_S, result of which is described in Figure 7.4(b). For λ equal to ± 1, the respective limits on M_S are found to be 670 and 730 GeV. The obtained lower limit can be further converted into a distance R at which any significant deviation from Newtonian gravity

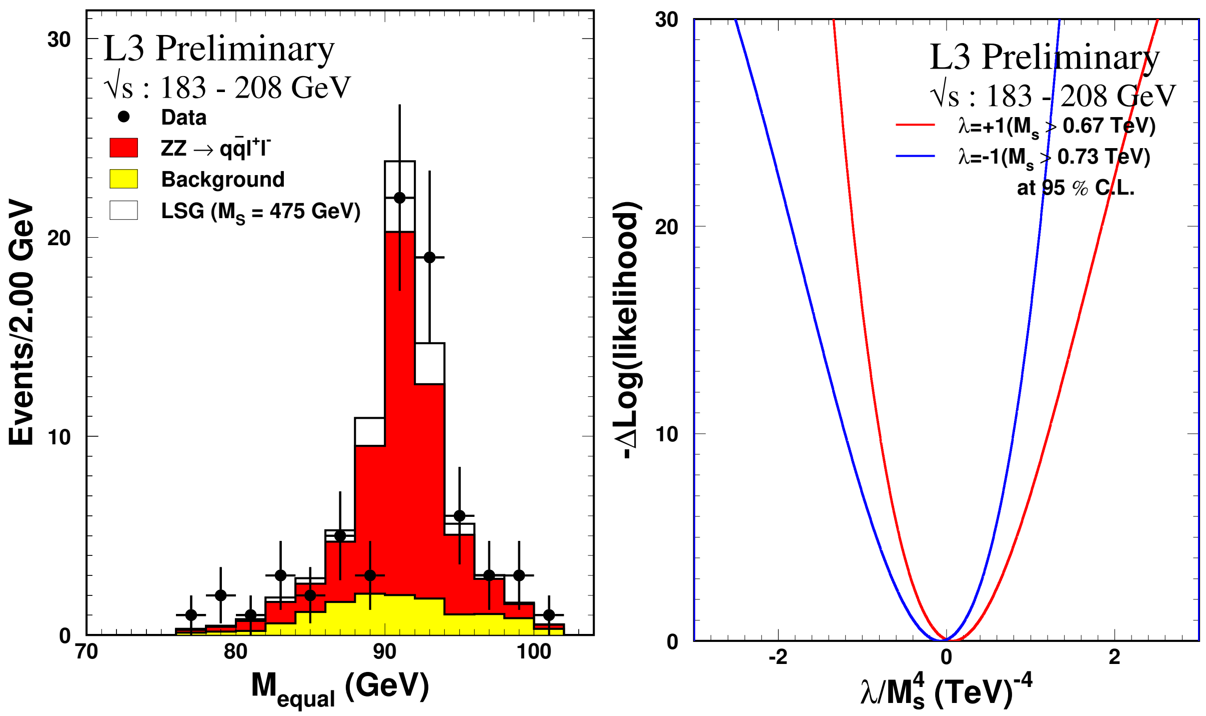

Figure 7.4: Modified distribution of equal mass spectrum in presence of Low Scale Gravity and log-likelihood curve for (λ/M_S^4) as obtained for the process, $e^+e^- \rightarrow ZZ$.

could be realised, using Equation 2.21. Table 7.2 summarise the values of R as obtained with different number of extra dimensions.

	$\lambda = +1,\ M_S = 670$ GeV	$\lambda = -1,\ M_S = 730$ GeV
$n = 1$	3.32×10^{13} cm	2.57×10^{13} cm
$n = 2$	2.23×10^{-2} cm	1.88×10^{-2} cm
$n = 3$	1.95×10^{-7} cm	1.69×10^{-7} cm
$n = 4$	5.77×10^{-10} cm	5.07×10^{-10} cm

Table 7.2: Conversion of the limits on Low Scale Gravity into distances up to which no deviations from Newtonian gravity to be expected.

A single extra dimension would have size of R larger than our solar system, as already mentioned in Chapter 2, and can be thus excluded. Possibility of two extra dimensions that leads to LSG at millimetre scale, can be also excluded from a recent experiment [6], which reported no deviations from the standard behaviour of gravitational force down to 10^{-3} cm. The number of extra dimensions in which the graviton propagates must be at least 3, for which our result indicates change in gravitational behaviour at a distance of the order of 1 nm (10^{-7} cm).

References

[1] G.J. Gounaris *et al.*, Phys. Rev. **D61** (2000) 073013;
J. Alcaraz *et al.*, Phys. Rev. **D61** (2000) 075006;
G. Mohanty, "W^+W^- and ZZ productions and couplings at LEP", Talk given at PHENO 2001 Symposium, University of Wisconsin, Madison, USA, May 2001.

[2] W.T. Eadie *et al.*, *Statistical Methods in Experimental Physics*, North-Holland (1971);
L. Lyons, *Statistics for nuclear and particle physicists*, Cambridge Univ. Press (1986).

[3] K. Agashe and N.G. Deshpande, Phys. Lett. **B456** (1999) 60.

[4] Similar likelihood function can be found in the following paper:
S. Baker and R.D. Cousins, Nucl. Inst. Meth. **A221** (1984) 437.

[5] L3 Collab., M. Acciarri *et al.*, Phys. Lett. **B464** (1999) 135;
S. Mele and E. Sánchez, Phys. Rev. **D61** (2000) 117901;
E. Sánchez, in *private communication.*

[6] C.D. Hoyle *et al.*, Phys. Rev. Lett. **86** (2001) 1418.

Chapter 8

Neutral Current Four-Fermion Production

Study of four-fermion production via neutral currents [1] at LEP is one of the basic tests of higher order processes in the Standard Model of electroweak interactions. It has also important discovery potential for particles produced in association with Z [2]. A dedicated study of neutral current four-fermion production thus represents a complementary search for new physics, that could manifest itself in sizable deviations of rates or kinematic distributions from the SM expectations.

In the present chapter, the analysis of the $q\bar{q}\ell^+\ell^-$ ($\ell = e, \mu$) final states originating from the neutral-current processes is described. Particular emphasis has been laid on the study of di-lepton invariant and recoil mass spectra to search for new physics, in a model independent way.

8.1 Data and Monte Carlo Samples

The same set of data and Monte Carlo samples used for the study of Z-boson pair production is also used in this analysis. The data-set corresponds to a total integrated luminosity of 682 pb^{-1}, whose exact break-up at different energy is given in Table 4.1.

Processes leading to the $q\bar{q}\ell^+\ell^-$ four-fermion final state are generated using EXCALIBUR [3] Monte Carlo program. Suitable cuts are applied at generator level on the polar angle of the leptons and the invariant mass of the $f\bar{f}$ pair. First criterion takes care of limited lepton detection coverage in extreme forward regions. It also reduces the relative contribution from the multiperipheral diagram, in case of electron in the final state. Lower cut-off on the invariant mass is required to counter the diverging four-fermion cross section in the limit of $m_{f\bar{f}} \to 0$, since EXCALIBUR treats all the fermions to be massless. All these phase-space requirements are listed in Table 8.1. Figure 8.1 justifies the utility of signal definition cuts for $q\bar{q}\mu^+\mu^-$ final state, by showing

$\lvert\cos\theta_\ell\rvert$		$<$	0.95
$M_{\ell^+\ell^-}$	(GeV)	$>$	5.00
$M_{q\bar{q}}$	(GeV)	$>$	10.00

Table 8.1: Four-fermion signal definition cuts applied at generator level.

the fall in the muon detection acceptance for L3 detector in extreme forward region and almost exponential dependence of the four-fermion cross section in the limit of $m_{f\bar{f}} \rightarrow 0$.

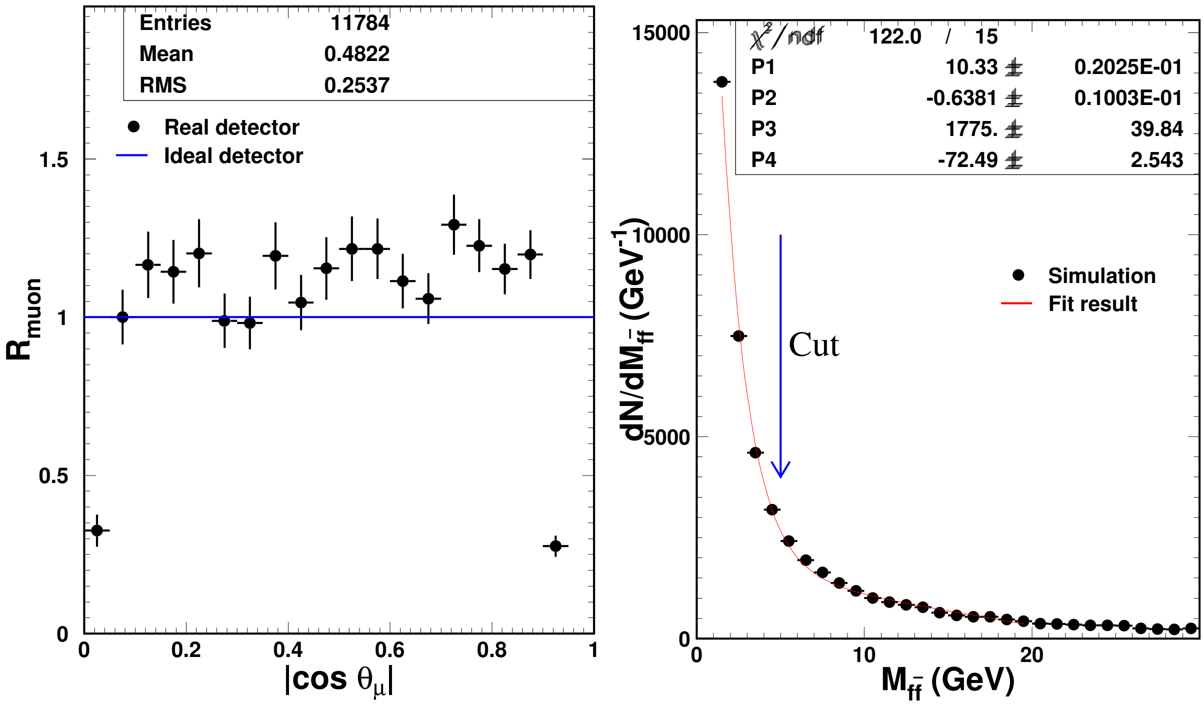

Figure 8.1: Utility of four-fermion signal definition cuts: (a) muon detection acceptance as a function of its polar angle, and (b) the generated di-muon mass in the low-mass region. The latter is fitted to an exponential plus polynomial function of order 1.

8.2 Event Selection

8.2.1 Loose Preselection

At preselection level, we require at least 4 charged tracks and 10 calorimetric clusters in addition to two leptons. It should be noted here that, the lepton identification criteria is same as in the case of Z-pair production, however, with the cuts on the lepton energy relaxed little bit. The visible energy, E_{vis}, must be greater than 0.45 $\sqrt{s}$ and the energy imbalance both along the longitudinal and transverse directions must not exceed 0.35 E_{vis}. These two cuts help in getting rid of low multiplicity events as well as events with large missing energy. Contribution from the two-photon mediated process where both the electron and positron escape through the beam-pipe, is rejected by requiring the event thrust axis not to point along the beam direction. Figure 8.2(a) shows the variation of the overall signal efficiency at preselection level both for $q\bar{q}e^+e^-$ and $q\bar{q}\mu^+\mu^-$ final states with centre-of-mass energies. The average efficiencies are found to be 71% and 55% for the $q\bar{q}e^+e^-$ and $q\bar{q}\mu^+\mu^-$ final states respectively.

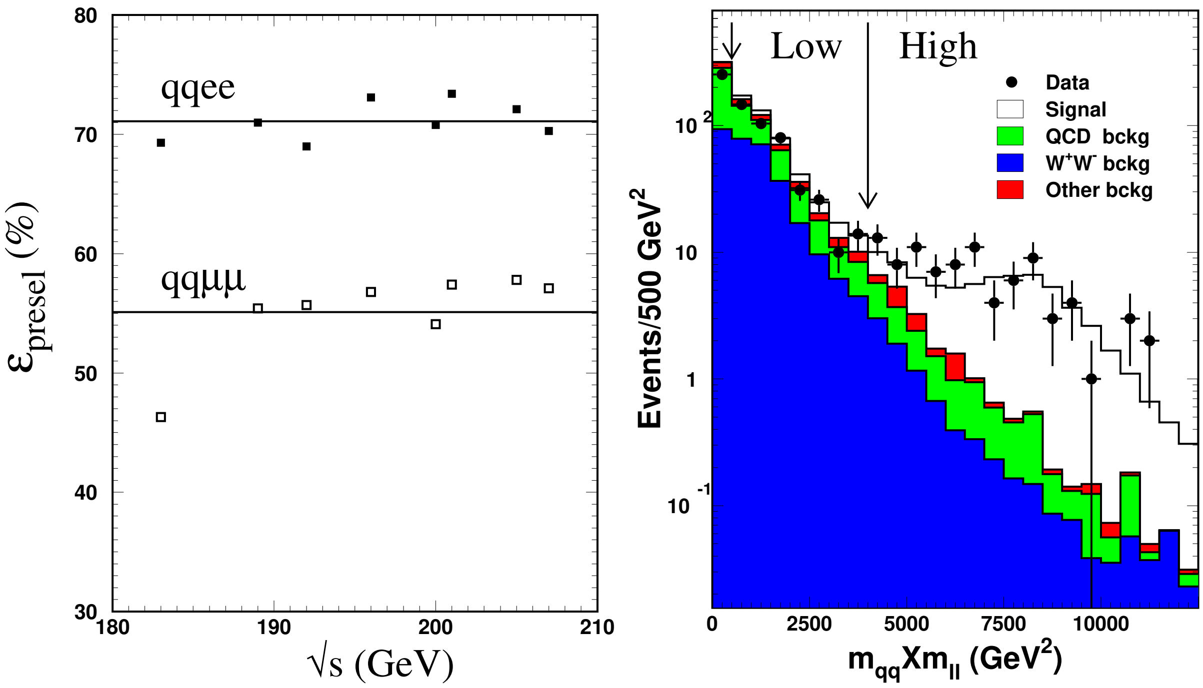

Figure 8.2: (a) Preselection efficiency of the $\mathrm{q\bar{q}e^+e^-}$ and $\mathrm{q\bar{q}}\mu^+\mu^-$ final states at different $\sqrt{s}$, and (b) the product of $m_{\mathrm{q\bar{q}}}$ and $m_{\ell^+\ell^-}$, used for separating the low and high mass regions. The first bin in the second plot is rejected, as it is mostly due to backgrounds.

8.2.2 Final Selection

Two separate sets of selection cuts are chosen for selecting the $\mathrm{q\bar{q}}\ell^+\ell^-$ events in the low as well as high mass region, since the underlying physics and the background processes involved are quite different for these two regions. The low mass region is mostly dominated by the $\gamma^\star$-mediated process, while in the region close to m_{Z}, the Z-mediated process takes over. As it is shown in Figure 8.2(b), the low and high mass regions are separated by putting the following cut on the product of $m_{\mathrm{q\bar{q}}}$ and $m_{\ell^+\ell^-}$:

- Low mass : $500 < m_{\mathrm{q\bar{q}}} \cdot m_{\ell^+\ell^-} < 4000$ GeV^2
- High mass : $m_{\mathrm{q\bar{q}}} \cdot m_{\ell^+\ell^-} > 4000$ GeV^2

This way of separating the two regions nicely takes care of the intermediate mass region. For each region, we optimise on the selection variables and the two selections are combined by a logical $\mathcal{OR}$. Table 8.2 shows the cut position on various selection variables used for selecting $\mathrm{q\bar{q}}\ell^+\ell^-$ events at $\sqrt{s} = 189$ GeV. These cut values are retuned at each centre-of-mass energy to take care of modified event topology. Figure 8.3 shows the distribution for two of the important selection variables, normalised transverse energy imbalance and energy of the most energetic lepton scaled to $\sqrt{s}$. We find a nice agreement between the data and the Standard Model expectation.

Final state	Mass region	Selection variables		Cut value
$q\bar{q}e^+e^-$	Low	$E_\perp/E_{vis}$	$<$	0.14
		E_{e2}/E_{e1}	$>$	0.15
		$E_{e1}/\sqrt{s}$	$>$	0.13
	High	$E_\perp/E_{vis}$	$<$	0.14
		$E_{e2}/\sqrt{s}$	$>$	0.07
$q\bar{q}\mu^+\mu^-$	Low	$E_\perp/E_{vis}$	$<$	0.24
		$E_{\mu 1}/\sqrt{s}$	$>$	0.09
		$M^{rec}_{\mu^+\mu^-}$ (GeV)	$>$	5.00
	High	$E_{\mu 1}/\sqrt{s}$	$>$	0.12
		$E_{vis}/\sqrt{s}$	$>$	0.68

Table 8.2: Typical cut position used for selecting the $q\bar{q}\ell^+\ell^-$ events at $\sqrt{s} = 189$ GeV.

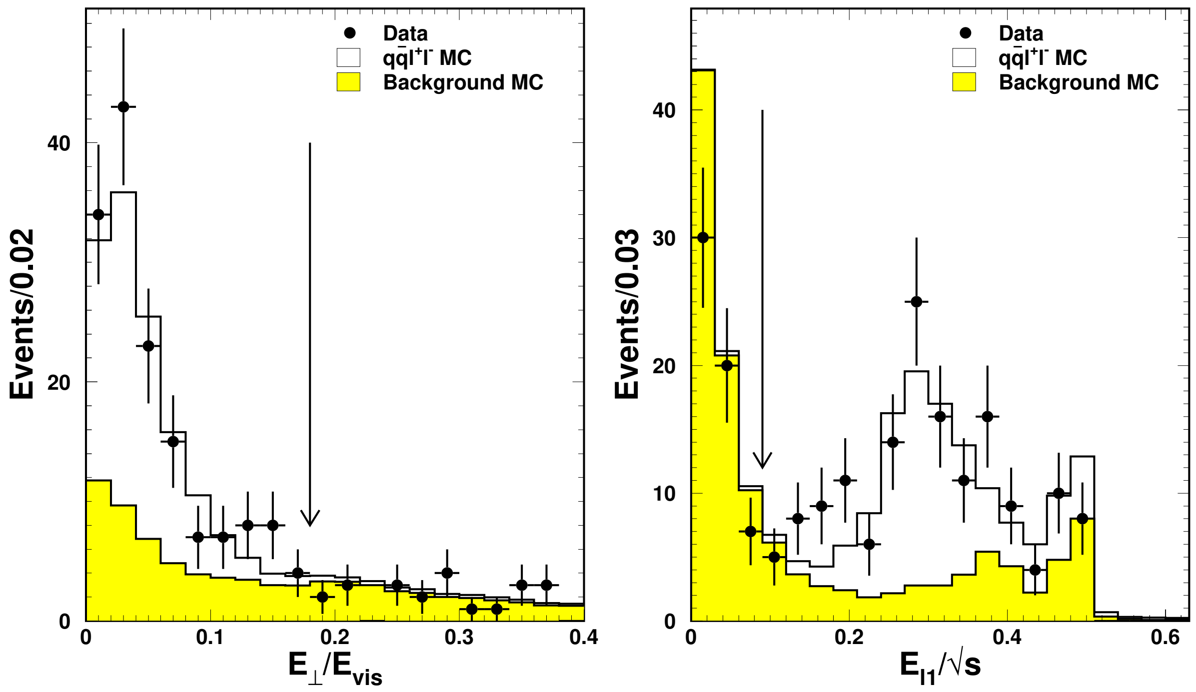

Figure 8.3: Distributions of (a) the transverse energy imbalance, and (b) the energy of most energetic lepton scaled to $\sqrt{s}$. The arrow mark indicates typical cut position. The contributions both from the $q\bar{q}e^+e^-$ and $q\bar{q}\mu^+\mu^-$ final states are added together to have better statistics.

8.2.3 Selection Performance

The selection performance is summarised in Table 8.3 for the individual sub-channels, $q\bar{q}e^+e^-$ and $q\bar{q}\mu^+\mu^-$. In total, we select 134 candidates in data, compared with 126 events expected from the Standard Model processes (signal=90 and background=36). Figure 8.4 show the distributions of the di-lepton invariant and recoil mass (di-jet mass) spectra for $q\bar{q}\ell^+\ell^-$ final state. One finds good agreement between the data and the SM predictions. Also the angular distributions of the di-jet and di-lepton systems show similar trend, as shown in Figure 8.5.

Final State	Efficiency(%)	Purity(%)	N_{signal}	$N_{background}$	N_{data}
$q\bar{q}e^+e^-$	59.5	68.3	59.1±0.45	27.4±0.67	97.0
$q\bar{q}\mu^+\mu^-$	54.5	78.4	30.6±0.17	8.4±0.25	37.0
		Total	89.7±0.48	35.8±0.71	134.0

Table 8.3: Selection performance of four-fermion events in terms of overall selection efficiency, purity, expected signal, background and observed data events. The uncertainties on signal and background expectation, due to finite Monte Carlo statistics, are also given.

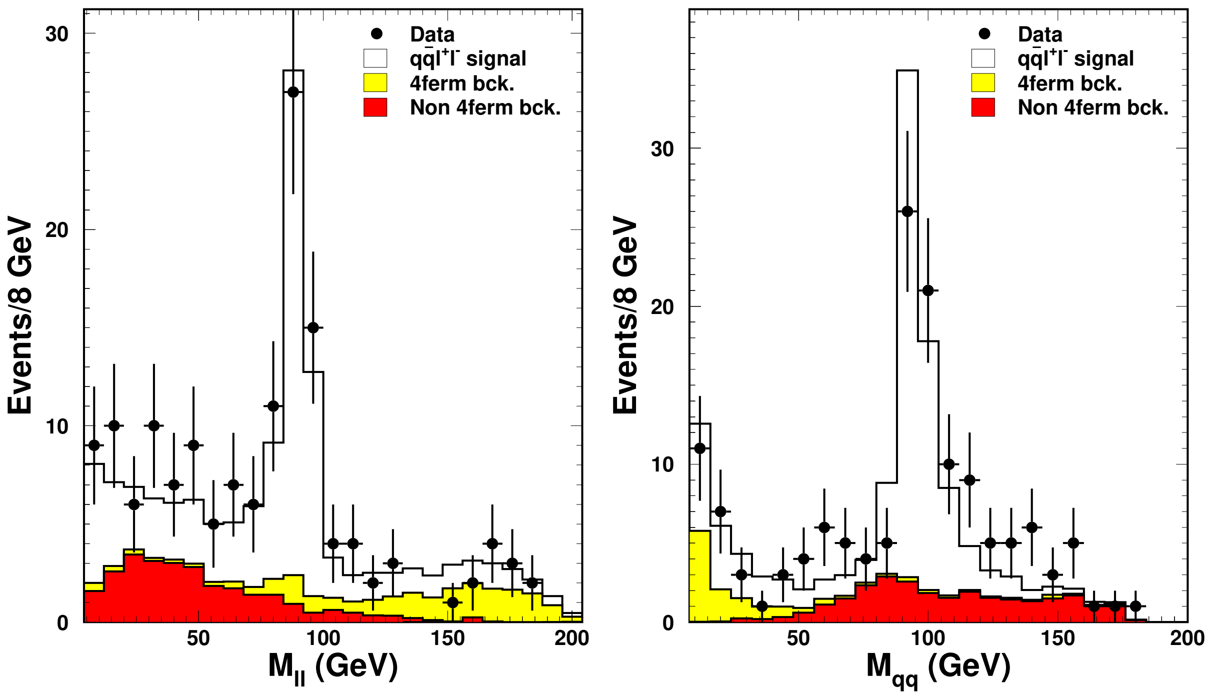

Figure 8.4: Distributions of (a) the lepton-pair invariant mass, and (b) the hadronic mass recoiling against of them, for $q\bar{q}\ell^+\ell^-$ final state. Here "4ferm bck." indicates the event that does not pass through the signal definition cut, as given in Table 8.1.

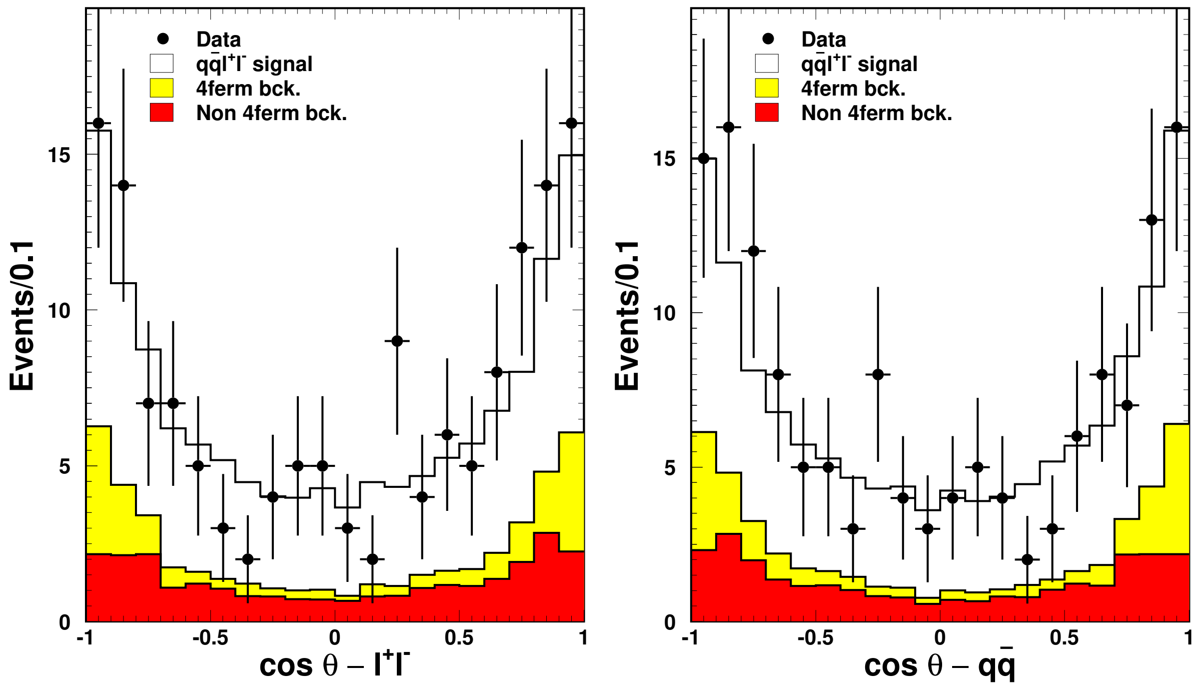

Figure 8.5: Distributions of the production angle of (a) the di-lepton system, and (b) the recoiling di-jet system. Strong forward/backward peak is due to pole in the e–propagator.

8.3 Results

8.3.1 The Four-Fermion Cross Section

Systematic Source	Error (%)
Energy Scale	0.713
Cut Variation	2.202
Lepton Identification	1.900
Bckg. Normalisation	0.656
Signal MC statistics	0.416
Bckg. MC statistics	1.884
Total	3.622

Table 8.4: Systematic uncertainties on the four-fermion cross section.

Cross section for the $q\bar{q}\ell^+\ell^-$ four fermion final state is calculated by fitting the di-lepton invariant mass spectrum to a maximum binned log-likelihood function. Figure 8.6 shows the ratio of the measured four-fermion cross section to the Standard Model values at different centre-of-mass energies. We find reasonable agreement between our measurement [4, 5] and the SM expectation. However, keeping the large statistical error in mind, we have opted for a single luminosity-averaged cross section, each for the $q\bar{q}e^+e^-$ and $q\bar{q}\mu^+\mu^-$ final states separately. The reason for treating them in this way stems from the fact that they originate from different sources as explained in Chapter 2. Various systematic uncertainties are studied as enlisted in Table 8.4. The measured $q\bar{q}e^+e^-$ and $q\bar{q}\mu^+\mu^-$ four-fermion cross sections are $0.184^{+0.026}_{-0.024} \pm 0.005$ and $0.077^{+0.018}_{-0.015} \pm 0.003\,\mathrm{pb}$ respectively, in good agreement with the corresponding SM values of 0.150 and 0.086 pb.

The quoted errors are respectively statistical and systematic errors.

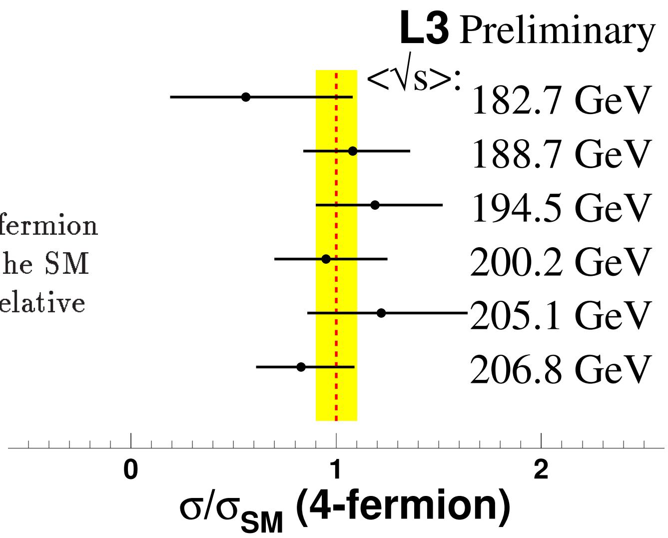

Figure 8.6: Ratio of the measured four-fermion cross section for $q\bar{q}\ell^+\ell^-$ final states to the SM prediction. The yellow band implies a relative error of 10% on the prediction.

8.3.2 Sensitivity to New Physics

In a bid to look for new physics in an unbiased manner, we have studied the scatter plot of the invariant and recoil mass spectra in the selected $q\bar{q}\ell^+\ell^-$ data sample as shown in Figure 8.7(a). No significant structure, beyond the Standard Model expectation, is observed in the mass spectra. Further study has been performed on the mass of the $f\bar{f}$ system recoiling against Z, M_X. Here also nothing unusual is noticed on the mass spectra (Figure 8.7(b)).

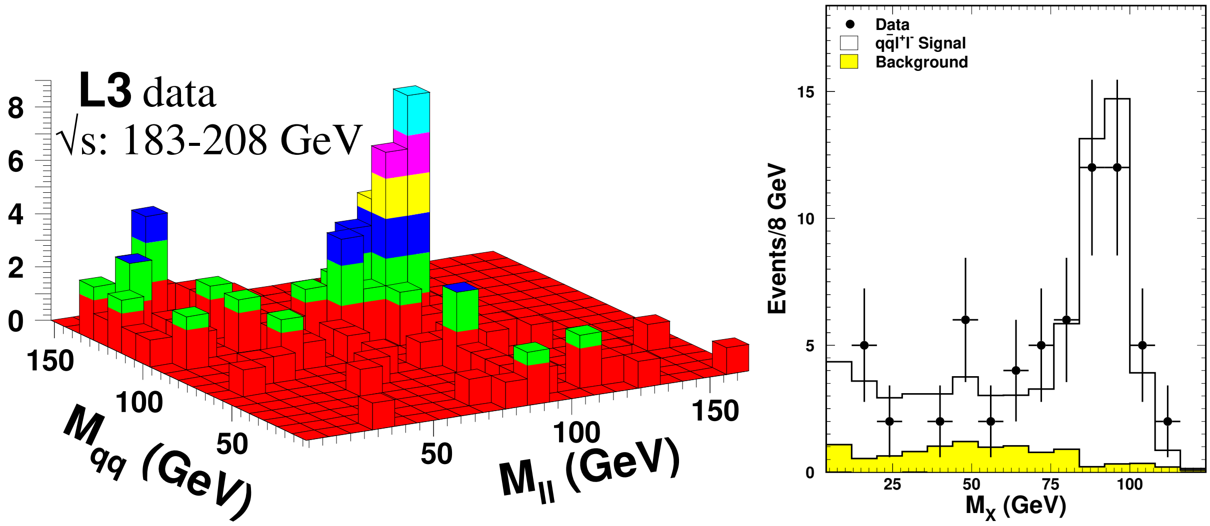

Figure 8.7: (a) Scatter plot of the invariant *vs.* recoil mass of the lepton-pair in the selected $q\bar{q}\ell^+\ell^-$ data sample (different colour shade indicates the number of event in the box), and (b) the mass of the system recoiling against Z.

References

[1] G. Altareli *et al.*, "Physics at LEP2", CERN 96-01, Volume 1.

[2] F. Diakonos *et al.*, Phys. Lett. **B260** (1991) 219;
P. García–Abia and W. Lohmann, Eur. Phys. J. direct **C2** (2000) 1.

[3] EXCALIBUR Monte Carlo Program:
F.A. Berends *et al.*, Comp. Phys. Comm. **85** (1995) 437.

[4] G. Mohanty, *Preliminary status of Four-Fermion analysis on semileptonic sector*, Talk given at L3 Analysis Workshop, BalatonFüred, Hungary, June 2001;
G. Mohanty, *Status report on Four-Fermion final states*, Talk given at L3 Extended Analysis Meeting, CERN, Switzerland, September 2001;
G. Mohanty, $Z\gamma^\star$ *selections and status of the paper*, Talk given at L3 Analysis Week, Aachen, Germany, May 2002.

[5] T. Aziz and G. Mohanty, L3 Internal Note # 2739 (2002).

Chapter 9

Summary and Outlook

Study of Z-boson pair production has been performed over a wide energy range: from 183 (just above the production threshold) to 208 GeV the maximum energy attained at LEP, with particular emphasis on the $q\bar{q}\ell^+\ell^-$ final state [1]. Measured cross section values for the process, $e^+e^- \to ZZ \to q\bar{q}\ell^+\ell^-$, as well as for the full process, $e^+e^- \to ZZ$, are found to be in good agreement with the Standard Model expectations. The result on measured

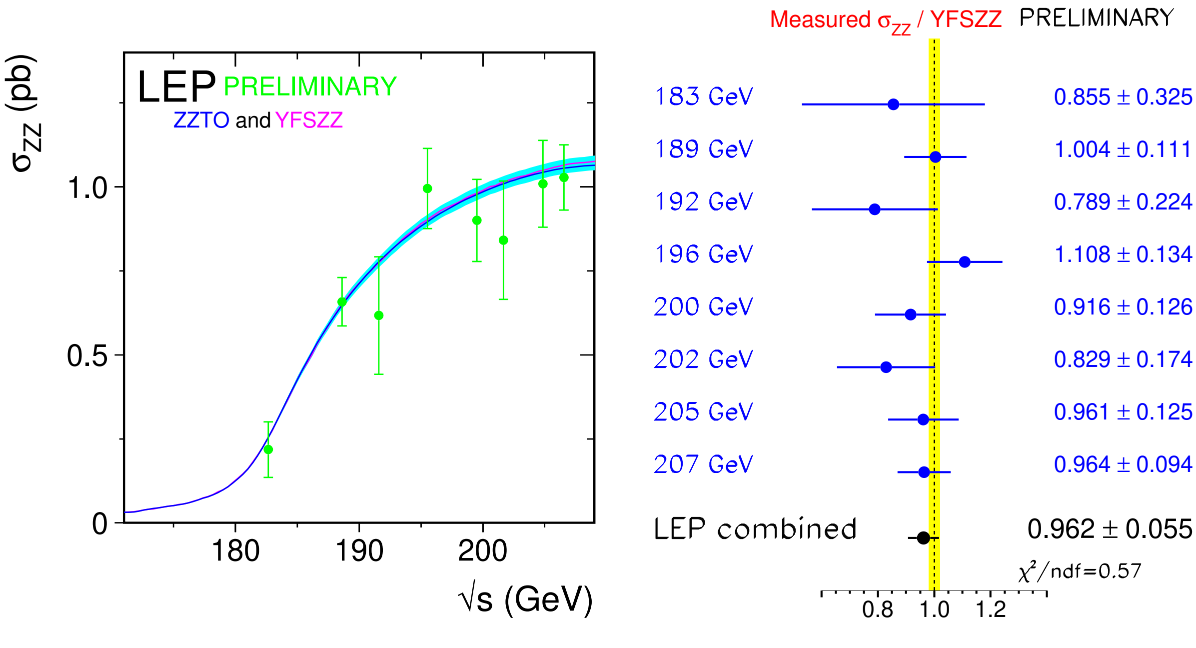

(a) Evolution of measured σ_{ZZ} with $\sqrt{s}$.

(b) Ratio of measured σ_{ZZ} to the SM value.

Figure 9.1: Combined LEP results on Z-pair production.

cross section [2] has been combined with that of other LEP experiments [3], result of which is shown in Figure 9.1. A good agreement with the SM prediction is observed.

A dedicated study of inclusive $b\bar{b}X$ final state has been carried out in connection with the Standard Model Higgs production at LEP. Measurement of cross section for the processes, $e^+e^- \to ZZ \to b\bar{b}\ell^+\ell^-$ and $e^+e^- \to ZZ \to b\bar{b}X$, gave results [2] consistent with ZZ production, and due to low statistics no statement about Higgs could be made.

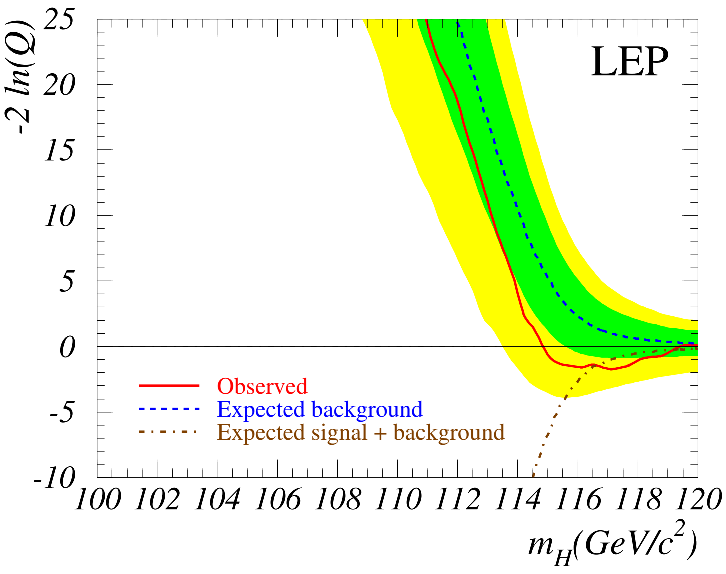

Figure 9.2: Result on SM Higgs search at LEP.

At this point, we would like to say few sentences on the results from direct Higgs search at LEP [4, 5]. Values for Higgs mass up to 114.1 GeV are excluded at 95% confidence level. This is bit lower than the expected mass limit at 115.4 GeV, because of a few good (Higgs–like) candidates observed in this mass window. Probability that this excess was due to a fluctuation of the SM background is 3.4%. The effect is mainly driven by the ALEPH data in the four-jet final state [4]. Figure 9.2 shows the test-statistics $-2\ \ln(Q)$ as the function of the Higgs mass. Observed excess is represented by slight dip in the vicinity of $m_{\mathrm{H}} = 116\,\mathrm{GeV}$, touching the expectation of signal plus background hypothesis.

Search for physics beyond Standard Model has been carried out in the sector of anomalous trilinear gauge couplings (forbidden in the SM) and Low Scale Gravity. No significant deviations from the SM predictions were found resulting in 95% confidence limits on the anomalous coupling, and on the string scale (M_S) that represented the effect of LSG. Table 9.1 summarises the LEP-wide results on the trilinear gauge couplings and M_S. Results are consistent with the Standard Model predictions. No deviation from the standard behaviour of gravitational force is expected down to the distance of 1 nm.

Anomalous Gauge Couplings			
f_4^Z	$\in$	$[-0.30, 0.28]$	
f_5^Z	$\in$	$[-0.36, 0.38]$	
f_4^γ	$\in$	$[-0.17, 0.19]$	
f_5^γ	$\in$	$[-0.34, 0.38]$	
Low Scale Gravity			
		$\lambda = +1$	$\lambda = -1$
M_S (TeV)	$>$	1.20	1.09

Table 9.1: LEP-wide limits on the anomalous gauge couplings and LSG.

Study on neutral current four-fermion production has been extended over to the full accessible mass range in the $q\bar{q}\ell^+\ell^-$ final state. The measurements of $q\bar{q}\ell^+\ell^-$ four fermion cross sections were found to be in agreement with the Standard Model expectations [7]. No anomalous structures were observed in the di-lepton invariant and recoil mass (di-jet invariant mass) spectra.

To summarise, all our measurements and searches are in agreement with the Standard Model. Higgs sector still remains as one of the least understood sectors of SM with Higgs particles escaping the experimenter eye. Now, the mantle has been handed over to Tevatron and future Large Hadron Collider (LHC) to look for Higgs, and unravel the next layer of physics which would explain many of the unanswered questions in the Standard Model.

References

[1] T. Aziz and G. Mohanty, L3 Internal Note # 2726 (2002).

[2] L3 Collab., M. Acciarri *et al.*, Phys. Lett. **B450** (1999) 281;
L3 Collab., M. Acciarri *et al.*, Phys. Lett. **B465** (1999) 363;
L3 Collab., M. Acciarri *et al.*, Phys. Lett. **B497** (2001) 23;
G. Mohanty, L3 Internal Note # 2542l (2000);
Contributed to the 2002 summer conferences, L3 Internal Note # 2770 (2002).

[3] ALEPH Collab., R. Barate *et al.*, Phys. Lett. **B469** (1999) 287;
ALEPH Collab., ALEPH 2001-006 CONF 2001-003;
DELPHI Collab., P. Abreu *et al.*, Phys. Lett. **B497** (2001) 199;
DELPHI Collab., DELPHI 2001-015 CONF 456;
OPAL Collab., G. Abbiendi *et al.*, Phys. Lett. **B476** (2000) 256;
OPAL Collab., OPAL Physics Note PN482.

[4] ALEPH Collab., A. Heister *et al.*, Phys. Lett. **B526** (2002) 191.

[5] L3 Collab., P. Achard *et al.*, Phys. Lett. **B517** (2001) 319;
DELPHI Collab., DELPHI 2002-041-CONF-575;
OPAL Collab., OPAL Physics Report PR367, July 2002;
LEP Higgs Working Group Note # 2002-01, July 2002.

[6] Stephan Wynhoff, *Anomalous Triple Neutral & Quartic Gauge Boson Couplings*, Talk given at ICHEP02, Amsterdam, Holland, July 2002;
G. Bernardi, *Low Scale Gravity & Extra Dimensions at HERA, LEP and Tevatron*, Talk given at ICHEP02, Amsterdam, Holland, July 2002.

[7] T. Aziz and G. Mohanty, L3 Internal Note # 2739 (2002).

Publications of Gagan Bihari Mohanty

[1] ZZ Production in e^+e^- interaction at $\sqrt{s} = 189$ GeV.
E. Sanchez-Alvaro *et al.*, L3 Note # 2413.
Submitted to International Europhysics Conference on High Energy Physics, Tampere, July 1999.

[2] Study of Z Boson Pair Production at LEP.
S. Mele *et al.*, L3 Note # 2579.
Submitted to XXX International Conference on High Energy Physics, Osaka, July - August 2000.

[3] Model Independent Search for Physics Beyond Standard Model.
T. Aziz, G. Mohanty, L3 Note # 2606, August 2000.

[4] Study of Z Boson pair production at LEP
S. Mele *et al.*, L3 Note # 2696.
Submitted to International Europhysics Conference on High Energy Physics, Budapest, July 2001.

[5] Study of $e^+e^- \to$ ZZ events with the L3 detector at LEP.
T. Aziz and G. Mohanty, L3 Note # 2726 (2002).

[6] Study of Neutral-Current Four-Fermion Processes at LEP.
T. Aziz and G. Mohanty, L3 Note # 2739 (2002).

Published journals:

Co-author of 75 publications from the L3 Collab., since April 1999. Some of the selected ones are given here:

1. Search for the Standard Model Higgs boson in e^+e^- interactions at $\sqrt{s} = 189$ GeV.
L3 Collab., M. Acciarri *et al.*, Phys. Lett. **B461** (1999) 376.

2. Search for Low Scale Gravity Effects in e^+e^- collisions at LEP.
L3 Collab., M. Acciarri *et al.*, Phys. Lett. **B464** (1999) 135.

3. Study of Z Boson Pair Production in e^+e^- collisions at LEP at $\sqrt{s} = 189$ GeV.
L3 Collab., M. Acciarri *et al.*, Phys. Lett. **B465** (1999) 363.

4. Search for Extra Dimensions in Boson and Fermion Pair Production in e^+e^- interactions at LEP.
L3 Collab., M. Acciarri *et al.*, Phys. Lett. **B470** (1999) 281.

5. Search for Anomalous $ZZ\gamma$ and $Z\gamma\gamma$ couplings in the process $e^+e^- \to Z\gamma$ at LEP.
L3 Collab., M. Acciarri *et al.*, Phys. Lett. **B489** (2000) 55.

6. Higgs Candidates in e^+e^- interactions at $\sqrt{s} = 206.6$ GeV.
L3 Collab., M. Acciarri *et al.*, Phys. Lett. **B495** (2000) 18.

7. Study of Z Boson Pair Production in e^+e^- interactions at $\sqrt{s} = 192$–202 GeV.
L3 Collab., M. Acciarri *et al.*, Phys. Lett. **B497** (2001) 23.

8. Search for the Standard Model Higgs boson in e^+e^- collisions at $\sqrt{s}$ up to 202 GeV.
L3 Collab., M. Acciarri *et al.*, Phys. Lett. **B508** (2001) 225.

9. Standard Model Higgs Boson with the L3 Experiment at LEP.
L3 Collab., P. Archad *et al.*, Phys. Lett.**B517** (2001) 319.